

Dynamic Modelling of Overhead Power Lines for Electric Trains



John Martin

University College

University of Oxford

A thesis submitted for the degree of

Doctor of Philosophy

Hilary 2019

Abstract

Electric and hybrid trains are popular across Europe and many overhead lines have been installed. The train collects electrical power from a high-voltage contact wire using a pantograph, which is a metal framework attached to the roof of the train. The contact wire is supported by a messenger wire through a series of vertical droppers, while registration arms maintain the horizontal stagger of the contact wire. The modelling of the pantograph-catenary interaction is an important part of overhead-system design and it is desirable to maximise the speed of simulation software while maintaining realism.

A Galerkin approach, also known as modal analysis, is used to solve the Euler-Bernoulli wire equations, as opposed to the typical finite-element methods. This approach was chosen to improve simulation speed and allow dynamically chosen velocity profiles to be modelled. Elimination of variables is then used to reduce the index-three differential-algebraic equation to an ordinary differential equation after eigenvector decomposition is used to diagonalise the system.

The model is validated against the 2002 and 2018 European Standards for pantograph-catenary simulation. Each of these standards provides an idealised model of an overhead system and requires that the simulation software produce results that are in agreement with the standard's benchmark. The model is then tested against real data from the Old Dalby test track.

The model is shown to produce realistic results at excellent simulation speeds. The final model includes up to two pantographs, contact-wire transitions and dropper unloading. The equations used to produce the model are explained in detail, many results are presented and numerous ideas to further improve the model are described.

Acknowledgements

Firstly, I wish to express my sincere thanks to my supervisor, Professor Stephen Duncan, for guiding me throughout my research. His expertise, insight and support were invaluable and it was a pleasure to work with him.

Secondly, I would like to extend my gratitude to Christopher Bryan, who was kind enough to lend his extensive knowledge of real-world pantograph-catenary systems. His insight into the nuances of overhead systems was greatly helpful and he was always eager to answer any questions I had.

Finally, I would like to thank the EPSRC for funding this research. This work would not have been possible without the generous stipend I received from them.

Contents

1	Introduction and Literature Review	1
1.1	Introduction	1
1.1.1	History	1
1.1.2	Background	2
1.1.3	The Pantograph	5
1.1.4	The Overhead Line	7
1.1.5	The Importance of Pantograph-Catenary Modelling	10
1.1.6	Outline of Thesis	11
1.2	Literature Review	12
1.2.1	The Pantograph	12
1.2.2	Finite-Element Methods (FEM)	13
1.2.3	The Galerkin Approach	14
1.2.4	Energy in the System	15
1.2.5	The Pantograph Position Constraint	16
1.2.6	Numerical Solution of DAEs	17
1.2.7	Contact-Wire Transitions	19
1.2.8	Wear Modelling	20
1.2.9	Aerodynamic Effects	21
1.3	Contributions	21
2	Modelling	23
2.1	Introduction	23

2.2	The Mathematical Model	23
2.2.1	The Pantograph	23
2.2.2	The Contact Wire	28
2.2.3	The Messenger Wire	31
2.2.4	The Droppers	33
2.2.5	The Registration Arms	35
2.2.6	The Algebraic Constraints	36
2.2.7	The Index-Three DAE	37
2.3	The Solution Process	39
2.3.1	Spatial Discretisation	39
2.3.2	Evaluation of Spatial Basis Functions	41
2.3.3	Orthogonality Integrals	44
2.3.4	Messenger Supports	48
2.3.5	Registration-Arm Constraints and Rotations	51
2.3.6	The Vertical Pantograph Constraints	52
2.3.7	Modal Index-Three DAE	53
2.3.8	The Structure of A_1	54
2.3.9	Eigenvector Decomposition	55
2.3.10	Modal Damping	56
2.3.11	Model Order Reduction	57
2.3.12	Possible Methods of DAE Solution	58
2.3.13	Reconstruction	62
2.3.14	Overview of Solution Process	62
2.3.15	Choice of Numbers of Modes	63
2.4	Conclusions	66
3	Validation Against BS:EN 50318:2002	67
3.1	Introduction	67
3.2	Specification	67
3.2.1	The Pantograph	68

3.2.2	The Catenary System	68
3.2.3	Quality of Validation	69
3.2.4	Numbers of Modes Used	69
3.2.5	Plots of Eigenmodes	70
3.3	Results	73
3.3.1	Snapshots	73
3.3.2	Dynamic Deflections at 250 km/hour	74
3.3.3	Dynamic Deflections at 300 km/hour	77
3.3.4	Contact-Force Plots	80
3.3.5	Comparison to Required Results	81
3.3.6	Verification Using MATLAB Code	82
3.3.7	Simulation Speed	83
3.4	Conclusions	84
4	Validation Against BS:EN 50318:2018	85
4.1	Introduction	85
4.2	Model Updates	87
4.2.1	Multiple Pantographs	87
4.2.2	Dropper Unloading	89
4.3	Results	91
4.3.1	Snapshots	91
4.3.2	Contact-Force Plots	100
4.3.3	Comparison to Required Results	101
4.3.4	Simulation Speed	103
4.4	Conclusions	103
5	Contact Events	105
5.1	Introduction	105
5.2	Detection of Events	106
5.2.1	A Pantograph Comes Into Contact	106

5.2.2	A Pantograph Comes Out of Contact	106
5.2.3	Simplified Events	106
5.3	Impact Modelling	107
5.4	Simulink Implementation	109
5.4.1	Contact Conditions	109
5.4.2	Avoidance of Algebraic Loops	111
5.4.3	New-Wire Events	112
5.5	Results	112
5.5.1	Snapshots	112
5.5.2	Contact-Force Plots	115
5.5.3	Comparison of Results	121
5.6	Simulation Speed	122
5.7	Conclusions	123
6	Validation Against Old Dalby Test-Track Data	125
6.1	Introduction	125
6.1.1	Old Dalby Data	125
6.1.2	Test-Track Layout	126
6.2	Model Updates	129
6.2.1	Differing Catenary Systems	129
6.2.2	Wire Gradients	129
6.2.3	Aerodynamic Pantograph Forces	130
6.2.4	Calculation of Original Dropper Lengths	131
6.2.5	Choice of Eliminated Eigenmodes	131
6.3	Results	139
6.3.1	Steady-State Wire Deflections	140
6.3.2	Snapshots	141
6.3.3	Force Plots	143
6.3.4	Comparison to Real Line-Test Data	147
6.3.5	Simulation Speed	149

6.3.6	Limitations	150
6.4	Conclusions	151
7	Conclusions and Further Work	152
7.1	Conclusions	152
7.2	Further Work	153

List of Figures

1.1	Image of High Speed Two electric train [5]	4
1.2	Diagram of pantograph and overhead wires [6]	5
1.3	Image of a single-arm pantograph [9]	6
1.4	Image of a double-arm pantograph [7]	6
1.5	Image of TENSOREX system [8]	7
1.6	Image of Series 1 Great Western overhead line (credit: Furrer+Frey)	8
1.7	Image of a dropper [3]	9
1.8	Image of a registration arm on the Old Dalby test track [2]	10
2.1	Pantograph mass-spring-damper models	24
2.2	Diagram of deflection directions	29
2.3	Diagram of a single catenary section. The length of a single messenger span is shown by the green arrow and the length of a contact wire is shown by the blue arrow.	31
2.4	Diagram of registration-arm model. A is the fixed registration-arm support, B is the arm's centre of mass and C is the position of the contact wire. θ is positive when the centre line of the arm is above horizontal and negative when the centre line is below horizontal.	35
2.5	Diagram of structure of A_1	54
2.6	Plot of eigenvalue roll-off for BS:EN 50318:2002	57
2.7	Plot of frequency response of pantograph head excited by sinusoidal contact force with angular frequency ω	65
3.1	Plot of steady-state vertical wire deflections for BS:EN 50318:2002	69

3.2	Eigenvalues of catenary system in order of increasing magnitude for BS:EN 50318:2002	70
3.3	Plot of first eigenmode for BS:EN 50318:2002	71
3.4	Plot of 21 st eigenmode for BS:EN 50318:2002	71
3.5	Plot of 161 st eigenmode for BS:EN 50318:2002	72
3.6	Snapshot of vertical and horizontal wire deflections at 250 km/hour for BS:EN 50318:2002	73
3.7	Plot of contact force against time for BS:EN 50318:2002 at 250 km/hour .	80
3.8	Plot of contact force against time for BS:EN 50318:2002 at 300 km/hour .	80
3.9	Plot of contact forces against pantograph position for BS:EN 50318:2002	81
4.1	Image of single span taken from BS:EN 50318:2018	86
4.2	Snapshot of total (static and dynamic) vertical wire deflections at 275 km/hour for BS:EN 50318:2018	92
4.3	Plot of contact forces against time for BS:EN 50318:2018 at 275 km/hour	100
4.4	Plot of contact forces against time for BS:EN 50318:2018 at 320 km/hour	101
5.1	A triggered subsystem in Simulink	110
5.2	An enabled subsystem in Simulink	111
5.3	Snapshot 1 of vertical wire deflections at 275 km/hour with events	113
5.4	Snapshot 2 of vertical wire deflections at 275 km/hour with events	113
5.5	Snapshot 1 of vertical and wire deflections at 320 km/hour with events . .	114
5.6	Snapshot 2 of vertical wire deflections at 320 km/hour with events	115
5.7	Plot of contact forces against time for the first wire at 275 km/hour with events	115
5.8	Plot of contact forces against time for the first wire at 320 km/hour with events	116
5.9	Zoomed-in plot of contact forces against time for the first wire at 320 km/hour with events	116

5.10	Plot of contact forces against time for the second wire at 275 km/hour with events	117
5.11	Plot of contact forces against time for the second wire at 320 km/hour with events	117
5.12	Plot of contact forces against time for the pantographs at 275 km/hour with events	118
5.13	Plot of contact forces against time for the pantographs at 320 km/hour with events	118
5.14	Plot of contact forces against time for the front pantograph as it transitions from the first wire to the second at 320 km/hour	119
5.15	Plot of contact forces against time for all wires and pantographs at 275 km/hour with events	120
5.16	Plot of contact forces against time for all wires and pantographs at 320 km/hour with events	120
6.1	Plot of steady-state, vertical wire deflections for the Old Dalby test track .	127
6.2	Plot of steady-state, horizontal wire deflections for the Old Dalby test track	128
6.3	Plot of values of S and F against horizontal position for first catenary system in contact with one pantograph, with the first eigenmode eliminated	132
6.4	Plot of values of S and F against horizontal position for second catenary system in contact with one pantograph, with the first eigenmode eliminated	132
6.5	Plot of values of S and F against horizontal position for fifth catenary system in contact with one pantograph, with the first eigenmode eliminated	133
6.6	Plot of values of S and F against horizontal position for fifth catenary system in contact with one pantograph, with the second eigenmode elim- inated	133
6.7	Plot of values of S and F against horizontal position for sixth catenary system in contact with one pantograph, with the first eigenmode eliminated	134

6.8	Zoomed-in plot of values of S and F against horizontal position for sixth catenary system in contact with one pantograph, with the first eigenmode eliminated	134
6.9	Plot of determinants of S and F against horizontal position for first catenary system in contact with two pantographs, with the first and second eigenmodes eliminated	135
6.10	Plot of determinants of S and F against horizontal position for first catenary system in contact with two pantographs, with the sixth and seventh eigenmodes eliminated	136
6.11	Plot of determinants of S and F against horizontal position for second catenary system in contact with two pantographs, with the first and second eigenmodes eliminated	136
6.12	Plot of determinants of S and F against horizontal position for sixth catenary system in contact with two pantographs, with the first and second eigenmodes eliminated	137
6.13	Image of arcing due to loss of contact on the Old Dalby track (credit: Furrer+Frey)	138
6.14	Snapshot of vertical and horizontal wire deflections of Old Dalby test track with one pantograph at 115 mph	141
6.15	Snapshot of vertical and horizontal wire deflections of Old Dalby test track with two pantographs at 115 mph	142
6.16	Plot of contact forces against time for the Old Dalby test track at 80 mph with a single pantograph	143
6.17	Plot of contact forces against time for the Old Dalby test track at 100 mph with a single pantograph	143
6.18	Plot of contact forces against time for the Old Dalby test track at 110 mph with a single pantograph	144
6.19	Plot of contact forces against time for the Old Dalby test track at 115 mph with a single pantograph	144

6.20	Plot of contact forces against time for the Old Dalby test track at 80 mph with two pantographs	145
6.21	Plot of contact forces against time for the Old Dalby test track at 100 mph with two pantographs	145
6.22	Plot of contact forces against time for the Old Dalby test track at 110 mph with two pantographs	146
6.23	Plot of contact forces against time for the Old Dalby test track at 115 mph with two pantographs	146

List of Tables

2.1	Table of modal properties for two-mass pantograph model from BS:EN 50318:2002	27
2.2	Table of modal properties for three-mass pantograph model from BS:EN 50318:2018	27
3.1	Table of pantograph constants for validation against BS:EN 50318:2002 . .	68
3.2	Table of results for validation against BS:EN 50318:2002	81
3.3	Comparison of results from Simulink and MATLAB for BS:EN 50318:2002	82
3.4	Simulink simulation speeds for BS:EN 50318:2002	83
4.1	Table of 275 km/hour results for validation against BS:EN 50318:2018 . .	102
4.2	Table of 320 km/hour results for validation against BS:EN 50318:2018 . .	102
4.3	Table of simulation speeds for BS:EN 50318:2018	103
5.1	Table of 275 km/hour results for model with events	121
5.2	Table of 320 km/hour results for model with events	121
5.3	Comparison of simulation speeds with and without events at 275 km/hour	122
5.4	Comparison of simulation speeds with and without events at 320 km/hour	122
6.1	Table of frequency properties of catenary model and pantograph model . .	139
6.2	Table of Old Dalby results with a single pantograph	147
6.3	Table of Old Dalby results for the front pantograph	148
6.4	Table of Old Dalby results for the rear pantograph	148
6.5	Table of simulation speeds for the Old Dalby model	149

Glossary of Terms

Symbol	Meaning	Typical Value
\dot{a}	Time derivative	-
a'	Space derivative	-
a^T	Transpose	-
$a_p(t)$	Horizontal acceleration of pantograph	-
A	Cross-sectional area of contact wire	$1.21 \times 10^{-4} \text{m}^2$
A^m	Cross-sectional area of messenger wire	$1.54 \times 10^{-4} \text{m}^2$
c_1	Pantograph damper stiffness	10Nsm^{-1}
c_1^s	Messenger-support damper stiffness at start of span	$5 \times 10^3 \text{Nsm}^{-1}$
c_2^s	Messenger-support damper stiffness at end of span	$5 \times 10^3 \text{Nsm}^{-1}$
E	Young's modulus of contact wire	$1.20 \times 10^{11} \text{Nm}^{-2}$
E^m	Young's modulus of messenger wire	$1.20 \times 10^{11} \text{Nm}^{-2}$
$F(\underline{x}_p(t))$	Term in $\ddot{\underline{q}}_1$ -equation to be inverted	-
$F_{d,i,j}(t)$	Tension in j^{th} dropper of i^{th} messenger span	-
g	Gravitational acceleration	9.81ms^{-2}
h_0	Initial contact-wire height	5m
I	Second moment of area of contact wire	$1.16 \times 10^{-9} \text{m}^4$
I^m	Second moment of area of messenger wire	$1.89 \times 10^{-9} \text{m}^4$
$J_{r,k}$	Moment of inertia of k^{th} registration arm	0.33kgm^{-2}
$k_{d,i,j}$	Stiffness of j^{th} dropper of i^{th} messenger span	$1 \times 10^5 \text{Nm}^{-1}$
k_1	Pantograph spring stiffness	$4.2 \times 10^3 \text{Nm}^{-1}$
k_1^s	Messenger-support spring constant at start of span	$5 \times 10^5 \text{Nm}^{-1}$
k_2^s	Messenger-support spring constant at end of span	$5 \times 10^5 \text{Nm}^{-1}$

Symbol	Meaning	Typical Value
L	Length of contact wire	600m
L^m	Length of messenger wire	60m
$L_{r,k}$	Length of k^{th} registration arm	1m
m	End-to-end contact-wire gradient	$\pm 1 \times 10^{-4}$ m
m_1	Mass of pantograph block	7.2kg
$m_{r,k}$	Mass of k^{th} registration arm	1kg
N_d	Number of droppers on messenger-wire span	9
N^m	Number of messenger wire-spans along contact wire	10
N_{modes}	Number of dynamic eigenmodes	204
N^p	Number of dynamic, horizontal contact-wire modes	204
N_q	Number of dynamic, vertical contact-wire modes	204
N_q^m	Number of dynamic, horizontal messenger-wire modes	204
N_r	Number of registration arms along contact wire	9
$p_n(t)$	Time function of horizontal contact-wire deflection	-
$\underline{p}(t)$	Vector of time components of horizontal contact-wire deflection	-
P	Axial tension of contact wire	2×10^4 N
P^m	Axial tension of messenger wire	1.6×10^4 N
P_v	Constant coefficient of aerodynamic pantograph force	7.7×10^{-3} Ns ² m ⁻²
P_1	Constant uplift force in three-mass pantograph model	90N
P_2	Constant uplift force in two-mass pantograph model	90N
$q_n(t)$	n^{th} time function of contact wire's vertical deflection	-
$\underline{q}(t)$	Vector of time components of contact wire's vertical deflection	-
$q_{i,n}^m(t)$	n^{th} time function of i^{th} messenger span's vertical deflection	-
$\underline{q}_i^m(t)$	Vector of time components of i^{th} messenger span's deflection	-
$\underline{\tilde{q}}(t)$	Vector of eigenmodes of DAE	-
$\underline{\tilde{q}}_1(t)$	Vector of eliminated eigenmodes of DAE	-
$\underline{\tilde{q}}_2(t)$	Vector of remaining eigenmodes of DAE	-

Symbol	Meaning	Typical Value
s_k	Transverse position of k^{th} registration-arm's contact point	$\pm 0.2\text{m}$
\underline{s}	Vector of transverse positions of registration-arm contact points	$\pm 0.2\text{m}$
$S(\underline{x}_p(t))$	Contact-constraint term to be inverted	-
t	Time	-
$\underline{u}(t)$	Vector of ODE position states	-
$\underline{v}(t)$	Vector of ODE velocity states	-
$v_p(t)$	Horizontal velocity of pantograph	275 km/hour
V	Left eigenvector matrix	-
$\underline{w}(t)$	Vector of ODE acceleration states	-
$\hat{w}(x, t)$	Total vertical deflection of contact wire	-
$\bar{w}(x, t)$	Steady-state vertical deflection of contact wire	-
$w(x, t)$	Dynamic vertical deflection of contact wire	-
$\hat{w}_i^m(x, t)$	Total vertical deflection of i^{th} messenger span	-
$\bar{w}_i^m(x, t)$	Steady-state vertical deflection of i^{th} messenger span	-
$w_i^m(x, t)$	Dynamic vertical deflection of i^{th} messenger span	-
$\hat{w}^p(x, t)$	Total horizontal deflection of contact wire	-
$\bar{w}^p(x, t)$	Steady-state horizontal stagger of contact wire	-
$w^p(x, t)$	Dynamic horizontal deflection of contact wire	-
W	Right eigenvector matrix	-
x	Horizontal position	-
$x_{d,i,j}$	Position of dropper of in contact wire's coordinate system	-
$x_{d,i,j}^m$	Position of dropper of in messenger span's coordinate system	-
$x_p(t)$	Horizontal position of pantograph	-
$x_p^f(t)$	Horizontal position of front pantograph	-
$x_p^b(t)$	Horizontal position of rear pantograph	-
$\underline{x}_p(t)$	Vector of horizontal pantograph positions	-
$x_{r,k}$	Horizontal position of the k^{th} registration arm	-

Symbol	Meaning	Typical Value
$z_1(t)$	Height of pantograph block	-
\bar{z}_1	Initial height of two-mass pantograph's head	-
\bar{z}_3	Initial height of three-mass pantograph's head	-
$z_3^f(t)$	Height of head of front pantograph	-
$z_3^b(t)$	Height of head of rear pantograph	-
$\underline{z}_3(t)$	Vector of pantograph head heights	-
$\alpha_{r,k}$	Angle of centre of mass of k^{th} registration arm	-
$\delta(t - \tau)$	Dirac Delta function centred at $t = \tau$	-
Δa	Change in a	-
ζ	Damping factor of catenary eigenmodes	0.02
η	Damping matrix	-
$\hat{\theta}_k(t)$	Total pitch angle of k^{th} registration arm	-
$\bar{\theta}_k$	Steady-state pitch angle of k^{th} registration arm	$\pm 0.1 \text{ rad}$
$\theta_k(t)$	Dynamic pitch angle of k^{th} registration arm	-
$\bar{\lambda}_{h,k}$	Steady-state, horizontal force exerted by k^{th} registration arm	$\pm 100 \text{ N}$
$\lambda_{h,k}(t)$	Dynamic, horizontal force exerted by k^{th} registration arm	-
$\lambda_{i,j}(t)$	Contact force between i^{th} contact wire and j^{th} pantograph	90N
$\bar{\lambda}_{v,k}$	Steady-state, vertical force exerted by k^{th} registration arm	$\pm 10 \text{ N}$
$\lambda_{v,k}(t)$	Dynamic, vertical force exerted by k^{th} registration arm	-
Λ	Diagonal matrix of eigenvalues	-
ρ	Density of contact wire	$8.89 \times 10^3 \text{ kg m}^{-3}$
ρ^m	Density of messenger wire	$8.89 \times 10^3 \text{ kg m}^{-3}$
$\phi_n(x)$	Spatial basis function of vertical contact-wire deflection	-
$\underline{\phi}(x)$	Vector of spatial basis functions of vertical contact-wire deflection	-
$\phi_{i,n}^m(x)$	Spatial basis function of i^{th} messenger wire's vertical deflection	-
$\underline{\phi}_i^m(x)$	Vector of spatial basis functions for i^{th} messenger wire	-

Chapter 1

Introduction and Literature Review

1.1 Introduction

1.1.1 History

In 1802, the Surrey Iron Railway opened, becoming the first public freight railway [39]. This was a horse-drawn plateway with a cast-iron track. Since then, gradual and continual progress has been made in train and railway design.

The first successful steam locomotive was Stephenson's Rocket. In 1829, the Rocket won the Rainhill Trials, which were hosted by the Liverpool and Manchester Railway, the first railway intended for passengers more so than freight. The train averaged 12 mph, with a top speed of 30 mph.

The world's first electric passenger train was presented at the Berlin Industrial Exhibition in 1879 [33]. Britain followed suit four years later, when Magnus Volk opened an electric railway in Brighton [56]. His train derived power from two electrified rails and could achieve a top speed of 6 mph, far from the current world record of 357 mph.

In 1902, the first commercially successful petrol locomotive was used for the Deptford Cattle Market in London. Ten years later, the first diesel-powered locomotive was operated on the Winterthur-Romanshorn railway in Switzerland. Since then, diesel has become the most common fuel used in trains across the world. However, due to issues with sustainability and pollution, it is desirable to move away from diesel power and to-

wards renewable energy sources.

An overview of the history of overhead electrification is given in [18]. Britain's first overhead electrification system opened to the public in 1909, with other overhead catenary systems following in the 1920s and 1930s. Initially, these systems were constrained by the immaturity of alternating-current (AC) motor technology and the limitations of direct current (DC) transmission. For these reasons, overhead electrification was only suitable for suburban and freight systems, with heavy electrical loads being used over short distances.

In the 1950s, there was increased interest in AC electrification due to increased reliability of electricity supplies. This made high-voltage, long-distance AC transmission a reality and paved the way for electric passenger trains. In the same decade, the French state railway SNCF began experimental runs of electric trains intended for passenger use. In 1955, they achieved the record-breaking speed of 326 km/hour using a modified 1500V DC system.

In modern times, overhead electrification systems are commonplace for passenger trains across the world. However, [18] also describes the difficulties in securing funding for new electrification projects. Therefore, most of the work done on electrification systems involves upgrading and maintaining existing overhead lines, rather than installing new ones. New overhead systems are generally only constructed for new railway lines, such as the High Speed Two (HS2) railway, which is currently in the early stages of construction in the UK.

1.1.2 Background

Numerous methods of power delivery exist for trains, including petrol, diesel, electricity and hydrogen. Petrol and diesel are reliable and easy to store, but are not sustainable and lead to a large carbon footprint. Electric trains are more environmentally friendly, since they produce less carbon dioxide. Furthermore, electric trains do not carry their own fuel, so there is more space on board for passengers or cargo.

There is great interest in renewable energy sources for trains. For this reason, diesel-

electric hybrids have become common across the UK. These trains are fitted with a diesel engine, as well as an electric motor and an electric generator. They run on electricity when possible, using the diesel engine when there is not enough electrical power available.

Hydrogen-powered engines have also been suggested as a solution to the problems with diesel. It is explained in [55] that environmental concerns are a major factor in the technological development of internal combustion engines. The combustion of hydrogen with oxygen only produces water, so there are no issues with harmful emissions. However, while hydrogen is abundant, storing it is currently very costly, both monetarily and in terms of energy. Therefore, hydrogen engines are not a suitable option for most commercial trains in the short term.

Overhead power lines for trains, shown in Figure 1.6, are currently a common form of power delivery and many further electrification projects are underway throughout Europe. In the UK, HS2 [4] is a huge project in which 530km of new track is being constructed with overhead lines in order to accommodate high-speed trains travelling at up to 400 km/hour. An HS2 electric train is shown in Figure 1.1.

Two methods of railway electrification have been used: the electric train can either receive power from a third rail on the ground or from an overhead contact wire. The overhead line's main advantages over the third rail are greater voltage (25kV vs 800V in the UK), which reduces losses, and higher train speed because it avoids problems with the current collector coming into contact with the third rail. Although the high voltage seems dangerous, it is ensured that overhead line is out of reach of anyone standing nearby.

The overhead catenary system consists of a contact wire supported by a messenger wire through a system of vertical droppers, with registration arms maintaining the horizontal stagger of the contact wire. The stagger is the horizontal zigzag pattern of the contact wire, which is primarily used to spread the wear across the pantograph head. The train collects electrical power from the contact wire using the pantograph, which is a metal framework on the roof of the train.

The messenger wire is supported above each registration arm, whereas the contact wire's only static supports are at its ends. In modern systems, both wires are tensioned by

TENSOREX [8] systems, which compensate for the thermal expansion and contraction of the wires, keeping their tensions constant. In older systems, large weights were used to tension the wires.

The design of overhead line equipment has largely been done by trial and error in the past, which has meant that overhead systems do not perform well as train speeds increase. Since real line tests are expensive, pantograph-catenary modelling software is a crucial part of modern overhead-system design. The analysis of pantograph-catenary systems is challenging, due to the various components in the catenary system, as well as the contact between the pantograph and the contact wire. The contact leads to more complications when there are multiple pantographs and multiple wires, especially when the pantographs are close together and their dynamics are coupled.

This thesis presents software that takes a Galerkin approach, also known as spectral analysis, instead of the usual finite-element methods (FEM). This software is intended for use in the design of new pantograph-catenary systems. The greatest problem with current FEM software is that it is very slow, so it is difficult to test significant numbers of pantograph designs, catenary configurations and train velocity profiles. The Galerkin approach offers greater simulation speed, enabling the simulation of many ‘what if?’ scenarios. While the Galerkin approach has been used for pantograph-catenary simulation in the past, this work aims to greatly increase the complexity and produce a model which can be used to simulate many real-world pantograph-catenary systems.



Figure 1.1: Image of High Speed Two electric train [5]

1.1.3 The Pantograph

The pantograph is illustrated in Figure 1.2. It is a metal framework mounted on the roof of the train, acting as a current collector. A graphite contact strip on the pantograph head is used to transfer electrical power from the contact wire to the train. The contact strip is typically about one metre wide, with horned ends to reduce the probability of hook over, where the contact wire loops around the pantograph head and becomes entangled underneath.

The main goal of pantograph design is to achieve a consistent contact force between the pantograph head and the contact wire. High contact forces lead to excessive wear on the contact strip and contact wire, increasing the cost of overhead-system maintenance. Conversely, if the contact force is too low, there is a risk of loss of contact, which interrupts power delivery and causes arcing.

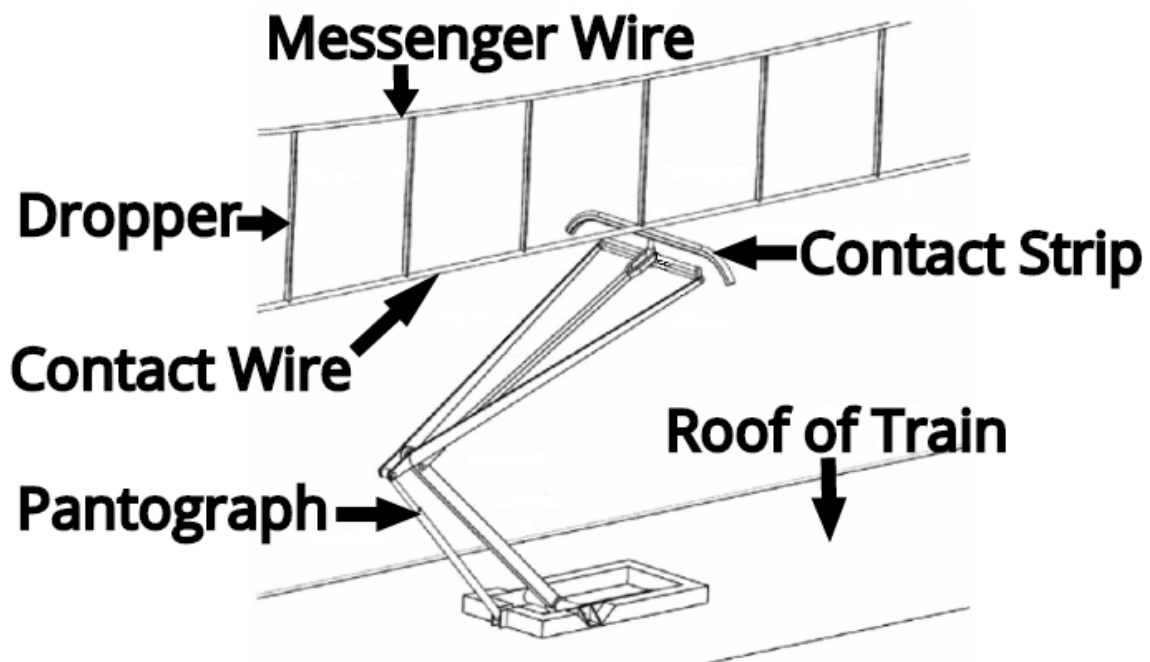


Figure 1.2: Diagram of pantograph and overhead wires [6]

The pantograph generally has two modes of movement: a slow, long-range mode that allows the pantograph to connect to contact wires of varying heights and a fast mode that allows the pantograph head to track small variations in contact-wire sag due to droppers, registration arms and the wire's self-weight. Various pantograph designs exist and

different models are better suited to different overhead catenary systems. It is desirable to design the pantograph to be suitable for a wide variety of overhead systems, because different countries use vastly different catenary designs.

There are two general categories: single-arm pantographs (Figure 1.3) and double-arm pantographs (Figure 1.4). The single-arm pantograph is generally preferred for electric trains due to its responsiveness at high speeds [1].



Figure 1.3: Image of a single-arm pantograph [9]



Figure 1.4: Image of a double-arm pantograph [7]

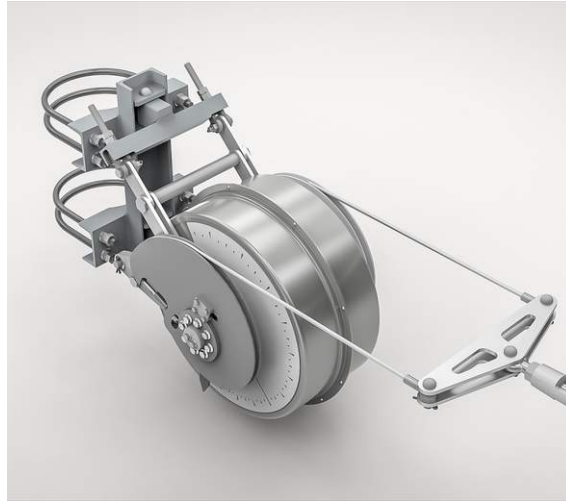


Figure 1.5: Image of TENSOREX system [8]

1.1.4 The Overhead Line

Overhead Wires

The contact wire is formed by extruding a copper-silver alloy and is used to deliver electrical power to the train via the pantograph. The messenger wire, on the other hand, is a stranded bronze-alloy cable and is allowed to sag substantially, so long as the contact wire is flat. The contact wire is typically around 4m above the ground and the messenger wire is about one metre above the contact wire. These heights are chosen so that the contact wire has sufficient clearance from the train roof and so that anyone standing near the track will be far from the high-voltage contact wire.

In modern overhead systems, the contact wire is held flat by support from the TENSOREX devices, droppers and registration arms in order to ensure a consistent contact force between it and the contact strip of the pantograph. The TENSOREX system, shown in Figure 1.5, maintains the contact-wire tension, which is typically around 20kN. These devices use the combination of a spiral spring and an eccentric disc to produce the tensioning force. Previously, large masses were used to hang from the ends of the wires, but the TENSOREX devices are more compact and far less dangerous in the event that the wire becomes detached from the tensioning device.

Each dropper is clamped to both the contact wire and messenger wire, exerting an upward force on the contact wire and a downward force on the messenger. The registration



Figure 1.6: Image of Series 1 Great Western overhead line (credit: Furrer+Frey)

arms are primarily used to maintain the horizontal contact-wire stagger, but they also exert upward forces on the wire. The pantograph exerts an additional upward contact force on the wire as it moves along.

The messenger wire is also tensioned at its ends by a TENSOREX system, commonly to about 16kN in the UK, and is supported at the end of each messenger span by a static support. Each dropper exerts a downward force on the messenger wire and the messenger is not in contact with the registration arms or pantograph.

The Droppers

A dropper is a braided wire with clamps on its ends to attach to the contact wire and messenger wire, as shown in Figure 1.7. The dropper can be considered as acting like a linear spring in tension, but only exerts a small buckling force in compression.

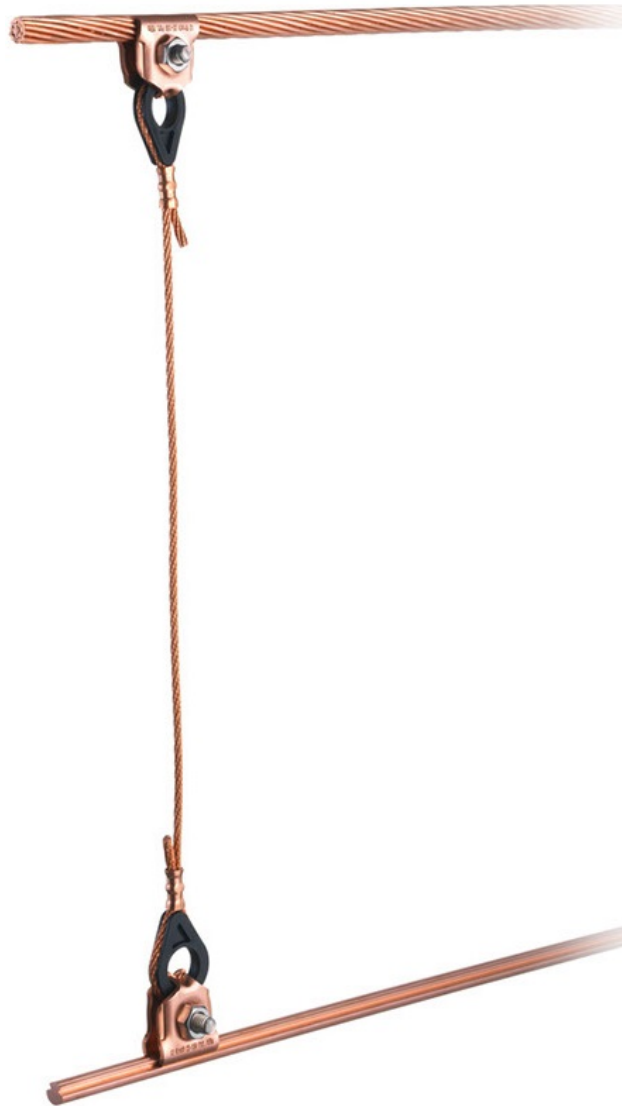


Figure 1.7: Image of a dropper [3]

There are typically five to ten droppers per messenger span, placed at roughly regular intervals. The droppers allow the messenger wire to support the contact wire and minimise the contact-wire sag. The contact wire's cross section is designed to allow the droppers to clamp on to the wire without disrupting the pantograph's movement along the wire.

The Registration Arms

A registration arm, pictured in Figure 1.8, is a stiff tube that is fixed at one end and attached to the contact wire at the other. The main purpose of a registration arm is to maintain the contact wire's horizontal stagger, which is typically $\pm 0.2\text{m}$. The stagger spreads the wear across the contact strip, as well as allowing the point of contact to remain near the centre of the pantograph head while the train turns a corner.



Figure 1.8: Image of a registration arm on the Old Dalby test track [2]

1.1.5 The Importance of Pantograph-Catenary Modelling

The primary use of pantograph-catenary modelling software is to aid the design of overhead systems. As train speeds increase, pantograph and catenary designs must be adapted. Real line tests are expensive, so it is necessary to simulate the pantograph-catenary interaction. It is desirable to have fast simulation speeds, which allow many OLE designs and ‘what if?’ scenarios to be tested. The model can also be used to test the compatibility of a pantograph with various overhead lines.

Another important concept is predictive maintenance. In order to maximise the number of trains that can run each day, the maintenance downtime must be minimised. There

is a physical New Measurement Train, which is used to assess the condition of the contact wire, but its top speed is 200 km/hour and it cannot detect problems that arise only at higher speeds. Furthermore, the measurement train takes up space on the track, whereas simulations do not.

Simulation software can be used to determine which parts of the overhead line are worn and require maintenance, meaning that few maintenance workers are required and they know where to focus their attention. The contact force measured in the physical overhead system is compared to the force profile calculated by the simulation, allowing the software to determine the wear of the contact wire as a function of position. This allows faults to be detected quickly and cheaply, even in parts of the overhead line that are difficult to check physically.

1.1.6 Outline of Thesis

In Section 1.2, literature on pantograph-catenary modelling and the numerical solution of differential-algebraic equations (DAEs) is reviewed. There is extensive literature on both, which provides ample guidance for this work.

In Chapter 2, the mathematical model used for the pantograph-catenary system is detailed. Four potential methods of DAE solution are explained and the most suitable is chosen. A step-by-step outline of the full solution process is provided.

Chapter 3 and Chapter 4 cover the validation against the 2002 and 2018 European Standards, BS:EN 50318:2002 and BS:EN 50318:2018 respectively. The specifications are explained, the results are presented and conclusions are drawn.

In Chapter 5, contact events are added to the model. The pantograph is able to come in and out of contact with each wire, allowing the pantograph's transition from one wire to the next to be simulated. The results with events are verified by comparison to those for BS:EN 50318:2018.

In Chapter 6, the final Simulink model is presented. This model loads in the pantograph-catenary system from a database and can be used to simulate a real overhead line, consisting of many differing catenary systems. The Old Dalby test track is used to validate

this model.

Chapter 7 concludes the thesis. The results from previous chapters are used to draw conclusions about the performance of the model and the usefulness of the Galerkin approach. Many further improvements to the software are suggested.

1.2 Literature Review

Pantograph-catenary modelling for high-speed trains has been researched extensively, with studies dating back as far as 1964. In [37], early dynamic pantograph-catenary simulation software was written in Fortran IV. In 1968, the effects of various design changes were studied, such as changing the steady-state sag, pantograph separation, pantograph stiffness, pantograph damping, dropper stiffness and dropper spacing [29]. These changes were all found to significantly affect the standard deviation of the contact force between the pantograph and the contact wire. The pantograph-catenary interaction is still an important research topic, because train speeds are increasing and new OLE designs are required.

1.2.1 The Pantograph

The model used for the pantograph varies greatly between studies. This is primarily due to the trade-off between realism and simulation speed, with the nonlinear and hardware-in-the-loop approaches being far more complex than the linear, lumped-mass model.

The hardware-in-the-loop approach involves a numerical catenary model being used to physically stimulate a real pantograph. The details of open-loop and closed-loop hardware-in-the-loop methods are explained in [23]. The open-loop method uses a predetermined pantograph excitation, whereas the closed-loop method allows the pantograph to interact with the dynamic simulation. Good agreement is found between the open-loop and closed-loop results. Despite the excellent accuracy of hardware-in-the-loop methods, which have been verified by comparison to line-test data, this approach is generally avoided due to the high complexity and low simulation speed.

Multibody pantograph models are commonly used [10, 11, 20, 47–49, 51, 52]. These models are able to capture the nonlinear pantograph dynamics and realistically describe the pantograph response. In [12], a linear finite-element catenary model is used in conjunction with a multibody pantograph, providing realistic pantograph dynamics at the expense of low simulation speed. This model is used to analyse the quality of contact between the pantograph and contact wire.

The simplest of the popular pantograph models is the lumped-mass or mass-spring-damper model used in [19, 41]. It is explained in [48] that the mass-spring-damper constants are chosen to match the experimentally measured frequency response of the pantograph. These models neglect the nonlinearities in the pantograph dynamics, but do not require co-simulation and therefore substantially reduce the complexity and increase the simulation speed.

Research has also been conducted on physical pantograph design. In [45], it is noted that catenary designs vary substantially between countries and this leads to pantographs being designed for specific catenary types. Contact wires using direct current require greater current and therefore greater contact force than alternating-current lines. Since overhead lines are generally only constructed for new track due to prohibitive cost, it is desirable to design pantographs that are compatible with many different catenary systems.

1.2.2 Finite-Element Methods (FEM)

The majority of pantograph-catenary simulation software uses FEM to solve the Euler-Bernoulli beam equations for the catenary system [11, 19, 41, 47–49, 52]. Typically, the only nonlinear effect included in the FEM model is dropper unloading.

In finite-element analysis, the overhead catenary system is spatially discretised into a finite set of simplified elements. Each element is chosen to be very small, so that the global solution can be accurately represented by this finite set of local approximations. For instance, the contact wire could be approximated as a set of 1m-long sections in a piecewise-linear arrangement.

FEM software provides excellent accuracy, especially close to the point of contact.

However, the short lengths of individual elements mean that the number of degrees of freedom of the overall solution must be very large, which leads to slow simulation speeds.

1.2.3 The Galerkin Approach

This study takes an alternative approach, based on the Galerkin method, also known as modal analysis. For each wire, the horizontal and vertical deflections are each separated into an infinite series of spatial basis functions and corresponding time functions. This method was used in [25] to model a moving point force on an axially loaded beam, which is analogous to a very simple pantograph-catenary model. The propagation of waves through the beam is studied and it is shown that the interference between these waves is a strong function of the speed of the moving force.

The Solution Process

Each wire is modelled as an Euler-Bernoulli beam, with vertical deflection $w(x, t)$.

$$\rho A \frac{\delta^2 w(x, t)}{\delta t^2} = -EI \frac{\delta^4 w(x, t)}{\delta x^4} + P \frac{\delta^2 w(x, t)}{\delta x^2} - \rho A g \quad (1.1)$$

where x is the horizontal position, t time, ρ the density of the wire, A the cross-sectional area, E Young's modulus, I the second moment of area, P the axial tension and g the acceleration due to gravitation.

The vertical deflection is decomposed into a series of spatial eigenmodes, $\phi_n(x)$ and corresponding functions of time, $q_n(t)$.

$$\rho A \phi_n(x) \ddot{q}_n(t) = -EI \phi_n''''(x) q_n(t) + P \phi_n''(x) q_n(t) - \rho A g \quad (1.2)$$

The boundary conditions are used to determine the spatial basis functions. For a simple pinned-pinned wire, these boundary conditions are given by (1.3).

$$\phi_n(0) = \phi_n''(0) = \phi_n(L) = \phi_n''(L) = 0 \quad (1.3)$$

where L is the length of the wire.

By analysing (1.2) for an unmoving wire and applying these boundary conditions, these $\phi_n(x)$ -terms can be evaluated. For an unmoving wire, (1.2) becomes (1.4).

$$0 = -EI\phi_n''''(x)\bar{q}_n + P\phi_n''(x)\bar{q}_n - \rho Ag \quad (1.4)$$

where \bar{q}_n is a constant.

Any solution to (1.4) must be an exponential, so $\phi_n(x)$ is of the form

$$\phi_n(x) = c_1 e^{\alpha x} + c_2 e^{-\alpha x} + c_3 \cos(\beta x) + c_4 \sin(\beta x) \quad (1.5)$$

where c_i , α and β are constants.

It can be seen by substituting (1.5) into (1.3) that, for a pinned-pinned wire, $\phi_n(x) = \sin\left(\frac{n\pi}{L}x\right)$ is the only function that satisfies all four boundary conditions. This expression is substituted into (1.2). Both sides are multiplied by $\phi_n(x)$, then integrated with respect to space between 0 and L to remove the dependence on x .

$$\begin{aligned} \int_0^L \rho A \sin^2(\beta_n x) \ddot{q}_n(t) dx = \\ \int_0^L -EI\beta_n^4 \sin^2(\beta_n x) q_n(t) + P\beta_n^2 \sin^2(\beta_n x) q_n(t) - \rho Ag \sin(\beta_n x) dx \end{aligned} \quad (1.6)$$

$$\frac{\rho A}{2} \ddot{q}_n(t) = -\left(\frac{EI}{2}\beta_n^4 + \frac{P}{2}\beta_n^2\right) q_n(t) + \frac{\rho Ag}{\beta_n} \cos(\beta_n x) \quad (1.7)$$

The partial differential equation (PDE) in space and time has been reduced to an ordinary differential equation (ODE) in time. Now, it can easily be solved by numerical integration.

1.2.4 Energy in the System

The energy in the overhead system can be evaluated as the sum of the kinetic energy (KE) and gravitational potential energy (GPE) for each component. For a wire, an infinitesimal slice of length Δx and mass $\rho A \Delta x$ is considered.

$$KE + GPE = \frac{1}{2}\rho A\Delta x\dot{w}^2(x, t) \quad (1.8)$$

$$GPE = \rho A\Delta xgw(x, t) \quad (1.9)$$

The energy in the whole wire is calculated by integrating (1.8) with respect to position.

$$KE + GPE = \int_0^L \frac{1}{2}\rho A\Delta x\dot{w}^2(x, t) + \rho A\Delta xgw(x, t)dx \quad (1.10)$$

Once the ODE has been solved and the vertical deflection of the wire is known for all positions and times, the energy in the wire can easily be evaluated. The same is true for droppers, registration arms and other overhead components.

The energy in the system has not been analysed in this thesis. However, the software presented here is capable of measuring the energy as a function of time using the results that have already been obtained.

Advantages Over FEM

The Galerkin approach approximates the global solution as a linear combination of basis functions at different spatial frequencies. These basis functions are global approximations, as opposed to the local approximations of the FEM approach. This allows realistic wire deflections to be modelled with relatively few degrees of freedom so long as the maximum spatial frequency is sufficiently low.

The Galerkin method was chosen to improve the simulation speed; it is hypothesised that the number of eigenmodes required to produce realistic results will be less than the number of FEM states, so the Galerkin approach will give faster simulation speed.

1.2.5 The Pantograph Position Constraint

The algebraic position constraint ensures that the height of the pantograph head and the vertical contact-wire deflection are in agreement. The constraint can be incorporated directly into the system of equations, yielding an index-three differential-algebraic equation

(DAE), but it is more common to use other techniques to ensure that the constraint is satisfied. A penalty method is used for the sliding-joint contact model in [11, 20]. In [19], a contact spring is used to model the compression of the contact strip and contact wire, which removes the contact constraint and gives an ODE.

1.2.6 Numerical Solution of DAEs

The dynamics of the overhead line and pantograph form an ordinary differential equation. However, an algebraic contact constraint is required to keep the pantograph and contact wire in contact. This gives rise to a DAE [13] which is nontrivial to solve numerically. The main focus of this thesis is on realistically and efficiently solving this DAE.

DAEs can be categorised by their differential indices. The differential index is the minimum number of times any one equation must be differentiated in order to reduce the DAE to an ODE. DAEs with differential indices greater than two are generally difficult to solve directly, so index-reduction methods are often applied.

Index-three DAEs are typical for constrained mechanical systems; they are not specific to the pantograph-catenary interaction. DAEs describing general multibody systems are discussed in [46] and it is explained that numerical solution methods differ greatly between stiff and nonstiff DAEs. Much of the research that has been done on general DAEs is applicable to pantograph-catenary systems. The general form of a DAE is given by (1.11), where the first equation is an ODE and the second is the set of algebraic constraints.

$$\begin{aligned}\dot{\underline{x}}(t) &= \underline{f}(\underline{x}(t), \underline{y}(t), t) \\ \underline{0} &= \underline{g}(\underline{x}(t), \underline{y}(t), t)\end{aligned}\tag{1.11}$$

where $\underline{x}(t)$ and $\underline{y}(t)$ are state vectors, $\underline{f}(\underline{x}(t), \underline{y}(t), t)$ the system's equations of motion and $\underline{g}(\underline{x}(t), \underline{y}(t), t)$ the algebraic constraints.

DAE problems fall into two general categories: initial-value problems (IVPs) and boundary-value problems (BVPs). IVPs are typically more straightforward to solve, be-

cause tools such as the backward differentiation formula (BDF) can be used [21]. The literature covers many different BVP solution methods for high-index DAEs, such as the one considered in this thesis. Four methods are outlined below.

- The position constraint can be differentiated with respect to time twice to reduce the differentiation index to one, or three times to reduce the DAE to its underlying ODE. This gives a tractable equation, but can lead to difficulty in evaluating the initial conditions and also leads to numerical drift in the position constraint [27]. Various ways of eliminating the numerical drift have been suggested, such as the introduction of additional variables to allow the simultaneous inclusion of the position, velocity and acceleration constraints in the DAE [42].
- The solution can be confined to a manifold on which the algebraic constraints are always satisfied [50], meaning that the DAE is reduced to an ODE. One way to find such a manifold is to apply the position constraints and their first two time derivatives in order to algebraically eliminate the constraint forces and constraint equations [40]. This is generally not advised for nonlinear DAEs, because the algebraic elimination of variables must be performed at each time step.
- Collocation methods can be used [14, 15, 32]. The solution is restricted to a finite-dimensional space, usually polynomials of finite index, and a set of collocation points is used to find the solution: whichever polynomial satisfies the equation at all of the collocation points is selected.
- The GGL formulation, which was originally presented in [28], can be utilised. The position and velocity constraints are both applied, using a fictitious force for each velocity constraint. This reduces the differential index to two without causing numerical drift.

The index-three DAE considered in this study is a time-varying, linear DAE, whereas the literature primarily covers nonlinear DAEs. Therefore, elimination of variables, which is inadvisable for nonlinear DAEs, is an appropriate consideration for pantograph-catenary modelling.

Once the index of a DAE has been sufficiently reduced, it can be solved using a numerical-integration algorithm, of which there are many available. For low-index DAEs, an algorithm such as MATLAB's ode15s can be used. ode15s is designed to solve stiff differential equations and DAEs. In this study, the pantograph-catenary DAE was reduced to an ODE and solved using MATLAB's ode45, which is based on an explicit Runge-Kutta (4,5) formula. ode45 was chosen due its speed in solving ODEs.

1.2.7 Contact-Wire Transitions

As a pantograph nears the end of a contact wire, it comes into contact with the next contact wire and then leaves contact with the old wire. The pantograph's transition from one wire to the next is investigated in [19].

For each catenary system, the DAE is of the form shown in (1.12), where the top row is the ODE and the bottom row is the set of algebraic constraints. Adjacent wires' dynamics are coupled only through the contact force acting on a pantograph that is in contact with both wires.

$$\begin{pmatrix} M & 0 \\ 0 & 0 \end{pmatrix} \begin{pmatrix} \ddot{\underline{q}}_i \\ \ddot{\underline{\lambda}}_i \end{pmatrix} + \begin{pmatrix} C_i & 0 \\ 0 & 0 \end{pmatrix} \begin{pmatrix} \dot{\underline{q}}_i \\ \dot{\underline{\lambda}}_i \end{pmatrix} + \begin{pmatrix} K_i & \phi_i^T \\ \phi_i & 0 \end{pmatrix} \begin{pmatrix} \underline{q}_i \\ \underline{\lambda}_i \end{pmatrix} = \begin{pmatrix} \underline{R}_i \\ \underline{0} \end{pmatrix} \quad (1.12)$$

where M is the mass matrix, C_i the damping matrix, K_i the stiffness matrix, ϕ_i the matrix of algebraic constraints, \underline{q}_i the state vector of the catenary system, $\underline{\lambda}_i$ the vector of contact forces and \underline{R}_i the vector of state-independent terms.

In a transition span, where two adjacent catenary systems overlap, there are four possible contact conditions for each pantograph:

1. The pantograph is in contact with neither wire.
2. The pantograph is in contact with only the first wire.
3. The pantograph is in contact with only the second wire.
4. The pantograph is in contact with both wires.

When the pantograph is in a transition span, both of the overlapping catenaries must be modelled simultaneously and the simulation software must detect changes in contact condition. When the pantograph is in contact with both contact wires, each wire exerts a separate contact force on the pantograph head.

Impact Mechanics

There is ample literature on impact modelling [53], including the interaction between a rigid body and an Euler-Bernoulli beam [26]. Immediately before a pantograph makes contact with a contact wire, there is a mismatch between the velocity of the pantograph head and the wire velocity at the point of contact [54]. Most modern impact-modelling methods resolve this mismatch by assuming the impact is instantaneous and allowing an infinite contact force to account for the discontinuities in velocity.

Impact modelling can predict complicated and unhelpful phenomena, such as infinite chatter [43, 44], which is an infinite number of impacts in a finite timespan, and indeterminate motion. These are numerical phenomena caused by the approximations used in the impact model. Various ideas have been presented to improve the numerical solution of impact problems, including the calculation of a continuous, finite contact force [57].

1.2.8 Wear Modelling

Predicting the wear of the contact wire and pantograph head is an important part of pantograph-catenary modelling. This can be done using on-board cameras [36] or by measuring the contact force and electrical current [24], then using the wear model to predict the condition of the overhead system. Wear modelling allows predictive maintenance to be performed and is particularly useful for sections of the overhead line that are rarely inspected physically. Image processing can also be used to detect faults such as overheating of the pantograph's contact strip, arcing and irregular positioning of the contact wire [16]. While wear modelling is closely related to the work presented here, it is outside the scope of this thesis

1.2.9 Aerodynamic Effects

Another important aspect of pantograph-catenary simulation which is not covered in this thesis is aerodynamic modelling. Numerous studies have considered the effects of wind on the pantograph-catenary system. The effects of cross-wind on the pantograph-catenary interaction are explained in [47]: cross-wind causes a lateral displacement in the catenary wires, as well as a variation in the pantograph uplift force. The pantograph must stay in contact with the contact wire even when there is powerful wind, so aerodynamic modelling is important.

When extreme wind speeds are measured in the UK, a blanket speed restriction is applied to all nearby trains. In [31], an active pantograph is designed to react to these wind conditions and allow trains to continue at their regular speeds. When extreme wind conditions are detected by the rotation of the pantograph's torsion bar, the pantograph uplift force is increased in order to regulate the contact force.

1.3 Contributions

This thesis investigates whether a Galerkin approach can provide faster simulation speeds than FEM for pantograph-catenary modelling without compromising realism.

The following goals have been achieved.

- Pantograph-catenary simulation software has been developed in MATLAB and Simulink.
- The Galerkin approach has been used to model an idealised catenary system. Dropper unloading, registration arms, multiple pantographs and transition events have all been successfully included in the model.
- The model has been validated against the European Standards BS:EN 50318:2002 and BS:EN 50318:2018. High simulation speed has been obtained without compromising the realism.
- The model has been generalised to simulate the overhead line for a real track. The dropper arrangement and registration-arm positions can be different for each cate-

nary system and each overhead wire is allowed to have a vertical and transverse horizontal gradient. The details of the pantograph and overhead line are read in from a spreadsheet and passed to the Simulink model when they are required.

Chapter 2

Modelling

2.1 Introduction

In this chapter, the mathematical model of the overheard system is explained in depth. The equations of motion for each component are given and then used to form an overall DAE. The process used to solve this DAE is explained and the reasons for choosing this process over other possibilities are discussed.

2.2 The Mathematical Model

2.2.1 The Pantograph

The pantograph is designed to track large, gradual changes in contact-wire height as well as small, abrupt changes due to droppers and registration arms. This is achieved using two stages of pantograph elevation: a slow, long-range stage and a fast, short-range stage. The pantograph head is lifted into contact and held in contact with the overhead wire by exerting a constant uplift force on the bottom of the pantograph. This uplift force is produced by a pneumatic actuator

In this study, the pantograph was modelled as a mass-spring-damper system [30]. The topology and parameters were prescribed based on the frequency response of the pantograph; they are not derived here, but they were chosen to match the frequency response

of the real pantograph. Pantograph models with two and three masses were used, with a constant uplift force applied to the bottom mass in order to keep the pantograph head in contact with the contact wire. The equations of motion for the pantographs represented by Figure 2.1a and Figure 2.1b are given by (2.1)-(2.2) and (2.3)-(2.5), respectively.

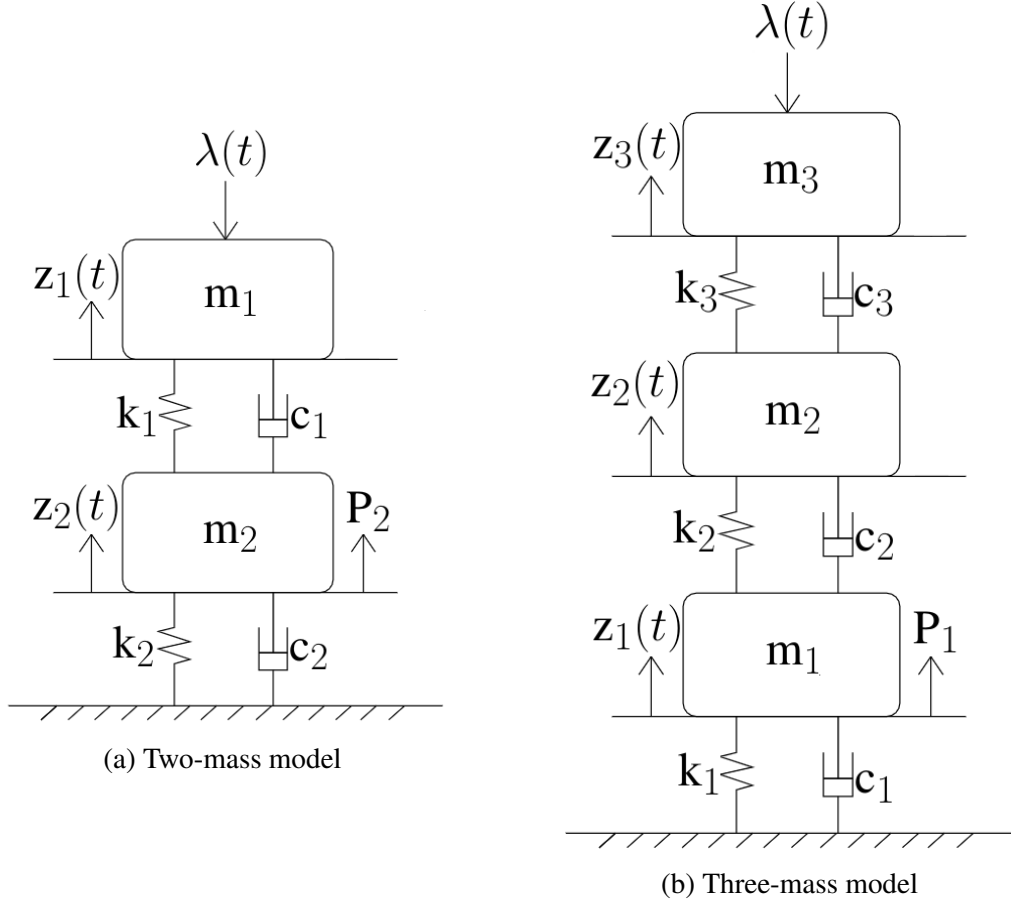


Figure 2.1: Pantograph mass-spring-damper models

The evaluation of the pantograph's parameters is explained in [48]. The lumped-mass model is derived through a series of laboratory tests. The masses, stiffnesses and damping properties are set to match the frequency response of the physical pantograph.

A pantograph generally consists of two arms in the 'Z'-shape which support a horned head with a graphite contact strip, as shown in Figure 1.3. The top mass of the model always represents the pantograph head. For a three-mass model, each of the lower masses represents one of the arms and the springs and dampers represent the joints between these arms and the head. However, for some pantographs, it is empirically observed that the frequency response of the pantograph can be realistically matched by a two-mass model

[30]. In this case, the lower mass represents both of the pantograph arms.

Two-Mass Model

$$m_1 \ddot{z}_1(t) = -c_1 \dot{z}_1(t) + c_1 \dot{z}_2(t) - k_1 z_1(t) + k_1 z_2(t) - \lambda(t) \quad (2.1)$$

$$m_2 \ddot{z}_2(t) = c_1 \dot{z}_1(t) - (c_1 + c_2) \dot{z}_2(t) + k_1 z_1(t) - (k_1 + k_2) z_2(t) + P_2 \quad (2.2)$$

where m_i is the mass of the i^{th} pantograph block, $z_i(t)$ the vertical displacement of the i^{th} pantograph block, c_i the i^{th} damping coefficient, k_i the i^{th} spring constant, $\lambda(t)$ the downward contact force exerted on the pantograph head and P_2 the constant uplift force applied to the bottom pantograph block.

Three-Mass Model

$$m_1 \ddot{z}_1(t) = -(c_1 + c_2) \dot{z}_1(t) + c_2 \dot{z}_2(t) - (k_1 + k_2) z_1(t) + k_2 z_2(t) + P_1 \quad (2.3)$$

$$m_2 \ddot{z}_2(t) = c_2 \dot{z}_1(t) - (c_2 + c_3) \dot{z}_2(t) + c_3 \dot{z}_3(t) + k_2 z_1(t) - (k_2 + k_3) z_2(t) + k_3 z_3(t) \quad (2.4)$$

$$m_3 \ddot{z}_3(t) = c_3 \dot{z}_2(t) - c_3 \dot{z}_3(t) + k_3 z_2(t) - k_3 z_3(t) - \lambda(t) \quad (2.5)$$

where P_1 is the constant uplift force applied to the bottom pantograph block.

Modal Properties

The modal properties of the two-mass and three-mass pantograph models were analysed for the pantographs that will be used in Chapter 3 and Chapter 4, respectively. This analysis began with the general form of the equations of motion of an unforced pantograph, given by (2.6). This was obtained by combining (2.1)-(2.2) or (2.3)-(2.5).

$$M \ddot{\underline{z}}(t) = C \dot{\underline{z}}(t) + K \underline{z}(t) \quad (2.6)$$

where $\underline{z}(t)$ is the vector of vertical displacements, M the mass matrix, C the damping matrix and K the stiffness matrix.

For an undamped pantograph, (2.6) reduces to (2.7).

$$M\ddot{\underline{z}}(t) = K\underline{z}(t) \quad (2.7)$$

The general solution is a combination of real exponentials and sinusoids. However, there is no damping or external excitation, there cannot be any exponential decay or growth in the oscillations of the masses. Therefore, the solution is a sinusoid.

$$\underline{z}(t) = Ae^{j\omega_{0,i}t} \quad (2.8)$$

where A is a constant matrix and $\omega_{0,i}$ is a natural frequency of the system.

Substituting (2.8) into (2.7) gives

$$-\omega_{0,i}^2 \underline{z}(t) = M^{-1}K\underline{z}(t) \quad (2.9)$$

Using eigenvector decomposition, (2.9) can be reformulated in terms of decoupled eigenmodes.

$$M^{-1}K = V\Lambda W = V\Omega_0^2 W \quad (2.10)$$

where $W = V^{-1}$ and Ω_0 is the diagonal matrix of natural frequencies.

$$\ddot{\underline{z}}(t) = V\Omega_0^2 W\underline{z}(t) \quad (2.11)$$

$$\ddot{\underline{z}}(t) = V\Omega_0^2 W\underline{z}(t) \quad (2.12)$$

$$W\ddot{\underline{z}}(t) = WV\ddot{\underline{z}}(t) = \ddot{\underline{\tilde{z}}}(t) = \Omega_0^2 \underline{\tilde{z}}(t) \quad (2.13)$$

where $\underline{\tilde{z}} = W\underline{z}$ is the vector of eigenmodes of the undamped system.

To approximate the damping factor of the pantograph, the same diagonalisation was applied to the damped system, (2.6).

$$\ddot{\tilde{\mathbf{z}}}(t) = \tilde{C}\dot{\tilde{\mathbf{z}}}(t) + \Omega_0^2\tilde{\mathbf{z}}(t) \quad (2.14)$$

where $\tilde{C} = WM^{-1}CV$.

The modes of the damped system, $\tilde{\mathbf{z}}$, are coupled by the off-diagonal damping terms in \tilde{C} . These off-diagonal terms were ignored in order to analyse each mode independently and find the approximate damping factor.

$$\ddot{\tilde{z}}_i(t) = \tilde{c}_i\dot{\tilde{z}}_i(t) + \omega_{0,i}^2\tilde{z}_i(t) \quad (2.15)$$

$$\zeta_i = \frac{\tilde{c}_i}{2\omega_{0,i}} \quad (2.16)$$

where ζ_i is the damping factor of the i^{th} mode.

The results of performing this analysis on the two-mass pantograph model that will be used in Chapter 3 and the three-mass pantograph model that will be used in Chapter 4 are shown in Table 2.1 and Table 2.2, respectively.

Mode number, i	Natural frequency, $\omega_{0,i}$ (rad/s)	Damping factor, ζ_i
1	29.40	0.07
2	1.50	1.35

Table 2.1: Table of modal properties for two-mass pantograph model from BS:EN 50318:2002

Mode number, i	Natural frequency, $\omega_{0,i}$ (rad/s)	Damping factor, ζ_i
1	69.00	0.09
2	35.73	0.16
3	2.66	0.82

Table 2.2: Table of modal properties for three-mass pantograph model from BS:EN 50318:2018

In each case, the off-diagonal terms in \tilde{C} were found to be within an order of magnitude of the diagonal terms. Since the damping factors are significant, especially for the

low-frequency modes, the magnitude of the off-diagonal terms suggests that the damping elements introduce significant modal coupling into the pantograph dynamics.

Suitability

It is explained in [30] that these linear pantograph models have been extensively validated against experimental and laboratory results. They have also been validated against nonlinear multibody models. Furthermore, the findings presented in this thesis demonstrate that a linear mass-spring-damper pantograph model can be used to produce realistic results from pantograph-catenary simulations.

The main advantage of the mass-spring-damper model is that it is simple and computationally efficient. The co-simulation of a linear catenary model and multibody pantograph is very slow and for many applications, it is desirable to model the pantograph-catenary system linearly in order to greatly improve the simulation speed. However, for some purposes, it is important to model the pantograph-catenary interaction extremely realistically close to the point of contact. In these cases, the linear model is not appropriate and either a multibody model or a hardware-in-the-loop model should be used.

2.2.2 The Contact Wire

The contact wire was modelled as an Euler-Bernoulli beam, as shown in (2.17)-(2.24), where $\hat{w}(x, t)$ is the wire's total vertical deflection and $\hat{w}^p(x, t)$ is the wire's total horizontal deflection. These directions are clarified in Figure 2.2. For a contact wire which is staggered in a zigzag pattern, the x -axis is parallel to the train tracks, rather than the contact wire.

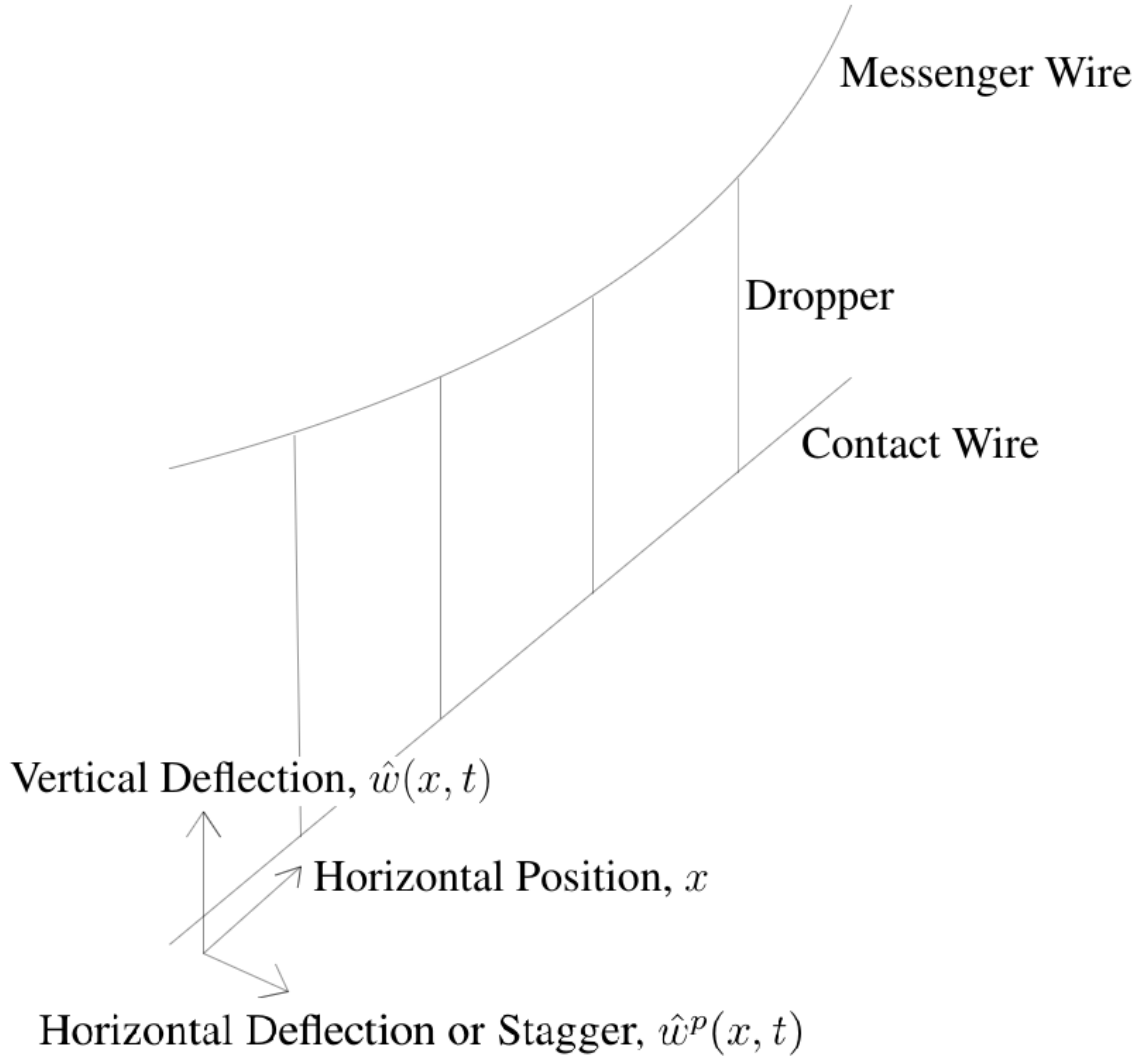


Figure 2.2: Diagram of deflection directions

Each wire is hundreds of metres long, but less than a centimetre in radius, so they are extremely slender and the Euler-Bernoulli beam equation is justified [17]. The right-hand terms represent the bending stiffness, tension, self-weight and contact force respectively. The forces from droppers, registration arms and messenger supports have been omitted and will be added later.

There is also friction between the pantograph head and the contact wire. The frictional force acts in the line of motion of the train, but the contact wire is laterally staggered, so there are transverse and longitudinal components of friction acting on the contact wire. A typical contact force is around 200N, so a rough estimate of the frictional force is 100N. This is two orders of magnitude less than the contact-wire tension, so the longitu-

dinal component can be neglected. For a typical OLE arrangement, the horizontal stagger between two adjacent registration arms is three orders of magnitude smaller than the distance between the registration arms. Therefore, the transverse force can be estimated to be around 0.1N and can also be neglected.

Vertical Deflection

$$\rho A \frac{\partial^2 \hat{w}(x, t)}{\partial t^2} = -EI \frac{\partial^4 \hat{w}(x, t)}{\partial x^4} + P \frac{\partial^2 \hat{w}(x, t)}{\partial x^2} - \rho A g + \lambda(t) \delta(x - x_p(t)) \quad (2.17)$$

where x is the horizontal position, t the time, ρ the contact-wire density, A the cross-sectional area, $\hat{w}(x, t)$ the total wire deflection, E Young's modulus, I the second moment of area, P the axial tension, g the gravitational constant, $x_p(t)$ the horizontal pantograph position and δ the Dirac Delta function.

The contact force, $\lambda(t)$, acts upwards on the contact wire, hence the positive sign. Since the Euler-Bernoulli beam equation is formulated in terms of force per unit length, a point force appears in the equation as an impulse in the space domain.

Horizontal Deflection

$$\rho A \frac{\partial^2 \hat{w}^p(x, t)}{\partial t^2} = -EI \frac{\partial^4 \hat{w}^p(x, t)}{\partial x^4} + P \frac{\partial^2 \hat{w}^p(x, t)}{\partial x^2} \quad (2.18)$$

where $\hat{w}^p(x, t)$ is the total horizontal contact-wire deflection. When $\hat{w}^p(x, t) = 0$, the wire sits on the centre line between the two TENSOREX supports at its ends.

In this thesis, 'stagger' refers to the steady-state component of the horizontal deflection of a wire, whereas 'horizontal deflection' refers to the dynamic component or total deflection.

The self-weight and contact force act vertically, so they do not appear in the horizontal equation. The horizontal stagger of the system described by 2.18 would be zero for all x and t , but more terms will be added when the registration arms are put into the model and these will give nonzero horizontal deflection.

Boundary Conditions

The TENSOREX contact-wire supports do not exert a bending moment, so the contact wire is free to rotate. The wire was therefore modelled as a pinned-pinned beam with boundary conditions

$$\hat{w}(0, t) = \hat{w}''(0, t) = \hat{w}(L, t) = \hat{w}''(L, t) = 0 \quad (2.19)$$

where L is the contact-wire length.

2.2.3 The Messenger Wire

The messenger wire was modelled as a series of Euler-Bernoulli beams. Each messenger span was considered separately, giving one equation for each span. A messenger span is defined as the section between two consecutive messenger-wire supports, which are found at the ends of the contact wire and above each registration arm.

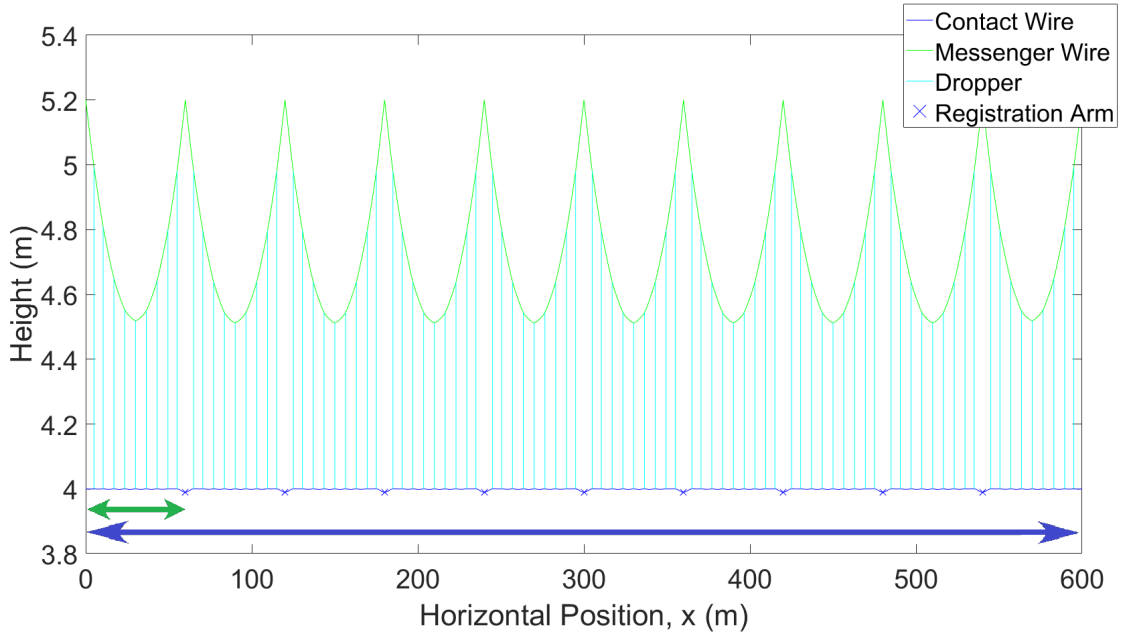


Figure 2.3: Diagram of a single catenary section. The length of a single messenger span is shown by the green arrow and the length of a contact wire is shown by the blue arrow.

Vertical Deflection

$$\rho^m A^m \frac{\partial^2 \hat{w}_i^m(x, t)}{\partial t^2} = -E^m I^m \frac{\partial^4 \hat{w}_i^m(x, t)}{\partial x^4} + P^m \frac{\partial^2 \hat{w}_i^m(x, t)}{\partial x^2} - \rho^m A^m g \quad (2.20)$$

where x is the horizontal position in the messenger span's coordinate system, ρ^m the messenger-wire density, A^m the cross-sectional area, $\hat{w}_i^m(x, t)$ the deflection of the i^{th} messenger span, E^m Young's modulus, I^m the second moment of area and P^m the axial tension.

The pantograph does not make contact with the messenger wire, so there is no contact force in (2.20).

Horizontal Deflection

It is assumed that no external, horizontal forces act on the messenger wire. In reality, each dropper exerts a lateral force due to the horizontal deflection of the contact wire relative to the messenger wire, but these deflections were found to be so small that the lateral dropper forces were negligible.

With no horizontal forces, the horizontal deflection of the messenger wire is zero for all time. The messenger-wire stagger matches the registration-arm arrangement in a partwise-linear zigzag pattern.

Boundary Conditions

At its ends, the messenger is supported by TENSOREX devices. In Chapter 3, the messenger supports above the registration arms are also considered pinned and each messenger span is modelled as pinned-pinned.

$$\hat{w}_i^m(0, t) = \hat{w}_i^{m''}(0, t) = \hat{w}_i^m(L^m, t) = \hat{w}_i^{m''}(L^m, t) = 0 \quad (2.21)$$

where L^m is the messenger-wire length.

From Chapter 4 onwards, the messenger is supported by a spring and a damper above each registration arm is free to move vertically. Therefore, the messenger wire is modelled as pinned-free-free-...-free-free-pinned, as shown in (2.22) - (2.24).

First Messenger Span

$$\hat{w}_i^m(0, t) = \hat{w}_i^{m''}(0, t) = \hat{w}_i^{m''}(L^m, t) = \hat{w}_i^{m'''}(L^m, t) = 0 \quad i = 1 \quad (2.22)$$

Middle Messenger Spans

$$\hat{w}_i^{m''}(0, t) = \hat{w}_i^{m'''}(0, t) = \hat{w}_i^{m''}(L^m, t) = \hat{w}_i^{m'''}(L^m, t) = 0 \quad 1 < i < N^m \quad (2.23)$$

Last Messenger Span

$$\hat{w}_i^{m''}(0, t) = \hat{w}_i^{m'''}(0, t) = \hat{w}_i^m(L^m, t) = \hat{w}_i^{m''}(L^m, t) = 0 \quad i = N^m \quad (2.24)$$

where N^m is the number of messenger spans in the catenary system.

2.2.4 The Droppers

Along a messenger span, there are typically multiple droppers connecting the contact wire and messenger wire. The droppers were modelled as linear springs in tension. The spring constant of each dropper is usually specified, but this could be calculated by modelling the braided wire if necessary. The weights of the dropper and its clamps were ignored initially, but were added to the model as point forces before validating against the 2018 European Standard.

The masses of the droppers were neglected from the equations of motion, as they were found to be very small relative to the total mass of the wires between two adjacent droppers. Using the typical values given in the glossary, the mass of the contact wire between droppers is 6.5kg and the mass of the messenger wire is 8.2kg, which gives a total of 14.7kg. Using values from the 2018 European Standard, the total mass of a dropper of length 1m and its clamps is 0.47kg.

Dropper unloading was neglected in the initial model and is introduced in Section 4.2.2. Without unloading, the droppers act as linear springs even in compression, but in reality, they exert only a small buckling force when compressed.

$$F_{d,i,j}(t) = k_{d,i,j} (w_i^m(x_{d,i,j}^m, t) - w(x_{d,i,j}, t)) \quad (2.25)$$

where $F_{d,i,j}(t)$ is the tension in the j^{th} dropper of the i^{th} messenger span, $k_{d,i,j}$ the dropper stiffness, $x_{d,i,j}$ the horizontal dropper position in the contact wire's coordinate system and $x_{d,i,j}^m$ the horizontal dropper position in the messenger span's coordinate system.

These forces were added to (2.17) and (2.20) as Dirac Delta functions, giving (2.26) and (2.27), respectively. Since the dropper tensions act vertically, they do not appear in the horizontal equations.

$$\begin{aligned} \rho A \frac{\partial^2 \hat{w}(x, t)}{\partial t^2} = & -EI \frac{\partial^4 \hat{w}(x, t)}{\partial x^4} + P \frac{\partial^2 \hat{w}(x, t)}{\partial x^2} - \rho A g + \lambda(t) \delta(x - x_p(t)) \\ & + \sum_{i=1}^{N^m} \sum_{j=1}^{N_d} (k_{d,i,j} (\hat{w}_i^m(x_{d,i,j}^m, t) - \hat{w}(x_{d,i,j}, t)) \delta(x - x_{d,i,j})) \end{aligned} \quad (2.26)$$

where N_d is the number of droppers on the messenger span.

$$\begin{aligned} \rho^m A^m \frac{\partial^2 \hat{w}_i^m(x, t)}{\partial t^2} = & -E^m I^m \frac{\partial^4 \hat{w}_i^m(x, t)}{\partial x^4} + P^m \frac{\partial^2 \hat{w}_i^m(x, t)}{\partial x^2} - \rho^m A^m g \\ & + \sum_{j=1}^{N_d} (k_{d,i,j} (\hat{w}(x_{d,i,j}, t) - \hat{w}_i^m(x_{d,i,j}^m, t)) \delta(x - x_{d,i,j}^m)) \end{aligned} \quad (2.27)$$

Each dropper also exerts a horizontal force on each wire, proportional to the horizontal deflection of the contact wire relative to the messenger wire. A typical deflection is around 1mm and a typical dropper is about 1m long, so this horizontal force is three orders of magnitude smaller than the vertical dropper force. Therefore, these horizontal forces were neglected.

2.2.5 The Registration Arms

Registration-Arm Rotation

The registration arms were modelled as stiff rods, with one end stationary and the other attached to the contact wire. The model is illustrated in Figure 2.4 and the dynamics of the k^{th} registration arm are given by (2.28).

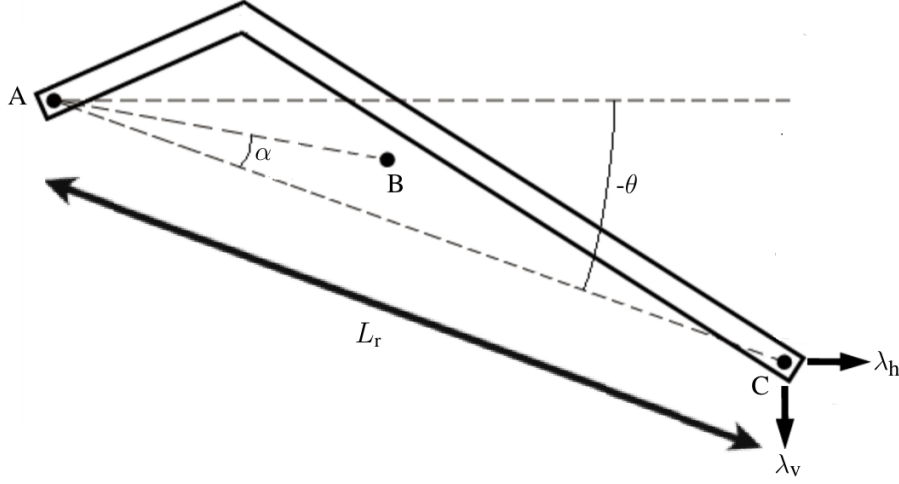


Figure 2.4: Diagram of registration-arm model. A is the fixed registration-arm support, B is the arm's centre of mass and C is the position of the contact wire. θ is positive when the centre line of the arm is above horizontal and negative when the centre line is below horizontal.

$$J_{r,k} \ddot{\hat{\theta}}_k(t) = -L_{r,k} \hat{\lambda}_{v,k}(t) \cos \hat{\theta}_k(t) - L_{r,k} \hat{\lambda}_{h,k}(t) \sin \hat{\theta}_k(t) - m_{r,k} g \frac{L_{g,k}}{2} \cos \left(\hat{\theta}_k(t) - \alpha_k \right) \quad (2.28)$$

where $J_{r,k}$ is the moment of inertia of the k^{th} registration arm attached to the contact wire, α_k angle from the centre line to the centre of mass, $\hat{\theta}_k(t)$ the change in pitch from horizontal, $L_{r,k}$ the distance from the registration-arm support to the contact wire, $L_{g,k}$ the distance from the registration-arm support to the centre of mass, $\hat{\lambda}_{v,k}(t)$ the upward vertical force exerted on the contact wire by the registration arm, $\hat{\lambda}_{h,k}(t)$ the horizontal force exerted on the contact wire by the registration arm towards the registration-arm support, and $m_{r,k}$ the mass of the registration arm.

Each registration arm exerts a vertical force and a horizontal force, $\hat{\lambda}_{v,k}(t)$ and $\hat{\lambda}_{h,k}(t)$

respectively, on the contact wire. The vertical force is positive upwards and the horizontal force is positive towards the registration-arm support.

Vertical Contact-Wire Deflection

$$\begin{aligned} \rho A \frac{\partial^2 \hat{w}(x, t)}{\partial t^2} = & -EI \frac{\partial^4 \hat{w}(x, t)}{\partial x^4} + P \frac{\partial^2 \hat{w}(x, t)}{\partial x^2} - \rho A g + \sum_{k=1}^{N_r} \left(\hat{\lambda}_{v,k}(t) \delta(x - x_{r,k}) \right) \\ & + \sum_{i=1}^{N^m} \sum_{j=1}^{N_d} \left(k_{d,i,j} \left(\hat{w}_i^m(x_{d,i,j}^m, t) - \hat{w}(x_{d,i,j}, t) \right) \delta(x - x_{d,i,j}) \right) + \lambda(t) \delta(x - x_p(t)) \end{aligned} \quad (2.29)$$

where $x_{r,k}$ is the horizontal position of the k^{th} registration arm in the contact wire's coordinate system.

Horizontal Contact-Wire Deflection

$$\begin{aligned} \rho A \frac{\partial^2 \hat{w}^p(x, t)}{\partial t^2} = & -EI \frac{\partial^4 \hat{w}^p(x, t)}{\partial x^4} + P \frac{\partial^2 \hat{w}^p(x, t)}{\partial x^2} \\ & + \sum_{k=1}^{N_r} \left(\text{sign}(s_k) \hat{\lambda}_{h,k}(t) \delta(x - x_{r,k}) \right) \end{aligned} \quad (2.30)$$

where s_k is the transverse position of the k^{th} registration arm's contact point, defined as the displacement of the point of contact between the registration arm and the wire from the horizontal centre line of the contact wire.

Messenger-Wire Deflection

The registration arms are not in contact with the messenger wire, so there are no registration-arm terms in the messenger equations. However, the messenger wire does zigzag due to the locations of its supports so that it is directly above the contact wire. The registration arms affect the messenger-wire behaviour, but only through the contact wire and the droppers.

2.2.6 The Algebraic Constraints

In addition to the previously derived ODEs and PDEs, two sets of constraints must be satisfied to ensure that the registration arms remain in contact with the contact wire and

one constraint must be satisfied to ensure the pantograph head stays in contact. The time derivatives of these constraints must also be satisfied; these derivatives are later used to eliminate time derivatives of some ODE states.

Vertical Registration-Arm Position

$$\hat{w}(x_{r,k}, t) = L_{r,k} \sin \hat{\theta}_k(t) \quad (2.31)$$

(2.31) ensures that the vertical deflection of the registration arm matches that of the contact wire.

Horizontal Registration-Arm Position

$$\hat{w}^p(x_{r,k}, t) = s_k + L_{r,k} \text{sign}(s_k) \left(1 - \cos \hat{\theta}_k(t)\right) \quad (2.32)$$

(2.32) ensures that the horizontal deflection of the registration arm matches that of the contact wire.

Vertical Pantograph-Head Position

$$z_1(t) + \bar{z}_1 = \hat{w}(x_p(t), t) \quad (2.33)$$

where \bar{z}_1 is the initial height of the pantograph head relative to the contact-wire support height. The pantograph is at rest at this height when no uplift force is applied, so the uplift force raises the pantograph head up to the height of the contact wire. For the three-mass pantograph, $z_1(t)$ and \bar{z}_1 are replaced by $z_3(t)$ and \bar{z}_3 .

2.2.7 The Index-Three DAE

The equations are compiled here for clarity. The pantograph and wire dynamics form a system of ODEs and PDEs that must be solved in accordance with the algebraic constraints. Since the pantograph-position constraint would have to be differentiated three times to remove the algebraic constraints, the differential index is three.

Vertical Contact-Wire Dynamics

$$\begin{aligned} \rho A \frac{\partial^2 \hat{w}(x, t)}{\partial t^2} = & -EI \frac{\partial^4 \hat{w}(x, t)}{\partial x^4} + P \frac{\partial^2 \hat{w}(x, t)}{\partial x^2} - \rho A g + \sum_{k=1}^{N_r} \left(\hat{\lambda}_{v,k}(t) \delta(x - x_{r,k}) \right) \\ & + \sum_{i=1}^{N^m} \sum_{j=1}^{N_d} \left(k_{d,i,j} \left(\hat{w}_i^m(x_{d,i,j}^m, t) - \hat{w}(x_{d,i,j}, t) \right) \delta(x - x_{d,i,j}) \right) + \lambda(t) \delta(x - x_p(t)) \end{aligned}$$

Horizontal Contact-Wire Dynamics

$$\rho A \frac{\partial^2 \hat{w}^p(x, t)}{\partial t^2} = -EI \frac{\partial^4 \hat{w}^p(x, t)}{\partial x^4} + P \frac{\partial^2 \hat{w}^p(x, t)}{\partial x^2} + \sum_{k=1}^{N_r} \left(\text{sign}(s_k) \hat{\lambda}_{h,k}(t) \delta(x - x_{r,k}) \right)$$

Vertical Messenger-Wire Dynamics

$$\begin{aligned} \rho^m A^m \frac{\partial^2 \hat{w}_i^m(x, t)}{\partial t^2} = & -E^m I^m \frac{\partial^4 \hat{w}_i^m(x, t)}{\partial x^4} + P^m \frac{\partial^2 \hat{w}_i^m(x, t)}{\partial x^2} - \rho^m A^m g \\ & + \sum_{j=1}^{N_d} \left(k_{d,i,j} \left(\hat{w}(x_{d,i,j}, t) - \hat{w}_i^m(x_{d,i,j}^m, t) \right) \delta(x - x_{d,i,j}^m) \right) \end{aligned}$$

Registration-Arm Dynamics

$$J_{r,k} \ddot{\hat{\theta}}_k(t) = -L_{r,k} \hat{\lambda}_{v,k}(t) \cos \hat{\theta}_k(t) - L_{r,k} \hat{\lambda}_{h,k}(t) \sin \hat{\theta}_k(t) - m_{r,k} g \frac{L_{g,k}}{2} \cos \left(\hat{\theta}_k(t) - \alpha_k \right)$$

Vertical Registration-Arm Constraints

$$\hat{w}(x_{r,k}, t) = L_{r,k} \sin \hat{\theta}_k(t)$$

Horizontal Registration-Arm Constraints

$$\hat{w}^p(x_{r,k}, t) = s_k + L_{r,k} \text{sign}(s_k) \left(1 - \cos \hat{\theta}_k(t) \right)$$

Pantograph Constraint

$$z_1(t) + \bar{z}_1 = \hat{w}(x_p(t), t)$$

2.3 The Solution Process

2.3.1 Spatial Discretisation

Each wire deflection was split into its steady-state and dynamic components and then each component was expressed as an infinite series of spatial basis functions multiplied by a corresponding series of time functions. The steady-state equations include all of the static forces, whereas the dynamic equations include the contact force and other time-dependent forces.

Contact Wire - Vertical

$$\hat{w}(x, t) = \bar{w}(x, t) + w(x, t) = \sum_{n=1}^{\infty} (\bar{q}_n \phi_n(x)) + \sum_{n=1}^{\infty} (q_n(t) \phi_n(x)) \quad (2.34)$$

where $\bar{w}(x, t)$ is the steady-state, vertical contact-wire deflection, $w(x, t)$ the dynamic, vertical contact-wire deflection, $\phi_n(x)$ a spatial basis function, \bar{q}_n the corresponding steady-state time function and $q_n(t)$ the corresponding dynamic time function.

Contact Wire - Horizontal

$$\hat{w}^p(x, t) = \bar{w}^p(x, t) + w^p(x, t) = \sum_{n=1}^{\infty} (\bar{p}_n \phi_n(x)) + \sum_{n=1}^{\infty} (p_n(t) \phi_n(x)) \quad (2.35)$$

where $\bar{w}^p(x, t)$ is the steady-state, horizontal contact-wire deflection, $w^p(x, t)$ the dynamic, horizontal contact-wire deflection, \bar{p}_n the corresponding steady-state time function and $p_n(t)$ the corresponding dynamic time function.

The horizontal $\phi_n(x)$ -terms are the same as the vertical ones, because the wire length and boundary conditions are unchanged. However, the infinite series of $\phi_n(x)$ -terms can be truncated to different lengths for the vertical and horizontal deflections.

Messenger Wire - Vertical

$$\hat{w}_i^m(x, t) = \bar{w}_i^m(x, t) + w_i^m(x, t) = \sum_{n=1}^{\infty} (\bar{q}_{i,n}^m \phi_{i,n}(x)) + \sum_{n=1}^{\infty} (q_{i,n}^m(t) \phi_{i,n}(x)) \quad (2.36)$$

where $\bar{w}_i^m(x, t)$ is the steady-state, vertical messenger-span deflection, $w_i^m(x, t)$ the dynamic, vertical messenger-span deflection, $\phi_{i,n}^m(x)$ a spatial basis function, $\bar{q}_{i,n}^m$ the cor-

responding steady-state time function and $q_{i,n}^m(t)$ the corresponding dynamic time function.

(2.34) was substituted into (2.17), which was then split into (2.37) and (2.38). The same process was used to derive similar equations for the horizontal deflection of the contact wire and the vertical messenger-wire deflection.

Steady-State, Vertical Contact-Wire Deflection

$$0 = -EI \sum_{n=1}^{\infty} (\bar{q}_n \phi_n''''(x)) + P \sum_{n=1}^{\infty} (\bar{q}_n \phi_n''(x)) - \rho A g + \sum_{k=1}^{N_r} (\bar{\lambda}_{v,k} \delta(x - x_{r,k})) + \sum_{i=1}^{N^m} \sum_{j=1}^{N_d} \left(k_{d,i,j} \left(\sum_{n=1}^{\infty} (\bar{q}_{i,n}^m \phi_{i,n}^m(x_{d,i,j}^m, t)) - \sum_{n=1}^{\infty} (\bar{q}_n \phi_n(x_{d,i,j})) \right) \delta(x - x_{d,i,j}) \right) \quad (2.37)$$

where $\bar{\lambda}_{v,k}$ is the steady-state, vertical force exerted by the k^{th} registration arm on the contact wire.

Dynamic, Vertical Contact-Wire Deflection

$$\rho A \sum_{n=1}^{\infty} (\ddot{q}_n(t) \phi_n(x)) = -EI \sum_{n=1}^{\infty} (q_n(t) \phi_n''''(x)) + P \sum_{n=1}^{\infty} (q_n(t) \phi_n''(x)) + \sum_{i=1}^{N^m} \sum_{j=1}^{N_d} \left(k_{d,i,j} \left(\sum_{n=1}^{\infty} (q_{i,n}^m(t) \phi_{i,n}^m(x_{d,i,j}^m)) - \sum_{n=1}^{\infty} (q_n(t) \phi_n(x_{d,i,j})) \right) \delta(x - x_{d,i,j}) \right) + \sum_{k=1}^{N_r} (\lambda_{v,k}(t) \delta(x - x_{r,k})) + \lambda(t) \delta(x - x_p(t)) \quad (2.38)$$

where $\lambda_{v,k}(t)$ is the dynamic, vertical force exerted by the k^{th} registration arm on the contact wire.

Steady-State, Horizontal Contact-Wire Deflection

$$0 = -EI \sum_{n=1}^{\infty} (\bar{p}_n \phi_n^{p''''}(x)) + P \sum_{n=1}^{\infty} (\bar{p}_n \phi_n^{p''}(x)) + \sum_{k=1}^{N_r} (\text{sign}(s_k) \bar{\lambda}_{h,k} \delta(x - x_{r,k})) \quad (2.39)$$

where $\bar{\lambda}_{h,k}$ is the steady-state, horizontal force exerted by the k^{th} registration arm on the contact wire.

Dynamic, Horizontal Contact-Wire Deflection

$$\begin{aligned} \rho A \sum_{n=1}^{\infty} (p_n(t) \phi_n^p(x)) = & -EI \sum_{n=1}^{\infty} (p_n(t) \phi_n^{p''''}(x)) + P \sum_{n=1}^{\infty} (p_n(t) \phi_n^{p''}(x)) \\ & + \sum_{k=1}^{N_r} (\text{sign}(s_k) \lambda_{h,k} \delta(x - x_{r,k})) \end{aligned} \quad (2.40)$$

where $\lambda_{h,k}(t)$ is the dynamic, horizontal force exerted by the k^{th} registration arm on the contact wire.

Steady-State, Vertical Messenger-Wire Deflection

$$\begin{aligned} 0 = & -E^m I^m \sum_{n=1}^{\infty} (\bar{q}_{i,n}^m \phi_n^{m''''}(x)) + P^m \sum_{n=1}^{\infty} (\bar{q}_{i,n}^m \phi_n^{m''}(x)) - \rho^m A^m g \\ & + \sum_{j=1}^{N_d} \left(k_{d,i,j} \left(\sum_{n=1}^{\infty} (\bar{q} \phi_n^p(x_{d,i,j})) - \sum_{n=1}^{\infty} (\bar{q}_{i,n}^m \phi_n^p(x_{d,i,j}^m)) \right) \delta(x - x_{d,i,j}^m) \right) \end{aligned} \quad (2.41)$$

Dynamic, Vertical Messenger-Wire Deflection

$$\begin{aligned} \rho^m A^m \sum_{n=1}^{\infty} (\ddot{q}_{i,n}^m(t) \phi_n(x)) = & -E^m I^m \sum_{n=1}^{\infty} (q_{i,n}^m(t) \phi_n^{m''''}(x)) + P^m \sum_{n=1}^{\infty} (q_{i,n}^m(t) \phi_n^{m''}(x)) \\ & + \sum_{j=1}^{N_d} \left(k_{d,i,j} \left(\sum_{n=1}^{\infty} (q_n(t) \phi_n^p(x_{d,i,j})) - \sum_{n=1}^{\infty} (q_{i,n}^m(t) \phi_n^p(x_{d,i,j}^m)) \right) \delta(x - x_{d,i,j}^m) \right) \end{aligned} \quad (2.42)$$

2.3.2 Evaluation of Spatial Basis Functions

The boundary conditions given in Section 2.2.2 and Section 2.2.3 were used to evaluate the spatial basis functions, $\phi_n(x)$ and $\phi_{i,n}^m(x)$. Because the boundary conditions must hold for all time, they must be satisfied by the time-invariant basis functions, so they can be rewritten in terms of $\phi_n(x)$ and $\phi_{i,n}^m(x)$. The general form of $\phi_n(x)$ and $\phi_{i,n}^m(x)$ is given by (2.43).

$$\phi_n(x) = A e^{\alpha_n x} + B e^{-\alpha_n x} + C \cos(\beta_n x) + D \sin(\beta_n x) \quad (2.43)$$

Contact wire

The contact wire was modelled as pinned-pinned, because of the TENSOREX system at each end, and the boundary conditions were given by (2.19).

$$\phi_n(0) = \phi_n''(0) = \phi_n(L) = \phi_n''(L) = 0 \quad (2.44)$$

$$\phi_n(x) = \sin\left(\frac{n\pi x}{L}\right) = \sin(\beta_n x) \quad (2.45)$$

$$\beta_n = \frac{n\pi}{L} \quad (2.46)$$

In Chapter 3, each messenger span is considered to be pinned-pinned and $\phi_{i,n}^m(x)$ is entirely analogous to $\phi_n(x)$. In later chapters, spring-damper messenger supports are modelled and $\phi_{i,n}^m(x)$ varies between messenger spans.

Messenger Wire - First Span

The first messenger span was modelled as pinned-free, as the spring-damper supports allowed the free end of the messenger wire to move, so the boundary conditions were

$$\phi_n^m(0) = \phi_n^{m''}(0) = \phi_n^{m''}(L^m) = \phi_n^{m'''}(L^m) = 0 \quad (2.47)$$

These boundary conditions yield

$$\phi_n^m(x) = \left(\frac{\beta_n^m}{\alpha_n^m}\right)^2 \sin(\beta_n^m L^m) e^{-\alpha_n^m(L^m-x)} + \sin(\beta_n^m x) \quad (2.48)$$

This expression for $\phi_n^m(x)$ was substituted into (2.41), ignoring the self-weight and dropper forces, to evaluate α_n^m and β_n^m .

$$\alpha_n^{m2} = \frac{P^m}{2E^m I^m} \left(\sqrt{1 + \frac{4E^{m2} I^{m2} \omega^2}{P^{m2}}} - 1 \right) \quad (2.49)$$

$$\beta_n^{m2} = \frac{P^m}{2E^m I^m} \left(\sqrt{1 + \frac{4E^{m2} I^{m2} \omega^2}{P^{m2}}} + 1 \right) \quad (2.50)$$

$$\tan(\beta_n^m L^m) = \frac{\beta_n^m}{\alpha_n^m} \quad (2.51)$$

Messenger Wire - Middle Spans

The middle spans took free-free boundary conditions and the analysis used was analogous.

$$\phi_n^{m''}(0) = \phi_n^{m'''}(0) = \phi_n^{m''}(L^m) = \phi_n^{m'''}(L^m) = 0 \quad (2.52)$$

$$\begin{aligned} \phi_n^m(x) = & - \left(\frac{\beta_n^m}{\alpha_n^m} \right)^3 e^{-\alpha_n^m x} - \frac{\beta_n^m}{\alpha_n^m} \cos(\beta_n^m x) + \sin(\beta_n^m x) \\ & + \left(\frac{\beta_n^m}{\alpha_n^m} \right)^2 \left(\sin(\beta_n^m L^m) - \left(\frac{\beta_n^m}{\alpha_n^m} \right) \cos(\beta_n^m L^m) \right) e^{-\alpha_n^m (L^m - x)} \end{aligned} \quad (2.53)$$

Again, (2.41) was used to evaluate α_n^m and β_n^m .

$$\alpha_n^{m2} = \frac{P^m}{2E^m I^m} \left(\sqrt{1 + \frac{4E^{m2} I^{m2} \omega^2}{P^{m2}}} - 1 \right) \quad (2.54)$$

$$\beta_n^{m2} = \frac{P^m}{2E^m I^m} \left(\sqrt{1 + \frac{4E^{m2} I^{m2} \omega^2}{P^{m2}}} + 1 \right) \quad (2.55)$$

$$\tan(\beta_n^m L^m) = \frac{2\alpha_n^m \beta_n^m}{\alpha_n^{m2} - \beta_n^{m2}} \quad (2.56)$$

Messenger Wire - Last Span

The end span took free-pinned boundary conditions.

$$\phi_n^{m''}(0) = \phi_n^{m'''}(0) = \phi_n^m(L^m) = \phi_n^{m''}(L^m) = 0 \quad (2.57)$$

$$\phi_n^m(x) = - \left(\frac{\beta_n^m}{\alpha_n^m} \right)^3 e^{-\alpha_n^m x} - \frac{\beta_n^m}{\alpha_n^m} \cos(\beta_n^m L^m) + \sin(\beta_n^m x) \quad (2.58)$$

where α_n^m and β_n^m were given by (2.49)-(2.51).

2.3.3 Orthogonality Integrals

With all the $\phi(x)$ -terms evaluated, an orthogonality integral was used to reduce the PDE in $w(x, t)$ to an ODE in $q(t)$. Both sides were multiplied by $\phi_o(x)$ and integrated with respect to x between 0 and L (or L^m) for all $o \in \mathbb{Z}^+$, removing all $q_{n \neq o}(t)$ -terms. The same method was used for $p_n(t)$ and $q_{i,n}^m(t)$.

Orthogonality Properties

$$\int_0^L (\phi_n(x) \phi_o(x)) dx = 0 \quad \forall o \neq n \quad (2.59)$$

$$\int_0^L (\phi_n''(x) \phi_o(x)) dx = 0 \quad \forall o \neq n \quad (2.60)$$

$$\int_0^L (\phi_n'''(x) \phi_o'(x)) dx = 0 \quad \forall o \neq n \quad (2.61)$$

$$\int_0^L (\phi_n''''(x) \phi_o(x)) dx = 0 \quad \forall o \neq n \quad (2.62)$$

For the contact wire, $\phi_n(x) = \sin(\beta x)$, so each spatial derivative of $\phi_n(x)$ is also a sinusoid. Using the fact that sin- and cos-functions are orthogonal to themselves and one another for $n \neq o$, it can be seen that these orthogonality properties hold for all derivatives of $\phi_n(x)$ and $\phi_o(x)$.

For the messenger wire, $\phi_n(x)$ is, in general, the summation of two real exponential functions, a sin wave and a cos wave. These orthogonality properties are nontrivial to derive for a general $\phi_n(x)$, but they were verified both analytically and numerically for (2.48), (2.53) and (2.58).

Steady-State, Vertical Contact-Wire Deflection

$$\begin{aligned}
0 = & \left(-EI \int_0^L (\phi_n''''(x) \phi_n(x)) dx + P \int_0^L (\phi_n''(x) \phi_n(x)) dx \right) \bar{q}_n(t) \\
& - \rho Ag \int_0^L \phi_n(x) dx + \sum_{k=1}^{N_r} \left(\bar{\lambda}_{v,k} \int_0^L (\phi_n(x) \delta(x - x_{r,k})) dx \right) \\
& + \sum_{i=1}^{N^m} \sum_{j=1}^{N_d} \left(k_{d,i,j} \left(\sum_{n=1}^{\infty} (\bar{q}_{i,n}^m \phi_{i,n}^m(x_{d,i,j}^m, t)) - \sum_{n=1}^{\infty} (\bar{q}_n \phi_n(x_{d,i,j})) \right) \int_0^L (\phi_n(x) \delta(x - x_{d,i,j})) dx \right)
\end{aligned} \tag{2.63}$$

For the contact wire, $\phi_n(x) = \sin(\bar{\beta}_n x) = \sin(\beta_n x)$ and (2.63) simplifies to (2.64), where the $\bar{q}_n(t)$ -terms have been compiled into a column vector. The same deflection shapes were used for the wires' steady-state and dynamic components, so $\bar{\beta}_n = \beta_n$. However, different numbers of modes were included for each component, so it is useful to disambiguate between $\bar{\beta}$ and β .

$$\begin{aligned}
\mathbf{0} = & -\text{diag} \left\{ \frac{EI}{\rho A} \bar{\beta}^4 + \frac{P}{\rho A} \bar{\beta}^2 \right\} \bar{\underline{q}} - \frac{2g}{L} \int_0^L \sin(\bar{\beta} x) dx + \frac{2}{\rho AL} \sin(\bar{\beta} x_r^T) \bar{\underline{\lambda}}_v \\
& + \frac{2}{\rho AL} \sum_{i=1}^{N^m} \sum_{j=1}^{N_d} k_{d,i,j} \left(\sin(\bar{\beta} x_{d,i,j}) \left(\underline{\phi}^{mT}(x_d^m(j)) \bar{\underline{q}}_i^m(t) - \sin(\bar{\beta} x_{d,i,j})^T \bar{\underline{q}}(t) \right) \right)
\end{aligned} \tag{2.64}$$

where ' $\bar{\beta}^2$ ' has been used to denote the elementwise square of the vector $\bar{\beta}$.

$$\bar{\underline{q}}(t) = \begin{pmatrix} \bar{q}_1(t) \\ \bar{q}_2(t) \\ \vdots \\ \bar{q}_{N_{\bar{q}}}(t) \end{pmatrix} \tag{2.65}$$

$$\underline{\phi}(x) = \begin{pmatrix} \phi_1(x) \\ \phi_2(x) \\ \vdots \\ \phi_{N_{\bar{q}}}(x) \end{pmatrix} \tag{2.66}$$

$$\underline{\bar{\beta}} = \begin{pmatrix} \bar{\beta}_1 \\ \bar{\beta}_2 \\ \vdots \\ \bar{\beta}_{N_{\bar{q}}} \end{pmatrix} \quad (2.67)$$

$$\underline{\bar{\lambda}}_v = \begin{pmatrix} \bar{\lambda}_{v,1} \\ \bar{\lambda}_{v,2} \\ \vdots \\ \bar{\lambda}_{v,N_r} \end{pmatrix} \quad (2.68)$$

$$\underline{x}_r = \begin{pmatrix} x_{r,1} \\ x_{r,2} \\ \vdots \\ x_{r,N_r} \end{pmatrix} \quad (2.69)$$

Dynamic, Vertical Contact-Wire Deflection

$$\begin{aligned} \rho A \int_0^L \phi_n^2(x) dx \ddot{q}_n(t) &= \left(-EI \int_0^L (\phi_n''''(x) \phi_n(x)) dx + P \int_0^L (\phi_n''(x) \phi_n(x)) dx \right) q_n(t) \\ &+ \sum_{i=1}^{N^m} \sum_{j=1}^{N_d} \left(k_{d,i,j} \left(\sum_{n=1}^{\infty} (q_{i,n}^m(t) \phi_{i,n}^m(x_{d,i,j}^m, t)) - \sum_{n=1}^{\infty} (q_n(t) \phi_n(x_{d,i,j})) \right) \int_0^L (\phi_n(x) \delta(x - x_{d,i,j})) dx \right) \\ &+ \sum_{k=1}^{N_r} \left(\lambda_{v,k}(t) \int_0^L (\phi_n(x) \delta(x - x_{r,k})) dx \right) + \lambda(t) \int_0^L (\phi_n(x) \delta(x - x_p(t))) dx \end{aligned} \quad (2.70)$$

Substituting (2.45) gives

$$\begin{aligned} \ddot{\underline{q}}(t) &= -\text{diag} \left\{ \frac{EI}{\rho A} \underline{\beta}^4 + \frac{P}{\rho A} \underline{\beta}^2 \right\} \underline{q}(t) + \frac{2 \sin(\underline{\beta} x_p(t))}{\rho A L} \lambda(t) + \frac{2}{\rho A L} \sin(\underline{\beta} \underline{x}_r^T) \underline{\lambda}_v(t) \\ &+ \frac{2}{\rho A L} \sum_{i=1}^{N^m} \sum_{j=1}^{N_d} k_{d,i,j} \left(\sin(\underline{\beta} x_{d,i,j}) \left(\underline{\phi}^{mT}(x_{d,i,j}^m) \underline{q}_i^m(t) - \sin(\underline{\beta} x_{d,i,j})^T \underline{q}(t) \right) \right) \end{aligned} \quad (2.71)$$

$$\underline{q}(t) = \begin{pmatrix} q_1(t) \\ q_2(t) \\ \vdots \\ q_{N_q}(t) \end{pmatrix} \quad (2.72)$$

$$\underline{\phi}(x) = \begin{pmatrix} \phi_1(x) \\ \phi_2(x) \\ \vdots \\ \phi_{N_q}(x) \end{pmatrix} \quad (2.73)$$

$$\underline{\beta} = \begin{pmatrix} \beta_1 \\ \beta_2 \\ \vdots \\ \beta_{N_q} \end{pmatrix} \quad (2.74)$$

$$\underline{\lambda}_v(t) = \begin{pmatrix} \lambda_{v,1}(t) \\ \lambda_{v,2}(t) \\ \vdots \\ \lambda_{v,N_r}(t) \end{pmatrix} \quad (2.75)$$

Steady-State, Horizontal Contact-Wire Deflection

$$\underline{0} = -\text{diag} \left\{ \frac{EI}{\rho A} \bar{\beta}^{p4} + \frac{P}{\rho A} \bar{\beta}^{p2} \right\} \bar{\underline{p}} + \left(\text{sign}(\underline{s})^T .* \sin(\bar{\beta}^p \underline{x}_r^T) \right) \bar{\underline{\lambda}}_h \quad (2.76)$$

where $\bar{\underline{p}}$ is a column vector of \bar{p}_n -terms, $\bar{\underline{\beta}}^p$ a column vector of $\bar{\beta}_n^p$ -terms, \underline{s} a column vector of s_k -terms and $\bar{\underline{\lambda}}_h$ a column vector of $\bar{\lambda}_{h,k}$ -terms. ‘.’*’ has been used to denote the elementwise product of two vectors or matrices.

Dynamic, Horizontal Contact-Wire Deflection

$$\ddot{\underline{p}}(t) = -\text{diag} \left\{ \frac{EI}{\rho A} \beta^{p4} + \frac{P}{\rho A} \beta^{p2} \right\} \underline{p}(t) + \left(\text{sign}(\underline{s})^T .* \sin(\beta^p \underline{x}_r^T) \right) \underline{\lambda}_h(t) \quad (2.77)$$

where $\underline{p}(t)$ is a column vector of $p_n(t)$ -terms, $\underline{\beta}^p$ a column vector of β_n^p -terms and

$\underline{\lambda}_h(t)$ a column vector of $\lambda_{h,k}(t)$ -terms.

2.3.4 Messenger Supports

Above each registration arm, the messenger wire was supported by a spring and a damper. These supports are not included in Chapter 3, where the messenger wire is modelled as pinned-pinned, but are included in the subsequent chapters. The spring and damper forces update the boundary conditions for a free-free wire, as shown in (2.78)-(2.80). The tension term, $P\phi'$, has been omitted.

$$\phi_n^{m''}(0) = \phi_n^{m''}(L^m) = 0 \quad (2.78)$$

$$EI \sum_{n=1}^{\infty} \left(\phi_n^{m'''}(0) q_n^m(t) \right) = -\frac{k_1^s}{2} \sum_{n=1}^{\infty} (\phi_n^m(0) q_n^m(t)) - \frac{c_1^s}{2} \sum_{n=1}^{\infty} (\phi_n^m(0) \dot{q}_n^m(t)) \quad (2.79)$$

$$EI \sum_{n=1}^{\infty} \left(\phi_n^{m'''}(L^m) q_n^m(t) \right) = -\frac{k_2^s}{2} \sum_{n=1}^{\infty} (\phi_n^m(L^m) q_n^m(t)) - \frac{c_2^s}{2} \sum_{n=1}^{\infty} (\phi_n^m(L^m) \dot{q}_n^m(t)) \quad (2.80)$$

where k_1^s is the support spring constant at the start of the messenger span, c_1^s the support damping constant at the start of the messenger span, k_2^s is the support spring constant at the end of the messenger span and c_2^s the support damping constant at the end of the messenger span. The factor of two is due to the spring and damper forces being split between two adjacent messenger spans.

These boundary conditions were applied by choosing the $\phi_n^m(x)$ from (2.53) and making use of the integration by parts shown in (2.81), where the boundary conditions (2.79)-(2.80) were used to evaluate the term in square brackets.

$$\begin{aligned} \int_0^{L^m} \left(\phi_o^m(x) \phi_n^{m'''}(x) \right) dx &= \left[\phi_o^m(x) \phi_n^{m'''}(x) \right]_0^{L^m} \\ &\quad - \int_0^{L^m} \left(\phi_o^{m'}(x) \phi_n^{m'''}(x) \right) dx \end{aligned} \quad (2.81)$$

Substituting (2.81) into (2.63) and (2.70) yields (2.82) and (2.85), respectively. The analysis used for free-pinned and pinned-free messenger spans was analogous.

Steady-State, Vertical Messenger-Wire Deflection

$$\begin{aligned} 0 &= \left(E^m I^m \int_0^{L^m} \left(\phi_{i,n}^{m'''}(x) \phi_{i,n}^{m'}(x) \right) dx + P^m \int_0^{L^m} \left(\phi_{i,n}^{m''}(x) \phi_{i,n}^m(x) \right) dx \right) \bar{q}_{i,n}^m \\ &\quad + \sum_{j=1}^{N_d} \left(k_{d,i,j} \left(\sum_{n=1}^{\infty} (\bar{q}_{i,n} \phi_{i,n}(x_{d,i,j})) - \sum_{n=1}^{\infty} (\bar{q}_{i,n}^m \phi_{i,n}^m(x_{d,i,j}^m, t)) \right) \int_0^{L^m} \left(\phi_{i,n}^m(x) \delta(x - x_{d,i,j}^m) \right) dx \right) \\ &\quad - \frac{k_1^s}{2} \phi_{i,n}^m(0) \sum_{o=1}^{\infty} (\phi_{i,o}^m(0) \bar{q}_{i,o}^m) - \frac{k_2^s}{2} \phi_{i,n}^m(L^m) \sum_{o=1}^{\infty} (\phi_{i,o}^m(L^m) \bar{q}_{i,o}^m) - \rho^m A^m g \int_0^{L^m} \phi_{i,n}^m(x) dx \end{aligned} \quad (2.82)$$

$$\begin{aligned} \underline{0} &= \sum_{j=1}^{N_d} \left(k_{d,i,j} \underline{\phi}_i^m(x_{d,i,j}^m) \left(\sin(\bar{\beta} x_{d,i,j})^T \bar{q} - \underline{\phi}^{mT}(x_{d,i,j}^m) \bar{q}_i^m \right) \right) \\ &\quad + \left(E^m I^m \int_0^{L^m} \underline{\phi}_i^{m'''}(x) \underline{\phi}_i^{m'T}(x) dx + P^m \int_0^{L^m} \underline{\phi}_i^{m''}(x) \underline{\phi}_i^{mT}(x) dx \right. \\ &\quad \left. - \frac{k_1^s}{2} \underline{\phi}_i^m(0) \underline{\phi}_i^{mT}(0) - \frac{k_2^s}{2} \underline{\phi}_i^m(L^m) \underline{\phi}_i^{mT}(L^m) \right) \bar{q}_i^m - \rho^m A^m g \int_0^{L^m} \underline{\phi}_i^m(x) dx \end{aligned} \quad (2.83)$$

Using the orthogonality properties described in Section 2.3.3, it can be shown that the off-diagonal terms of each $\underline{\phi}_i^m(x) \underline{\phi}_i^{mT}(x)$ -matrix integrate to zero and (2.83) can be simplified to

$$\begin{aligned} \underline{0} &= \sum_{j=1}^{N_d} \left(k_{d,i,j} \underline{\phi}_i^m(x_{d,i,j}^m) \left(\sin(\bar{\beta} x_{d,i,j})^T \bar{q} - \underline{\phi}^{mT}(x_{d,i,j}^m) \bar{q}_i^m \right) \right) \\ &\quad + \left(E^m I^m \int_0^{L^m} \text{diag} \left\{ \underline{\phi}_i^{m'''}(x) \cdot^* \underline{\phi}_i^{m'}(x) \right\} dx + P^m \int_0^{L^m} \text{diag} \left\{ \underline{\phi}_i^{m''}(x) \cdot^* \underline{\phi}_i^m(x) \right\} dx \right. \\ &\quad \left. - \frac{k_1^s}{2} \underline{\phi}_i^m(0) \underline{\phi}_i^{mT}(0) - \frac{k_2^s}{2} \underline{\phi}_i^m(L^m) \underline{\phi}_i^{mT}(L^m) \right) \bar{q}_i^m - \rho^m A^m g \int_0^{L^m} \underline{\phi}_i^m(x) dx \end{aligned} \quad (2.84)$$

where $\text{diag} \left\{ \underline{\phi}_i^{m'''}(x) \cdot^* \underline{\phi}_i^{m'}(x) \right\}$ is a diagonal matrix with the elements of the column

vector $\underline{\phi}_i^{\text{m}'''}(x) \cdot^* \underline{\phi}_i^{\text{m}'}(x)$ along its leading diagonal.

Dynamic, Vertical Messenger-Wire Deflection

$$\begin{aligned}
\rho^{\text{m}} A^{\text{m}} \int_0^{L^{\text{m}}} \phi_{i,n}^{\text{m}2}(x) dx \quad \ddot{q}_{i,n}^{\text{m}}(t) = & \\
& \left(E^{\text{m}} I^{\text{m}} \int_0^{L^{\text{m}}} \left(\phi_{i,n}^{\text{m}'''}(x) \phi_{i,n}^{\text{m}'}(x) \right) dx + P^{\text{m}} \int_0^{L^{\text{m}}} \left(\phi_{i,n}^{\text{m}''}(x) \phi_{i,n}^{\text{m}}(x) \right) dx \right) \dot{q}_{i,n}^{\text{m}}(t) \\
& + \sum_{j=1}^{N_{\text{d}}} \left(k_{\text{d},i,j} \left(\sum_{n=1}^{\infty} (q_{i,n}^{\text{m}}(t) \phi_{i,n}(x_{\text{d},i,j})) - \sum_{n=1}^{\infty} (q_{i,n}^{\text{m}}(t) \phi_{i,n}^{\text{m}}(x_{\text{d},i,j}^{\text{m}}, t)) \right) \int_0^{L^{\text{m}}} (\phi_{i,n}^{\text{m}}(x) \delta(x - x_{\text{d},i,j}^{\text{m}})) dx \right) \\
& - \frac{c_1^{\text{s}}}{2} \phi_{i,n}^{\text{m}}(0) \sum_{o=1}^{\infty} (\phi_{i,o}^{\text{m}}(0) \dot{q}_{i,o}^{\text{m}}(t)) - \frac{c_2^{\text{s}}}{2} \phi_{i,n}^{\text{m}}(L^{\text{m}}) \sum_{o=1}^{\infty} (\phi_{i,o}^{\text{m}}(L^{\text{m}}) \dot{q}_{i,o}^{\text{m}}(t)) \\
& - \frac{k_1^{\text{s}}}{2} \phi_{i,n}^{\text{m}}(0) \sum_{o=1}^{\infty} (\phi_{i,o}^{\text{m}}(0) q_{i,o}^{\text{m}}(t)) - \frac{k_2^{\text{s}}}{2} \phi_{i,n}^{\text{m}}(L^{\text{m}}) \sum_{o=1}^{\infty} (\phi_{i,o}^{\text{m}}(L^{\text{m}}) q_{i,o}^{\text{m}}(t))
\end{aligned} \tag{2.85}$$

For the first and last messenger spans, spring and damper forces were only applied to the free end.

$$\begin{aligned}
\ddot{\underline{q}}_i^{\text{m}}(t) = & \left(\rho^{\text{m}} A^{\text{m}} \int_0^{L^{\text{m}}} \underline{\phi}_i^{\text{m}}(x) \underline{\phi}_i^{\text{mT}}(x) dx \right)^{-1} \left[\left(-\frac{c_1^{\text{s}}}{2} \underline{\phi}_i^{\text{m}}(0) \underline{\phi}_i^{\text{mT}}(0) - \frac{c_2^{\text{s}}}{2} \underline{\phi}_i^{\text{m}}(L^{\text{m}}) \underline{\phi}_i^{\text{mT}}(L^{\text{m}}) \right) \dot{\underline{q}}_i^{\text{m}}(t) \right. \\
& + \sum_{j=1}^{N_{\text{d}}} \left(k_{\text{d},i,j} \underline{\phi}_i^{\text{m}}(x_{\text{d},i,j}^{\text{m}}) \left(\sin(\beta x_{\text{d},i,j})^{\text{T}} \underline{q}(t) - \underline{\phi}_i^{\text{mT}}(x_{\text{d},i,j}^{\text{m}}) \underline{q}_i^{\text{m}}(t) \right) \right) \\
& + \left(E^{\text{m}} I^{\text{m}} \int_0^{L^{\text{m}}} \underline{\phi}_i^{\text{m}'''}(x) \underline{\phi}_i^{\text{m}'}(x) dx + P^{\text{m}} \int_0^{L^{\text{m}}} \underline{\phi}_i^{\text{m}''}(x) \underline{\phi}_i^{\text{mT}}(x) dx \right. \\
& \left. \left. - \frac{k_1^{\text{s}}}{2} \underline{\phi}_i^{\text{m}}(0) \underline{\phi}_i^{\text{mT}}(0) - \frac{k_2^{\text{s}}}{2} \underline{\phi}_i^{\text{m}}(L^{\text{m}}) \underline{\phi}_i^{\text{mT}}(L^{\text{m}}) \right) \underline{q}_i^{\text{m}}(t) \right]
\end{aligned} \tag{2.86}$$

Orthogonality can be used again, yielding

$$\begin{aligned}
\ddot{\underline{q}}_i^{\text{m}}(t) = & \left(\rho^{\text{m}} A^{\text{m}} \int_0^{L^{\text{m}}} \text{diag} \left\{ \underline{\phi}_i^{\text{m}2}(x) \right\} dx \right)^{-1} \left[\left(-\frac{c_1^{\text{s}}}{2} \underline{\phi}_i^{\text{m}}(0) \underline{\phi}_i^{\text{mT}}(0) - \frac{c_2^{\text{s}}}{2} \underline{\phi}_i^{\text{m}}(L^{\text{m}}) \underline{\phi}_i^{\text{mT}}(L^{\text{m}}) \right) \dot{\underline{q}}_i^{\text{m}}(t) \right. \\
& + \sum_{j=1}^{N_{\text{d}}} \left(k_{\text{d},i,j} \underline{\phi}_i^{\text{m}}(x_{\text{d},i,j}^{\text{m}}) \left(\sin(\beta x_{\text{d},i,j})^{\text{T}} \underline{q}(t) - \underline{\phi}_i^{\text{mT}}(x_{\text{d},i,j}^{\text{m}}) \underline{q}_i^{\text{m}}(t) \right) \right) \\
& + \left(E^{\text{m}} I^{\text{m}} \int_0^{L^{\text{m}}} \text{diag} \left\{ \underline{\phi}_i^{\text{m}'''}(x) \cdot^* \underline{\phi}_i^{\text{m}'}(x) \right\} dx + P^{\text{m}} \int_0^{L^{\text{m}}} \text{diag} \left\{ \underline{\phi}_i^{\text{m}''}(x) \cdot^* \underline{\phi}_i^{\text{m}}(x) \right\} dx \right. \\
& \left. \left. - \frac{k_1^{\text{s}}}{2} \underline{\phi}_i^{\text{m}}(0) \underline{\phi}_i^{\text{mT}}(0) - \frac{k_2^{\text{s}}}{2} \underline{\phi}_i^{\text{m}}(L^{\text{m}}) \underline{\phi}_i^{\text{mT}}(L^{\text{m}}) \right) \underline{q}_i^{\text{m}}(t) \right]
\end{aligned} \tag{2.87}$$

2.3.5 Registration-Arm Constraints and Rotations

Steady-State Vertical Constraint

$$\underline{0} = \underline{L}_r \cdot \sin \bar{\theta} - \sin \left(\bar{\beta} \underline{x}_r^T \right)^T \bar{q} \quad (2.88)$$

Steady-State Horizontal Constraint

$$\underline{0} = \underline{s} + \underline{L}_r \cdot \text{sign}(\underline{s}) \cdot (1 - \cos \bar{\theta}) - \sin \left(\bar{\beta}^p \underline{x}_r^T \right)^T \bar{p} \quad (2.89)$$

Dynamic Vertical Constraint

$$\underline{0} = \underline{L}_r \cdot \cos \bar{\theta} \cdot \underline{\theta}(t) - \sin \left(\underline{\beta} \underline{x}_r^T \right)^T \underline{q}(t) \quad (2.90)$$

Dynamic Horizontal Constraint

$$\underline{0} = \underline{L}_r \cdot \text{sign}(\underline{s}) \cdot \sin \bar{\theta} \cdot \underline{\theta}(t) - \sin \left(\underline{\beta}^p \underline{x}_r^T \right)^T \underline{p}(t) \quad (2.91)$$

Steady-State Registration-Arm Rotation

$$\underline{0} = -\underline{L}_r \cdot \bar{\lambda}_v \cdot \cos \bar{\theta} - \underline{L}_r \cdot \bar{\lambda}_h \cdot \sin \bar{\theta} - g \underline{m}_r \cdot \underline{L}_g \cdot \cos (\bar{\theta} - \underline{\alpha}) \quad (2.92)$$

Dynamic Registration-Arm Rotation

Two assumptions were made in order to simplify the dynamic registration-arm equations:

1. The dynamic rotation, $\underline{\theta}(t)$, is sufficiently small for the small-angle approximations to be used.
2. The dynamic terms $\underline{\lambda}_h(t)$, $\underline{\lambda}_v(t)$ and $\underline{\theta}(t)$ are very small relative to the steady-state terms, so the product of any two dynamic terms is negligible.

$$\begin{aligned} J \ddot{\underline{\theta}}(t) = & \left(\underline{L}_r \cdot \bar{\lambda}_v \cdot \sin \bar{\theta} - \bar{\lambda}_h \cdot \underline{L}_r \cdot \cos \bar{\theta} + g \underline{m}_r \cdot \underline{L}_g \cdot \sin (\bar{\theta} - \underline{\alpha}) \right) \cdot \underline{\theta}(t) \\ & - \underline{L}_r \cdot \sin \bar{\theta} \cdot \underline{\lambda}_h(t) - \underline{L}_r \cdot \cos \bar{\theta} \cdot \underline{\lambda}_v(t) \end{aligned} \quad (2.93)$$

Elimination of Constraints and Forces

The dynamic registration-arm constraints, (2.90)-(2.91), were used to find $\underline{\theta}(t)$ and $\underline{p}(1 : N_r)(t)$ as linear, time-invariant functions of $\underline{q}(t)$ and $\underline{p}(N_r + 1 : \text{end})(t)$. These equations were removed and the expressions for $\underline{\theta}(t)$ and $\underline{p}(1 : N_r)(t)$ substituted into each equation in which the terms appeared. Similarly, (2.93) was used to eliminate $\underline{\lambda}_v(t)$ and (2.77) was used to eliminate $\underline{\lambda}_h(t)$. These terms were reconstructed in post-processing using the eliminated equations.

2.3.6 The Vertical Pantograph Constraints

The pantograph contact constraints were used to reflect the condition that the pantograph head remains in contact with the contact wire. The position constraint ensured that the height of the pantograph head matched the contact-wire deflection at that position and the first two time derivatives of this constraint were also used.

Position Constraint

$$\begin{aligned} 0 &= z_1(t) + \bar{z}_1 - \underline{\phi}^T(x_p(t))\underline{q}(t) - \underline{\phi}^T(x_p(t))\bar{\underline{q}} \\ &= z_1(t) + \bar{z}_1 - \sin(\underline{\beta}x_p(t))^T \underline{q}(t) - \sin(\bar{\underline{\beta}}x_p(t))^T \bar{\underline{q}} \end{aligned} \quad (2.94)$$

Velocity Constraint

$$\begin{aligned} 0 &= \dot{z}_1(t) - \sin(\underline{\beta}x_p(t))^T \dot{\underline{q}}(t) \\ &\quad - ((\underline{\beta}v_p(t))^T \cos(\underline{\beta}x_p(t)))^T \underline{q}(t) - ((\bar{\underline{\beta}}v_p(t))^T \cos(\bar{\underline{\beta}}x_p(t)))^T \bar{\underline{q}} \end{aligned} \quad (2.95)$$

It should be noted that, while $\underline{\phi}(x)$ is independent of time, $\underline{\phi}(x_p(t))$ is a function of $x_p(t)$ and therefore a function of time.

Acceleration Constraint

$$\begin{aligned} 0 &= \ddot{z}_1(t) - \sin(\underline{\beta}x_p(t))^T \ddot{\underline{q}}(t) - ((\underline{\beta}v_p(t))^T \cos(\underline{\beta}x_p(t)))^T \dot{\underline{q}}(t) \\ &\quad + \left(((\underline{\beta}v_p(t))^2 \sin(\underline{\beta}x_p(t))) - ((\underline{\beta}a_p(t))^T \cos(\underline{\beta}x_p(t)))^T \right) \underline{q}(t) \\ &\quad + \left(((\bar{\underline{\beta}}v_p(t))^2 \sin(\bar{\underline{\beta}}x_p(t))) - ((\bar{\underline{\beta}}a_p(t))^T \cos(\bar{\underline{\beta}}x_p(t)))^T \right) \bar{\underline{q}} \end{aligned} \quad (2.96)$$

2.3.7 Modal Index-Three DAE

All of the dynamic OLE equations are compiled in (2.99). The states are functions of time, but not of space, meaning that the DAE can be solved by integration. While the numerical solution of high-index DAEs is nontrivial, this linear, time-varying DAE is much easier to solve than many nonlinear DAEs.

$$\ddot{\underline{q}}(t) = A_1 \hat{q}(t) + A_2 \dot{\underline{q}}(t) + A_3 \ddot{\underline{q}}(t) + \frac{2 \sin \left(\tilde{\underline{\beta}} x_p(t) \right)}{\rho AL} \lambda(t) \quad (2.97)$$

$$\ddot{\underline{q}}(t) = (I - A_3)^{-1} \left(A_1 \hat{q}(t) + A_2 \dot{\underline{q}}(t) + \frac{2 \sin \left(\tilde{\underline{\beta}} x_p(t) \right)}{\rho AL} \lambda(t) \right) \quad (2.98)$$

$$\begin{aligned} \ddot{\underline{q}}(t) &= A_1 \hat{q}(t) + A_2 \dot{\underline{q}}(t) + A_3 \ddot{\underline{q}}(t) + \hat{f}(t) \lambda(t) \\ \ddot{z}_1(t) &= -\frac{c_1}{m_1} \dot{z}_1(t) + \frac{c_1}{m_1} \dot{z}_2(t) - \frac{k_1}{m_1} z_1(t) + \frac{k_1}{m_1} z_2(t) - \frac{1}{m_1} \lambda(t) \\ 0 &= z_1(t) + \bar{z}_1 - \sin \left(\tilde{\underline{\beta}} x_p(t) \right)^T \hat{q}(t) - \sin \left(\bar{\underline{\beta}} x_p(t) \right)^T \bar{q} \end{aligned} \quad (2.99)$$

where

$$\hat{q}(t) = \begin{pmatrix} \underline{q}(t) \\ p(N_r + 1 : \text{end})(t) \\ q_1^m(t) \\ q_2^m(t) \\ \vdots \\ q_{N_m}^m(t) \end{pmatrix} \quad (2.100)$$

$$\underline{u}(t) = \begin{pmatrix} \hat{q}(t) \\ z_1(t) \end{pmatrix} \quad (2.101)$$

$$\tilde{\underline{\beta}} = \begin{pmatrix} \underline{\beta} \\ \underline{0} \end{pmatrix} \quad (2.102)$$

$$\underline{\hat{f}}(t) = \frac{2 \sin \left(\tilde{\beta} x_p(t) \right)}{\rho AL} \quad (2.103)$$

where $z_2(t)$ was calculated separately, because (2.2) contains no $\lambda(t)$ -, $\underline{p}(t)$ - or $\underline{q}(t)$ -terms. For a three-mass pantograph model, $z_3(t)$ was included in the state vector, $\underline{\hat{u}}(t) = \begin{pmatrix} \underline{\hat{q}}(t) \\ z_3(t) \end{pmatrix}$, while $\begin{pmatrix} z_1(t) \\ z_2(t) \end{pmatrix}$ was calculated separately.

A_1 , A_2 and A_3 in (2.99) are matrices comprised of the dynamic terms from (2.71), (2.77), and (2.87). A_2 contains only the damping terms due to the messenger-wire damper supports. If the messenger wire is modelled with fixed supports and pinned-pinned boundary conditions, A_2 is empty. A_3 contains only the acceleration terms that appear in the right-hand sides of the equations of motion due to the elimination of the registration-arm forces and rotations.

2.3.8 The Structure of A_1

The structure of A_1 is illustrated in Figure 2.5. The white blocks represent empty matrices, whereas the numbered blocks represent full matrices. The matrices on the leading diagonal are square and the off-diagonal matrices are generally nonsquare, because of the different number of vertical, horizontal and messenger-wire modes included.

1	4	6	6	6	6	6	6
5	2						
7		3					
7			3				
7				3			
7					3		
7						3	
7							3

Figure 2.5: Diagram of structure of A_1

Each number represents a different set of terms from the overhead wires' equations of motion. While two '3' matrices may differ in size and value, all '3's come from the same terms in the dynamic messenger-wire equation.

- 1: The bending-stiffness, tension and self-dependent dropper terms in (2.71).
- 2: The bending-stiffness and tension terms in (2.77).
- 3: The bending-stiffness, tension and self-dependent dropper terms in (2.87), as well as the terms due to the spring support.
- 4: The $\underline{p}(N_r + 1 : end)(t)$ -terms brought into (2.71) as a result of eliminating $\underline{\lambda}_v(t)$.
- 5: The $\underline{q}(t)$ -terms brought into (2.77) as a result of eliminating $\underline{\lambda}_h(t)$.
- 6: The interdependent dropper terms in (2.71).
- 7: The interdependent dropper terms in (2.87).

2.3.9 Eigenvector Decomposition

The A_1 -matrix was decomposed into its eigenvectors and eigenvalues. Both sides of the $\hat{\underline{q}}(t)$ -equation in (2.99) were premultiplied by the right eigenvector matrix, W , leading to a diagonalised DAE, (2.107). The system is well conditioned, because the dominant terms in A_1 are the tension and bending-stiffness terms on the leading diagonal. These terms are much larger than the off-diagonal terms. Therefore, diagonalisation is appropriate here.

$$A_1 = V \Lambda W \quad (2.104)$$

$$V = W^{-1} \quad (2.105)$$

Let $\tilde{\underline{q}}(t) = W \hat{\underline{q}}(t)$.

$$\ddot{\underline{q}}(t) = W \ddot{\hat{\underline{q}}}(t) = W A_1 \hat{\underline{q}}(t) + W A_2 \dot{\hat{\underline{q}}}(t) + W \underline{\hat{f}}(t) \lambda(t) \quad (2.106)$$

$$\ddot{\underline{\tilde{q}}}(t) = \Lambda \underline{\tilde{q}}(t) + W A_2 V \dot{\underline{\tilde{q}}}(t) + \underline{\tilde{f}}(t) \lambda(t) \quad (2.107)$$

2.3.10 Modal Damping

Wire damping was added to the catenary model after diagonalisation [35]. This damping applied to both the contact wire and messenger wire and was separate from the spring-damper supports in Section 2.3.4. The damping matrix, η , was evaluated by considering the unforced dynamics of $\underline{\tilde{q}}(t)$, neglecting A_2 , which was found to be extremely small relative to A_1 .

$$\underline{\tilde{q}}_{\text{unforced}}(t) = A_0 e^{j\Omega_0 t}, \quad (2.108)$$

where Ω_0 is a diagonal matrix.

$$\ddot{\underline{\tilde{q}}}_{\text{unforced}}(t) = -A_0 \Omega_0^2 e^{j\Omega_0 t} = A_0 \Lambda e^{j\Omega_0 t} \quad (2.109)$$

$$\Omega_0 = (-\Lambda)^{\frac{1}{2}} \quad (2.110)$$

$$\eta = 2\zeta \Omega_0 \quad (2.111)$$

$$\ddot{\underline{\tilde{q}}}(t) = \Lambda \underline{\tilde{q}}(t) + B \dot{\underline{\tilde{q}}}(t) + \underline{\tilde{f}}(t) \lambda(t) \quad (2.112)$$

$$B = W A_2 V - \eta \quad (2.113)$$

where η is a square matrix with dimensions equal to the number of ODE states.

2.3.11 Model Order Reduction

The modes were sorted into descending-eigenvalue order and the roll-off is shown in Figure 2.6. The modes and equations corresponding to eigenvalues that were more negative than a threshold value, Λ_{\min} , were removed. The choice of Λ_{\min} is discussed in Section 2.3.15.

$$\tilde{V} = V(:, 1 : N_{\text{modes}}) \quad (2.114)$$

$$\tilde{\Lambda} = \Lambda(1 : N_{\text{modes}}, 1 : N_{\text{modes}}) \quad (2.115)$$

$$\tilde{W} = W(1 : N_{\text{modes}}, :) \quad (2.116)$$

$$\tilde{B} = B(1 : N_{\text{modes}}, 1 : N_{\text{modes}}) \quad (2.117)$$

$$\ddot{\underline{q}}(t) = \tilde{\Lambda} \underline{\tilde{q}}(t) + \tilde{B} \dot{\underline{\tilde{q}}}(t) + \underline{\tilde{f}}(t) \lambda(t), \quad (2.118)$$

where $\ddot{\underline{q}}(t)$ and $\underline{\tilde{f}}(t)$ have been truncated to the corresponding dimensions.

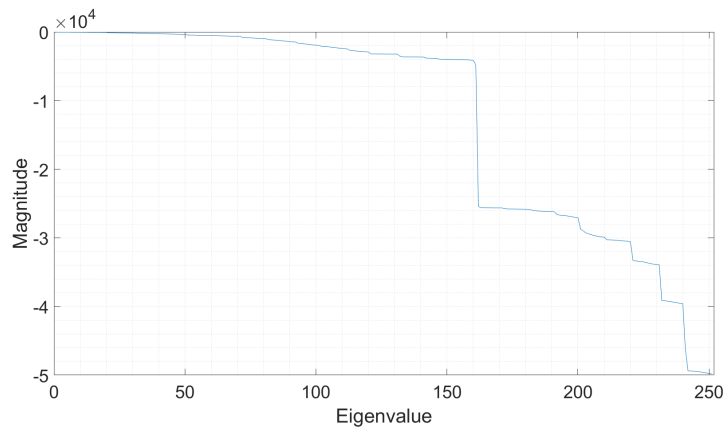


Figure 2.6: Plot of eigenvalue roll-off for BS:EN 50318:2002

2.3.12 Possible Methods of DAE Solution

Four methods of DAE solution were tested and the most suitable one chosen. The results of each method were compared to the other methods' results to verify its realism. The simulation speeds were also compared.

GGL Formulation

The GGL formulation, detailed in [27, 28], was tested on a simplified catenary system. Both the position constraint and the velocity constraint were applied using a fictitious force, $\underline{\mu}$, as shown in (2.119). This reduced the intractable index-three DAE to a solvable index-two DAE.

$$\begin{aligned}
 \dot{\underline{p}} &= \underline{v} - G^T(\underline{p}) \underline{\mu} \\
 M(\underline{p}) \dot{\underline{v}} &= \underline{f}(\underline{p}, \underline{v}, t) - G^T(\underline{p}) \underline{\lambda} \\
 \underline{0} &= \underline{g}(\underline{p}) \\
 \underline{0} &= G(\underline{p}) \underline{v}
 \end{aligned} \tag{2.119}$$

The third equation is the position constraint and the fourth is the velocity constraint. The fictitious force, $\underline{\mu}(t)$, which is numerically close to zero, allows the otherwise-overdetermined DAE to be solved.

This method was implemented in MATLAB, producing results in agreement with the other working methods' results. However, the simulation speed was relatively slow, because an index-two DAE takes more computational effort to solve than an ODE.

Index-One DAE

The index-three DAE was reduced to index one by differentiation. The acceleration constraint, (2.96), was applied in place of the position constraint.

This method produced realistic results for short simulations. However, even the index-one DAE was slower to solve than an ODE. Furthermore, the lack of a position constraint

meant that the pantograph head and wire deflection gradually drifted apart due to small errors in the acceleration constraint. This drift could be handled by correcting the position constraint at regular time intervals, but this would reduce the simulation speed.

Contact Spring

One alternative method that is suggested by the 2002 European Standard is the use of a fictional contact spring: the contact constraint is removed and a stiff spring connects the pantograph head to the contact wire. The European Standard suggests a spring constant of 50kNm^{-1} .

This method gave excellent simulation speed, as there was no algebraic constraint and the system of equations was therefore an ODE. However, any small errors in the contact constraint were amplified by the spring constant, leading to large errors in the contact force.

The spring constant could not be significantly reduced, because it would then be comparable to the spring constants in the mass-spring-damper pantograph model and would give erroneous results. The spring constant was made arbitrarily large in order to force the contact constraint to be satisfied, but the solver could not solve the ODE. Therefore, this method was discarded.

Elimination of Variables

The algebraic constraint was removed by elimination of variables, reducing the index-three DAE to a solvable ODE. The contact constraints, (2.94)-(2.96), were used to find expressions for $\tilde{q}_1(t)$, $\dot{\tilde{q}}_1(t)$ and $\ddot{\tilde{q}}_1(t)$ in terms of the remaining states, then (2.118) was rearranged to find an expression for $\lambda(t)$. This analytical elimination was possible because the DAE system is linear; for a nonlinear DAE, the algebraic elimination would have to be performed at each time step.

$$\tilde{V}_1 = \tilde{V}(:, 1) \quad (2.120)$$

$$\tilde{V}_2 = \tilde{V}(:, 2 : \text{end}) \quad (2.121)$$

Position Constraint

$$0 = z_1(t) + \bar{z}_1 - \sin \left(\underline{\tilde{\beta}x_p}(t) \right)^T \left(\tilde{V}_1 \tilde{q}_1(t) + \tilde{V}_2 \tilde{q}_2(t) \right) - \sin \left(\underline{\bar{\beta}x_p}(t) \right)^T \underline{\bar{q}} \quad (2.122)$$

$$\tilde{q}_1(t) = \frac{1}{\sin \left(\underline{\tilde{\beta}x_p}(t) \right)^T \tilde{V}_1} \left(z_1(t) + \bar{z}_1 - \sin \left(\underline{\tilde{\beta}x_p}(t) \right)^T \tilde{V}_2 \tilde{q}_2(t) - \sin \left(\underline{\bar{\beta}x_p}(t) \right)^T \underline{\bar{q}} \right) \quad (2.123)$$

Velocity Constraint

$$\begin{aligned} 0 = & \dot{z}_3(t) - \sin \left(\underline{\tilde{\beta}x_p}(t) \right)^T \left(\tilde{V}_1 \dot{\tilde{q}}_1(t) + \tilde{V}_2 \dot{\tilde{q}}_2(t) \right) \\ & - \left(\left(\underline{\tilde{\beta}x_p}(t) \right)^* \cos \left(\underline{\tilde{\beta}x_p}(t) \right) \right)^T \left(\tilde{V}_1 \tilde{q}_1(t) + \tilde{V}_2 \tilde{q}_2(t) \right) \\ & - \left(\left(\underline{\bar{\beta}x_p}(t) \right)^* \cos \left(\underline{\bar{\beta}x_p}(t) \right) \right)^T \underline{\bar{q}} \end{aligned} \quad (2.124)$$

$$\begin{aligned} \dot{\tilde{q}}_1(t) = & \frac{1}{\sin \left(\underline{\tilde{\beta}x_p}(t) \right)^T \tilde{V}_1} \left(\dot{z}_3(t) - \sin \left(\underline{\tilde{\beta}x_p}(t) \right)^T \tilde{V}_2 \dot{\tilde{q}}_2(t) \right. \\ & \left. - \left(\left(\underline{\bar{\beta}x_p}(t) \right)^* \cos \left(\underline{\bar{\beta}x_p}(t) \right) \right)^T \underline{\bar{q}} \right. \\ & \left. - \left(\left(\underline{\tilde{\beta}x_p}(t) \right)^* \cos \left(\underline{\tilde{\beta}x_p}(t) \right) \right)^T \left(\tilde{V}_1 \tilde{q}_1(t) + \tilde{V}_2 \tilde{q}_2(t) \right) \right) \end{aligned} \quad (2.125)$$

Acceleration Constraint

$$\begin{aligned} 0 = & \ddot{z}_3(t) + \left(\left(\left(\underline{\tilde{\beta}v_p}(t) \right)^2 \right)^* \sin \left(\underline{\tilde{\beta}x_p}(t) \right) \right) - \left(\left(\underline{\tilde{\beta}a_p}(t) \right)^* \cos \left(\underline{\tilde{\beta}x_p}(t) \right) \right)^T \underline{\bar{q}} \\ & - \sin \left(\underline{\tilde{\beta}x_p}(t) \right)^T \left(\tilde{V}_1 \ddot{\tilde{q}}_1(t) + \tilde{V}_2 \ddot{\tilde{q}}_2(t) \right) - \left(\left(\underline{\tilde{\beta}v_p}(t) \right)^* \cos \left(\underline{\tilde{\beta}x_p}(t) \right) \right)^T \left(\tilde{V}_1 \dot{\tilde{q}}_1(t) + \tilde{V}_2 \dot{\tilde{q}}_2(t) \right) \\ & + \left(\left(\left(\underline{\tilde{\beta}v_p}(t) \right)^2 \right)^* \sin \left(\underline{\tilde{\beta}x_p}(t) \right) \right) - \left(\left(\underline{\tilde{\beta}a_p}(t) \right)^* \cos \left(\underline{\tilde{\beta}x_p}(t) \right) \right)^T \left(\tilde{V}_1 \tilde{q}_1(t) + \tilde{V}_2 \tilde{q}_2(t) \right) \end{aligned} \quad (2.126)$$

$$\begin{aligned}
\ddot{\tilde{q}}_1(t) = & \frac{1}{\sin(\tilde{\beta}x_p(t))^T \tilde{V}_1} \left(\ddot{z}_3(t) \right. \\
& - \sin(\tilde{\beta}x_p(t))^T \tilde{V}_2 \ddot{\tilde{q}}_2(t) - \left((\tilde{\beta}v_p(t)) \cdot \cos(\tilde{\beta}x_p(t)) \right)^T (\tilde{V}_1 \dot{\tilde{q}}_1(t) + \tilde{V}_2 \dot{\tilde{q}}_2(t)) \\
& + \left(\left((\tilde{\beta}v_p(t))^2 \cdot \sin(\tilde{\beta}x_p(t)) \right) - \left((\tilde{\beta}a_p(t)) \cdot \cos(\tilde{\beta}x_p(t)) \right) \right)^T (\tilde{V}_1 \tilde{q}_1(t) + \tilde{V}_2 \tilde{q}_2(t)) \\
& + \left(\left((\tilde{\beta}v_p(t))^2 \cdot \sin(\tilde{\beta}x_p(t)) \right) - \left((\tilde{\beta}a_p(t)) \cdot \cos(\tilde{\beta}x_p(t)) \right) \right)^T \underline{\tilde{q}}(t) \Big) \quad (2.127)
\end{aligned}$$

Elimination of λ

$$\ddot{\tilde{q}}_1(t) = \tilde{\Lambda}(1, 1)\tilde{q}_1(t) + \tilde{B}(1, 1)\dot{\tilde{q}}_1(t) + \tilde{B}(1, 2 : \text{end})\dot{\tilde{q}}_2(t) + \underline{\tilde{f}}(1)(t)\lambda(t), \quad (2.128)$$

$$\lambda(t) = \frac{1}{\underline{\tilde{f}}(1)(t)} \left(\ddot{\tilde{q}}_1(t) - \tilde{\Lambda}(1, 1)\tilde{q}_1(t) - \tilde{B}(1, 1)\dot{\tilde{q}}_1(t) - \tilde{B}(1, 2 : \text{end})\dot{\tilde{q}}_2(t) \right), \quad (2.129)$$

Elimination of variables produced realistic results and provided excellent simulation speed, as the linear DAE was reduced to a linear ODE. The algebraic elimination only had to be performed once, producing expressions for the eliminated terms as functions of the remaining states and of time.

Reasons for Choosing Elimination of Variables

In Section 1.2.6, it was noted that using the GGL formulation was the consensus best method of numerically solving DAEs [27]. However, the literature primarily considers nonlinear DAEs, whereas the equation considered here is a linear, time-varying DAE. For a nonlinear DAE, the algebraic elimination would have to be performed at each time step, greatly reducing the simulation speed. Therefore, elimination of variables is relatively straightforward for pantograph-catenary modelling and the valid reason for dismissing elimination for nonlinear DAEs does not apply here.

Of all of the solution methods that were tested, elimination of variables provided the fastest simulation speed while exhibiting no problems in terms of realism and robustness.

Furthermore, elimination generalises easily to multiple pantographs and contact wires, which will be demonstrated in Chapter 4 and Chapter 5.

2.3.13 Reconstruction

$\tilde{q}_1(t)$ and its time derivatives were reconstructed at each time step from the expressions derived in Section 2.3.12, as was $\lambda(t)$. After the ODE had been solved by integration, the eigenvector decomposition was reversed and $\underline{p}(1 : N_r)(t)$ was reconstructed in post-processing in order to plot the results. $\underline{\theta}(t)$ was not used, but it could easily be reconstructed from the registration-arm constraints if necessary.

2.3.14 Overview of Solution Process

1. Decompose each wire deflection into an infinite series of spatial basis functions and corresponding time functions.
2. Use the wire's boundary conditions to evaluate its spatial basis functions.
3. Use orthogonality integrals to reduce the PDEs in $w(x, t)$ to ODEs in $q(t)$. Together with the pantograph contact constraint, this yields an index-three DAE.
4. Truncate this infinite series of basis functions and time functions to match the frequency response of the pantograph.
5. Eliminate $\underline{p}(1 : N_r)(t)$ and $\underline{\theta}(t)$ using the linear, time-invariant registration-arm constraints.
6. Use eigenvector decomposition to diagonalise the DAE.
7. Truncate $\tilde{q}(t)$ to remove any eigenmodes which correspond to eigenvalues below a certain cut-off value.
8. Eliminate $\tilde{q}_1(t)$, $\dot{\tilde{q}}_1(t)$ and $\ddot{\tilde{q}}_1(t)$ using the position constraint and its first two time derivatives.
9. Use the $\tilde{q}(t)$ -equation to eliminate $\lambda(t)$.

10. Solve the resulting ODE by integration.
11. Reconstruct $\lambda(t)$ using the previously derived expression.
12. Reconstruct $\tilde{q}_1(t)$ and its time derivatives.
13. Reverse the eigenvector decomposition to recover to the original DAE states, $\hat{q}(t)$.
14. Reconstruct $\underline{p}(1 : N_r)(t)$.
15. Combine $\underline{\phi}(x)$ and $\underline{q}(t)$ (or $\underline{p}(t)$) for each wire to find the wire deflections, $w(x, t)$.
16. Analyse the contact force, wire deflections and pantograph motion.

It can be seen that after integration, the process used to form the ODE is reversed in order to recover the original wire deflections. This solution process was chosen in order to simplify the numerical integration as much as possible, as that is where most of the time is spent.

2.3.15 Choice of Numbers of Modes

Numbers of Steady-State Modes

The speed of steady-state modelling is less important, because the steady-state deflections are only calculated once per catenary system and the same catenary system may be used for hundreds of dynamic tests. Therefore, it was not necessary to calculate precisely the optimal number of steady-state terms to include, so long as enough modes were used. $N_{\tilde{q}}$, $N_{\tilde{p}}$ and $N_{\tilde{q}}^m$ were increased until the wire displacement corresponding to the last term was sufficiently small.

This was done imprecisely, with the aim of the final term contributing no more than a 1mm displacement for any x . For comparison, the maximum steady-state vertical deflection of the contact wire for the 2002 European Standard was 11mm. The maximum horizontal stagger of the contact wire and the maximum vertical deflection of the messenger wire were each more than one order of magnitude larger than 11mm.

Numbers of Dynamic Modes Before Diagonalisation

FEM software typically filters out any catenary vibrations at frequencies above 20Hz during the simulation. The Galerkin software presented in this thesis differs by filtering out high-frequency catenary modes by truncating the series of $q_n(t)$ -, $p_n(t)$ - and $q_n^m(t)$ -terms to match the pantograph dynamics.

The frequency analysis was performed by simulating a sinusoidal contact force acting on the pantograph head and measuring the frequency response of the pantograph head. This methodology was chosen because the motion of the pantograph head and overhead wires is an important part of this pantograph-catenary simulation, whereas the precise motion of the lower segments of the pantograph is not important.

Each wire shape corresponds to a frequency of vibration of the pantograph head. A plot of the magnitude of the frequency response of the pantograph head was used to determine the maximum frequency of vibration of the pantograph head, which was used to calculate the number of wire shapes required.

A sinusoidal contact force was applied to the pantograph head and the resulting sinusoidal motion of the pantograph head was evaluated using (2.1)-(2.2).

$$\lambda(t) = \Lambda_0 e^{j\omega t} \quad (2.130)$$

$$z_1(t) = X_1 e^{j(\omega t + \psi_1)} \quad (2.131)$$

$$z_2(t) = X_2 e^{j(\omega t + \psi_2)} \quad (2.132)$$

$$M_z \begin{pmatrix} X_1 e^{j\psi_1} \\ X_2 e^{j\psi_2} \end{pmatrix} e^{j\omega t} = \begin{pmatrix} \Lambda_0 e^{j\omega t} \\ P_2 \end{pmatrix} \quad (2.133)$$

$$M_z = \begin{pmatrix} -\omega^2 m_1 + j\omega c_1 + k_1 & -j\omega c_1 - k_1 \\ -j\omega c_1 - k_1 & -\omega^2 m_2 + j\omega(c_1 + c_2) + k_1 + k_2 \end{pmatrix} \quad (2.134)$$

$$\left\| \frac{Z_1(j\omega)}{\Lambda(j\omega)} \right\|_2 = \begin{pmatrix} 1 & 0 \end{pmatrix} M_z^{-1} \begin{pmatrix} -1 \\ 0 \end{pmatrix} \quad (2.135)$$

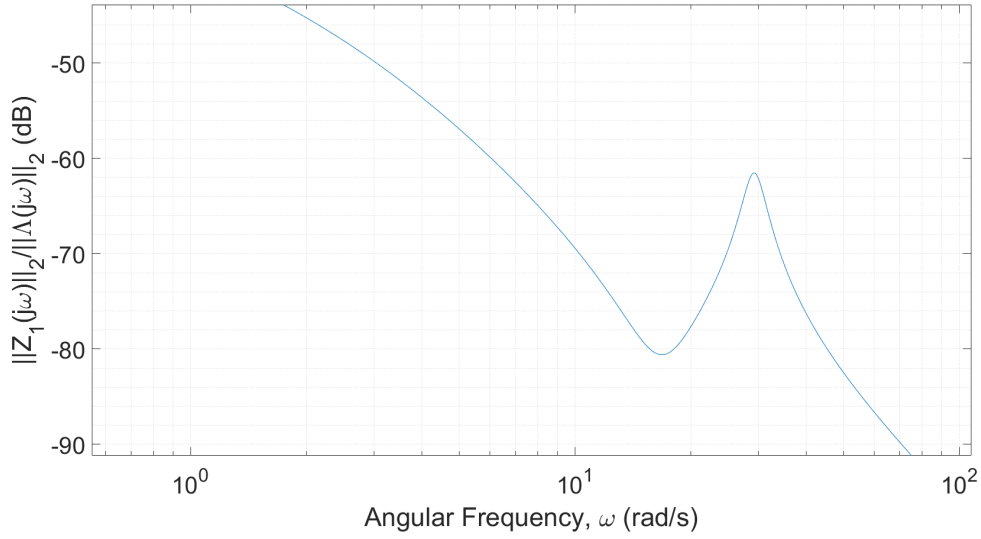


Figure 2.7: Plot of frequency response of pantograph head excited by sinusoidal contact force with angular frequency ω

A cut-off attenuation was chosen by analysing the eigenvalue roll-off and (2.135) was used to find ω_0 , the minimum ω -value to achieve the desired attenuation. The unforced vibration of each wire was then analysed to determine the number of modes included for that wire.

$$\underline{q}_n = Q_{0,n} e^{j\omega t} \quad (2.136)$$

$$-\omega^2 Q_{0,n} e^{j\omega t} = - \left(\frac{EI}{\rho A} \left(\frac{n\pi}{L} \right)^4 + \frac{P}{\rho A} \left(\frac{n\pi}{L} \right)^2 \right) Q_{0,n} e^{j\omega t} \quad (2.137)$$

$$\omega_0^2 \leq \left(\frac{EI}{\rho A} \left(\frac{N_q \pi}{L} \right)^4 + \frac{P}{\rho A} \left(\frac{N_q \pi}{L} \right)^2 \right) \quad (2.138)$$

The number of contact-wire modes, N_q and N_p , was chosen to be the smallest integer that satisfied (2.138). A typical value of ω_0 is 72rad/s or 11.5Hz. The same technique and the same ω_0 were used to calculate N_q^m .

Number of Eigenmodes After Diagonalisation

After eigenvector decomposition, the number of eigenmodes included in the model was determined using a maximum eigenvalue magnitude. Any eigenmodes corresponding to eigenvalues more negative than this value were ignored.

This differs from the previous truncation of the original states, in which the spatial frequencies of individual-wire terms were limited to match the pantograph dynamics. The purpose of the previous truncation was to disallow pantograph-catenary motion corresponding to unrealistically high pantograph-head oscillation frequencies. The purpose of this final truncation is to expedite the numerical integration of the ODE by removing any eigenmodes that have a negligible effect on the wire deflections.

2.4 Conclusions

The mathematical model for each part of the pantograph-catenary system has been described. These models have been chosen in order to maximise simulation speed while producing realistic results. The pantograph is modelled as a mass-spring-damper system with two or three masses, while the overhead wires are modelled as Euler-Bernoulli beams.

The advantages and limitations of the chosen methods have been discussed. Choices for numbers of modes and the decision to neglect parameters such as dropper mass have been explained and have been supported by numerical comparisons.

Chapter 3

Validation Against BS:EN 50318:2002

3.1 Introduction

In this chapter, the process of validating the model against the 2002 European Standard [34] is detailed. A single two-mass pantograph is modelled in contact with a single contact wire for trains travelling at constant speeds of 250 km/hour and 300 km/hour. Dropper unloading is not included.

The European Standard gives acceptable ranges for various properties of the contact force, $\lambda(t)$, as well as for the maximum contact-wire uplift at a registration arm, underneath a messenger support. It is desirable to obtain realistic results with the greatest possible simulation speed.

The results of the Simulink model are shown and compared to those required by the BSI. Conclusions are drawn about the realistic and speed of the simulation.

3.2 Specification

This chapter covers the first in a series of increasingly complicated analyses as the realism of the modelled overhead system is increased. Therefore, this first system is the simplest realistic case.

The design and parameters of the overhead system were prescribed by the European Standard. They were chosen to represent a simple-but-realistic overhead system, with

a standard design and no discrete components. Discrete components, such as section insulators, are an important part of the design of real overhead catenary systems, but are difficult to model, because they change the topology of the OLE system.

The most important, fundamental components of an OLE system are all included: the pantograph, contact wire, messenger wire and droppers. This European Standard is used as an initial check that a new piece of pantograph-catenary simulation software produces realistic results and later validations are used to test the software's ability to handle complex and varied overhead systems.

3.2.1 The Pantograph

The prescribed two-mass pantograph model, as shown in Figure 2.1a, was used and the constants are shown in Table 3.1.

Parameter	m_1	m_2	c_1	c_2	k_1	k_2	P_2
Value	7.2kg	15kg	10Nsm ⁻¹	90Nsm ⁻¹	4200Nm ⁻¹	50Nm ⁻¹	120N

Table 3.1: Table of pantograph constants for validation against BS:EN 50318:2002

3.2.2 The Catenary System

The overhead catenary system is illustrated in Figure 3.1. The contact wire is 600m in length and the messenger wire is split into ten 60m spans. There are nine droppers per messenger span and nine total registration arms, which are placed at the ends of the messenger spans.

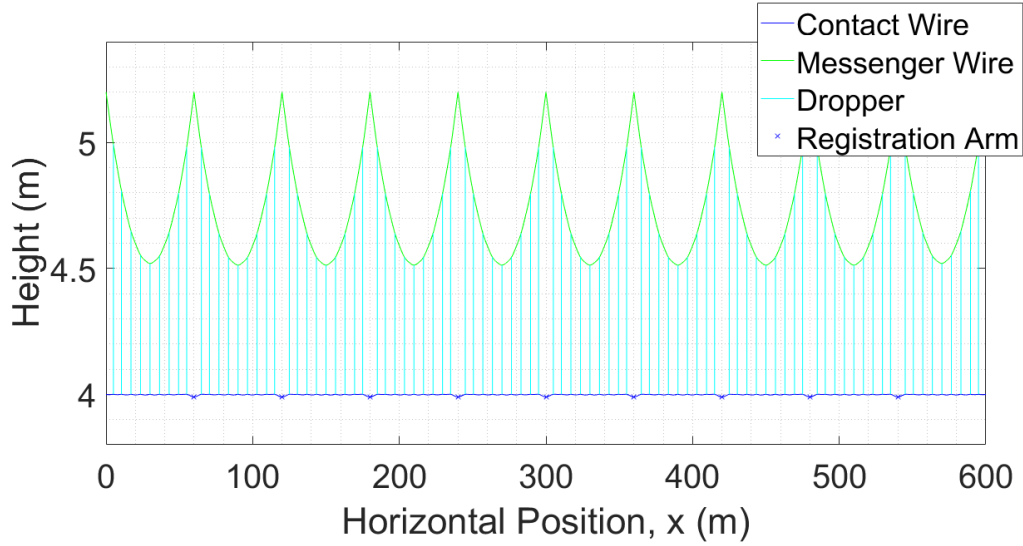


Figure 3.1: Plot of steady-state vertical wire deflections for BS:EN 50318:2002

3.2.3 Quality of Validation

This thesis compares the results of the analysis to values expected in the ruling European Standards. This is a weaker form of validation than direct comparison to real line-test data or to an existing, validated model. However, it is standard for new pantograph-catenary software to be validated in this manner, as the standardised OLE set-up allows a like-for-like comparison of simulation results.

There is also potential for overfitting: there are many degrees of freedom in the parameters of the model, such as the number of terms included at each stage and the ODE-solver settings. It is possible that even faulty or unrealistic software could yield satisfactory results using contrived parameters. To mitigate this problem, all of the parameters were set to reasonable values before comparing the results against the benchmark. Once preliminary results had been obtained, only small changes were made to the model's parameters, such as increasing the damping factor of the overhead system.

3.2.4 Numbers of Modes Used

The pantograph frequency analysis outlined in Section 2.3.15 was used, with a minimum attenuation of 90dB. This gave a frequency of 71rad/s or 11.4Hz, which was used as in input to (2.138) to determine the required number of contact-wire modes: 100. The

number of modes used for each messenger span was not determined analytically, so 12 modes were used per messenger span to be conservative. This gives the messenger wire a higher maximum spatial frequency than the contact wire.

After eigenvalue decomposition and diagonalisation, the eigenvalues were inspected to determine the number of eigenmodes to include in the final ODE. The eigenvalues are plotted in order of increasing magnitude in Figure 3.2. A cut-off magnitude of 2×10^4 was used, giving a cut-off frequency of 160rad/s or 25.4Hz. This corresponds to the large step in Figure 3.2. Any eigenmodes corresponding to eigenvalues greater than this cut-off were deemed to have an insignificant effect on the results, so 161 eigenmodes were included.

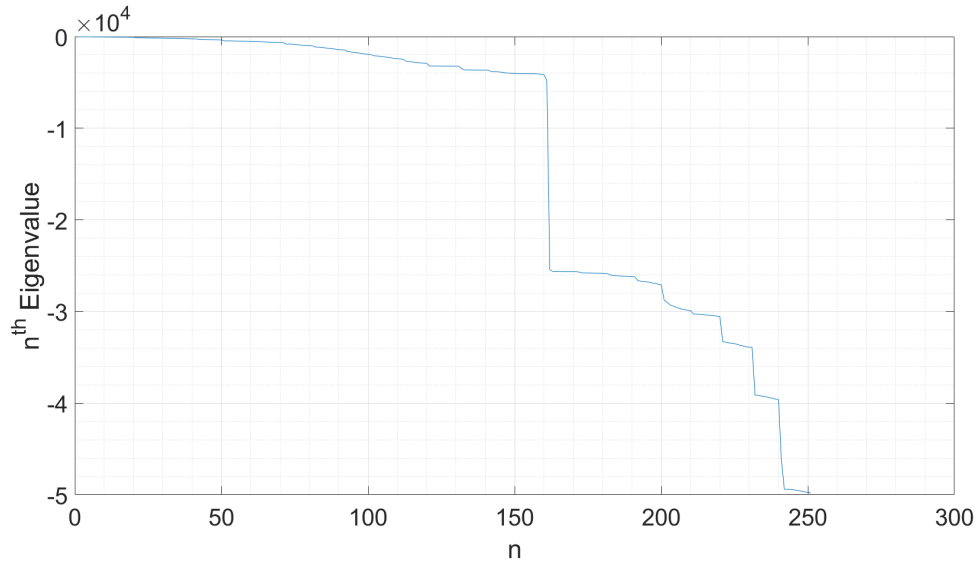


Figure 3.2: Eigenvalues of catenary system in order of increasing magnitude for BS:EN 50318:2002

Since there are 100 dropper intervals, the 100th eigenmode corresponds to one half sine wave per dropper interval. The natural frequency of this mode is 46rad/s or 7.3Hz.

3.2.5 Plots of Eigenmodes

The following plots are of the eigenmodes of the overhead catenary system. These eigenmodes describe the combined motion of the contact and messenger wires. When the ODE is solved the deflections of the overhead wires are found as a linear combination of these

eigenmodes, then the eigenvalue decomposition is reversed in order to find the deflection of each individual wire as a function of time.

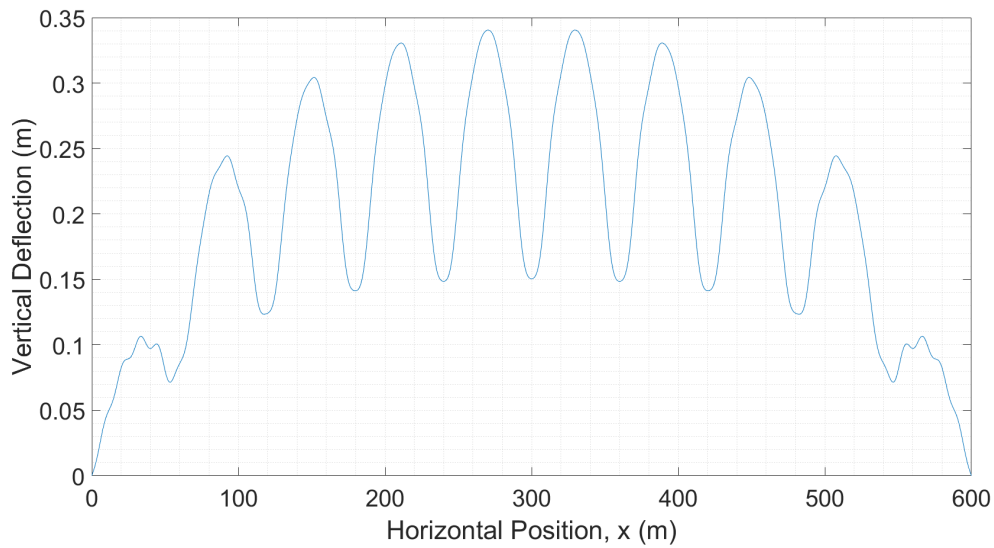


Figure 3.3: Plot of first eigenmode for BS:EN 50318:2002

The first eigenmode resembles a half sine wave over the full 600m length, modulated by a sine wave with a wavelength corresponding to the messenger spans. The stiffness of the messenger-wire supports and of the registration arms restrict the movement of the contact wire, producing the troughs in the eigenmode. These troughs are found every 60m, which is where the contact wire is attached to a registration arm. The frequency of this mode is 0.84Hz.

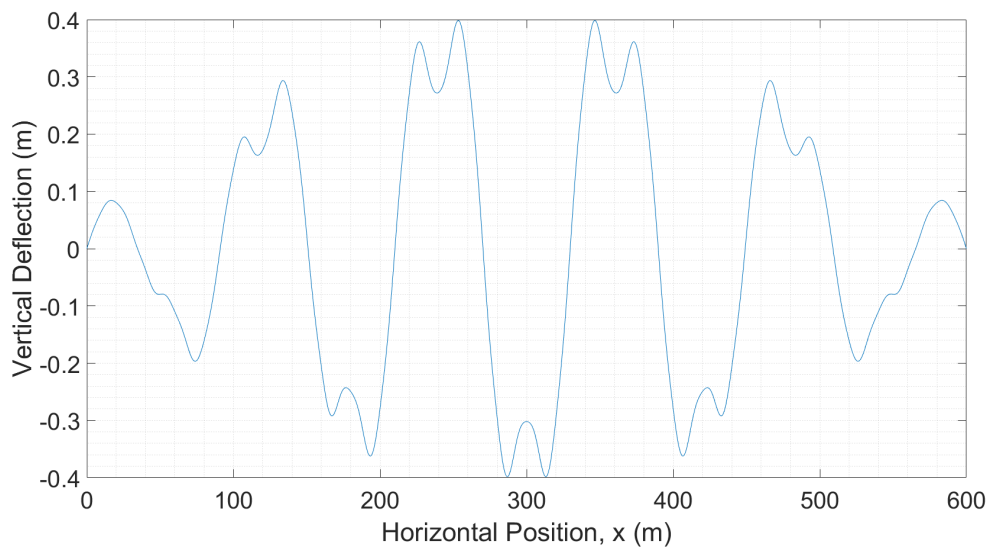


Figure 3.4: Plot of 21st eigenmode for BS:EN 50318:2002

The 21st eigenmode somewhat resembles a sine wave, but is heavily distorted. $\beta_{21} = \frac{21\pi}{L}x$, so the 21st mode for the contact wire is a sine wave with 10.5 wavelengths. This sine wave can be seen as the minor oscillations, but this eigenmode is dominated by the messenger wire and droppers. It is worth noting that the 21st eigenmode of the overall catenary system doesn't necessarily correspond to the 21st contact-wire mode, but in this case they do seem to correspond. The frequency of this mode is 1.7Hz

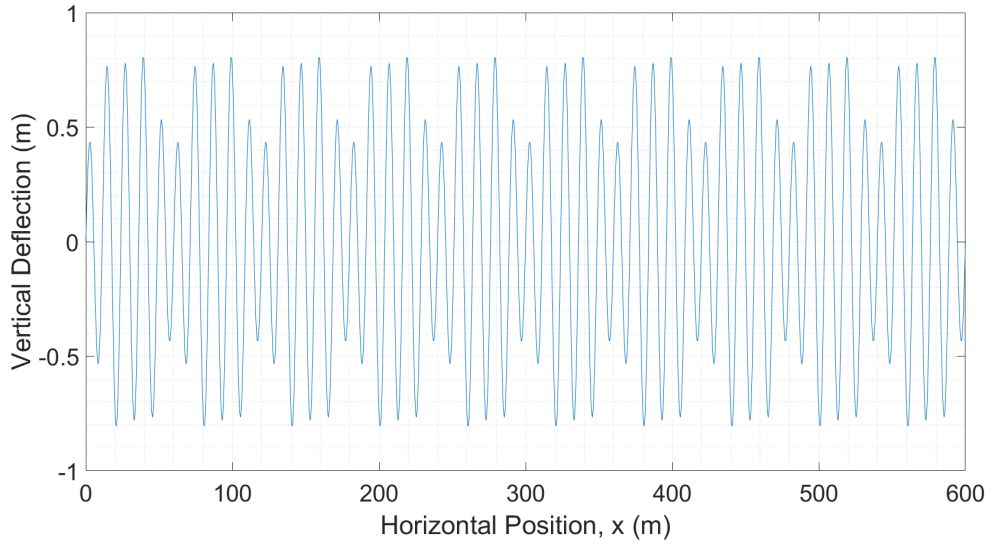


Figure 3.5: Plot of 161st eigenmode for BS:EN 50318:2002

The 161th eigenmode is a good approximation of the 100th undiagonalised contact-wire mode. However, the eigenmode's natural frequency (25.4Hz) is more than twice the natural frequency of the contact-wire mode (11.4Hz). This is because the eigenmode includes the effects of the messenger-wire supports and the registration arms, which is why the sine wave contracts at 60m intervals.

The lower-frequency eigenmodes describe the global motion of the overhead wires. The high-frequency eigenmodes, on the other hand, describe the minor local deflections in the wires. These high-frequency modes are crucial for realistically calculating the wire deflections close to the point of contact.

The cut-off frequency of the pantograph response is 11.4Hz. The frequency of the pantograph force, the rate at which the pantograph encounters the droppers, is 13.9Hz for the higher train speed of 300km/hour. Since the frequency of the last eigenmode, 25.4Hz,

is well above both of these pantograph frequencies, the diagonalised ODE should be able to realistically reproduce the excitation of the pantograph for both train speeds.

3.3 Results

3.3.1 Snapshots

Figure 3.6 shows snapshots of the vertical and horizontal deflections of the OLE system.

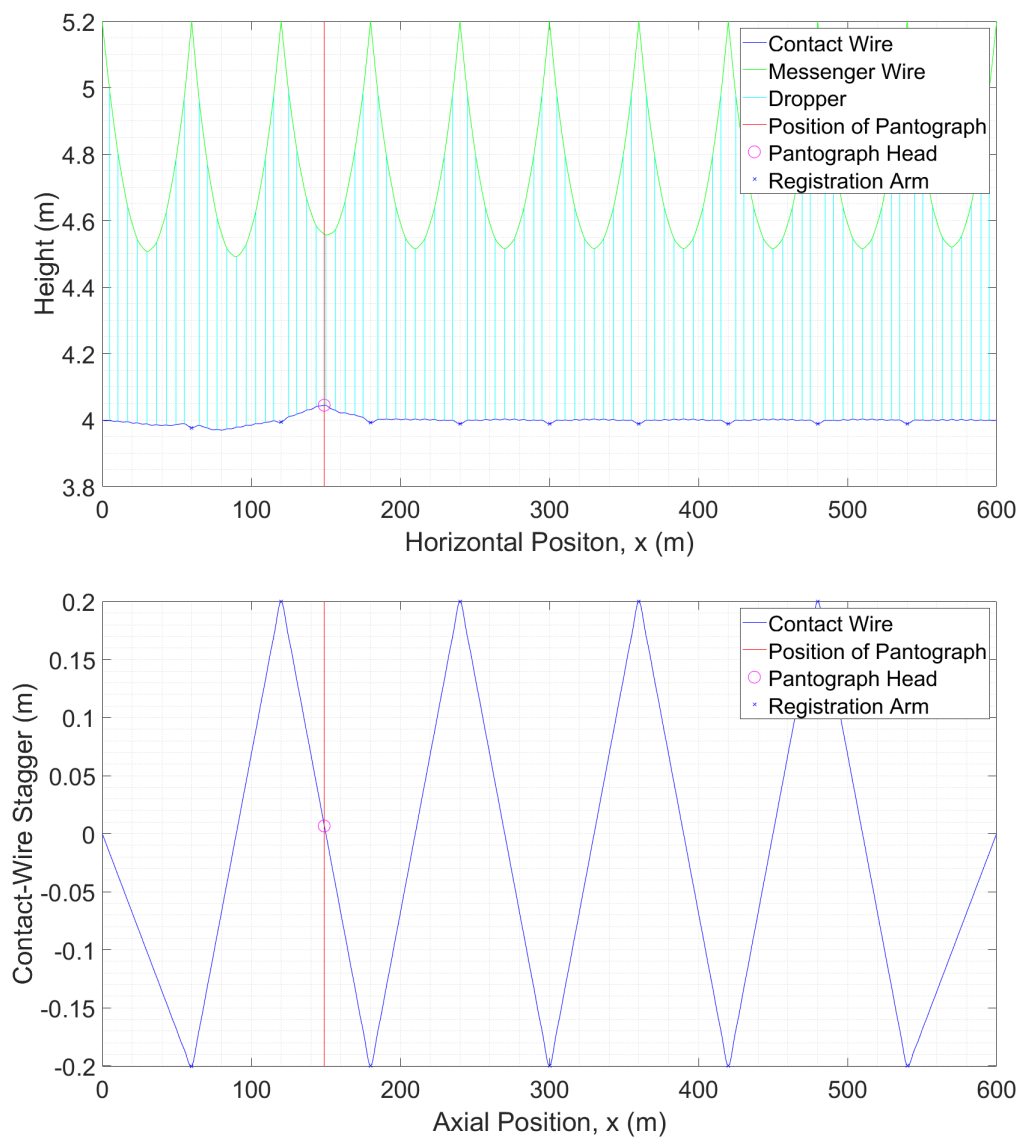


Figure 3.6: Snapshot of vertical and horizontal wire deflections at 250 km/hour for BS:EN 50318:2002

It should be noted that the the y -axis ranges for the vertical and horizontal plots are

only 2.4m and 0.4m, respectively, whereas the x -axis domain covers 600m. Therefore, the wire deflections appear far larger in these plots than when viewing a physical OLE system.

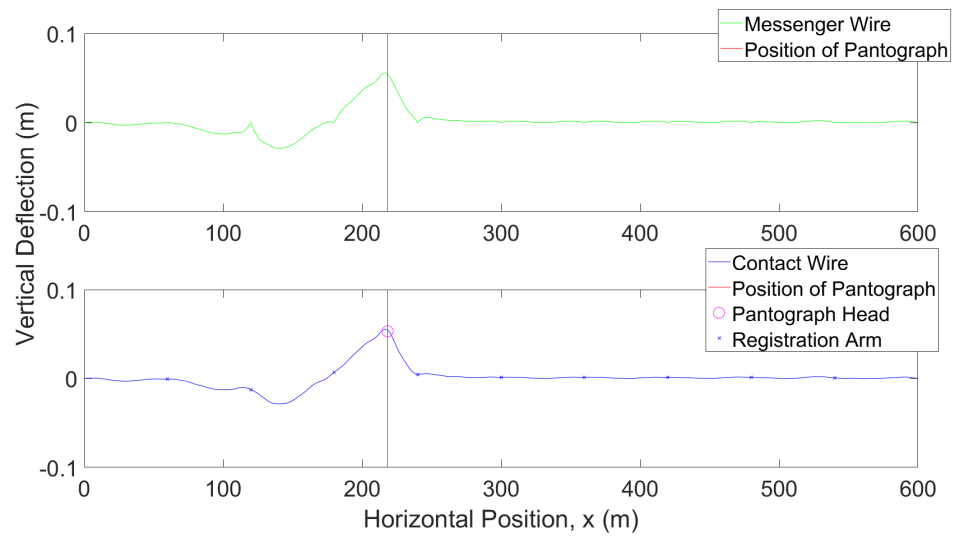
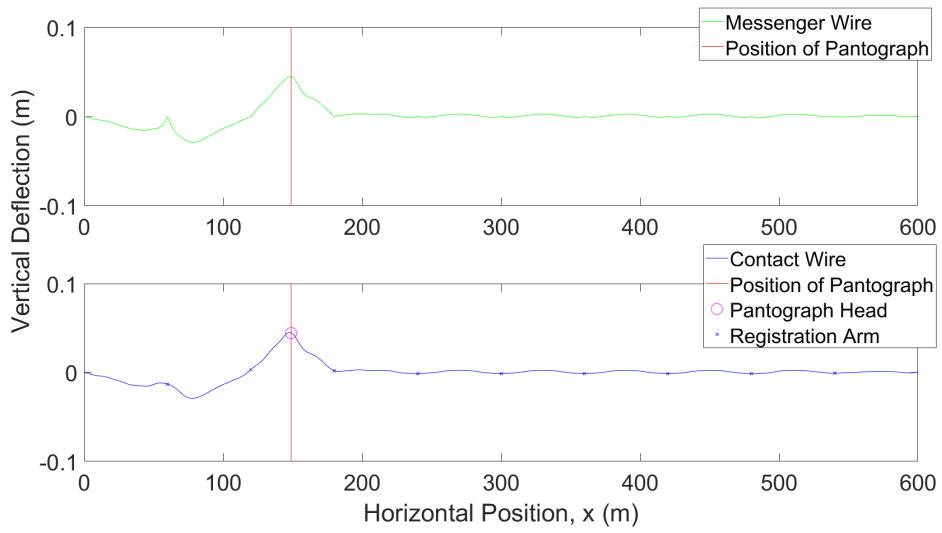
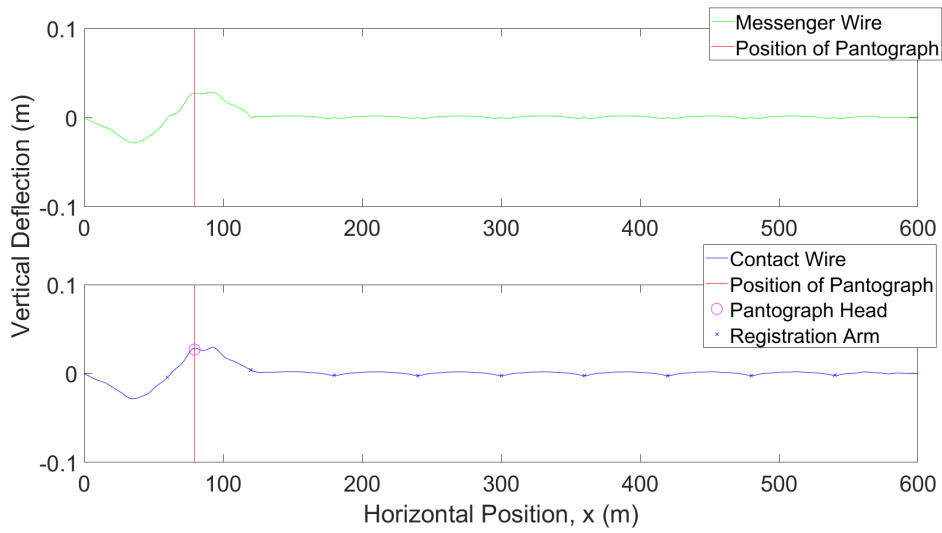
It can be seen that the dynamic horizontal deflection of the contact wire is extremely small relative to the wire's steady-state stagger, but dynamic horizontal modelling is necessary to model the deflections of the registration arms, which have a large effect on the contact force and vertical contact-wire deflection. These dynamic horizontal deflections were observed to always be negligibly small, typically under 1mm for all x . Therefore, subsequent dynamic horizontal plots have been omitted.

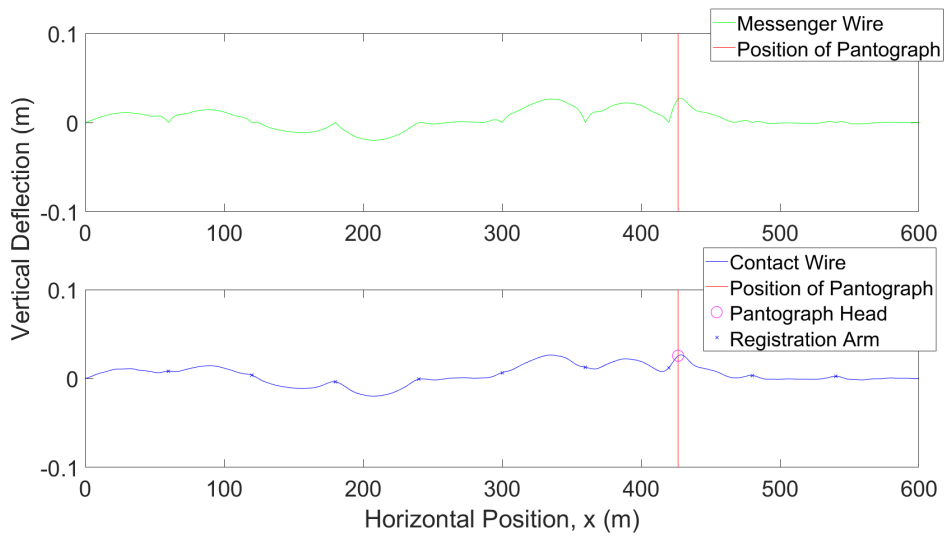
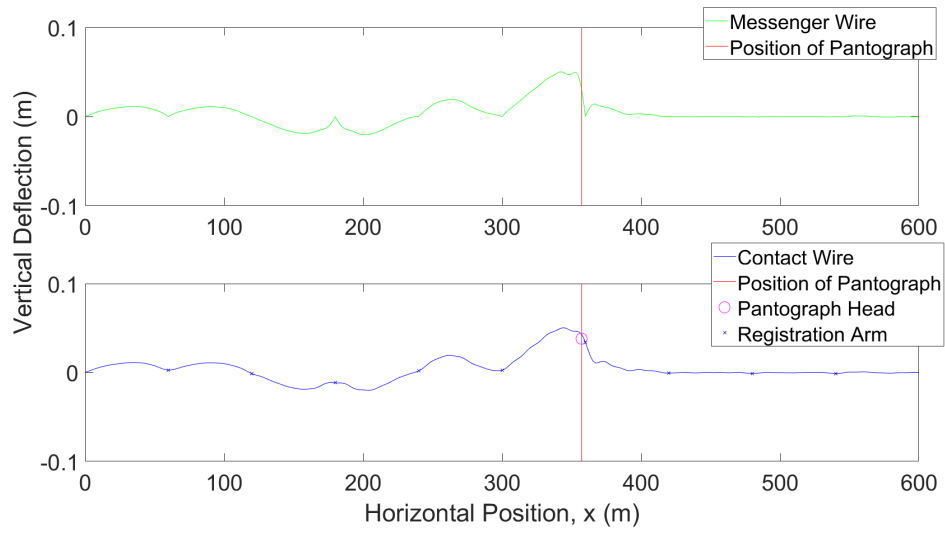
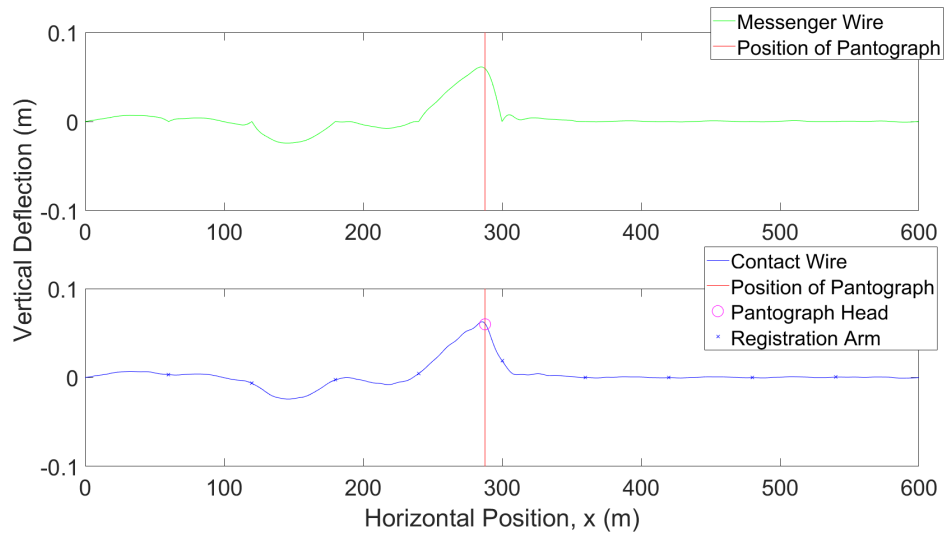
A typical change in dropper force is around 50N, which corresponds to a 0.5mm change in dropper length. Since this change in dropper length is small relative to a typical wire displacement of around 50mm, the droppers act similarly to stiff rods in the dynamic modelling. It is common for a dropper close to the point of contact to be in compression, but all other droppers will be in tension due to the steady-state forces applied to them.

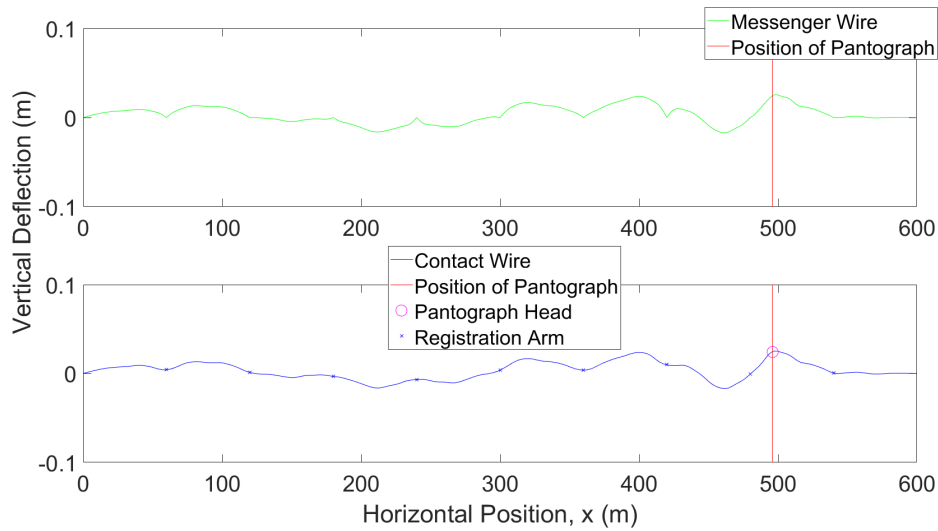
The magenta circle stays centred on the contact wire in the vertical plot, showing that the pantograph position constraint has been satisfied. Since the position constraint has been satisfied continuously, its time derivatives have not been violated.

3.3.2 Dynamic Deflections at 250 km/hour

The following snapshots show the dynamic components of the contact-wire deflection and messenger-wire deflection as the pantograph moves along the contact wire. The first snapshot shows the wires immediately before the pantograph comes into contact. Each subsequent snapshot is one second later than the preceding one.



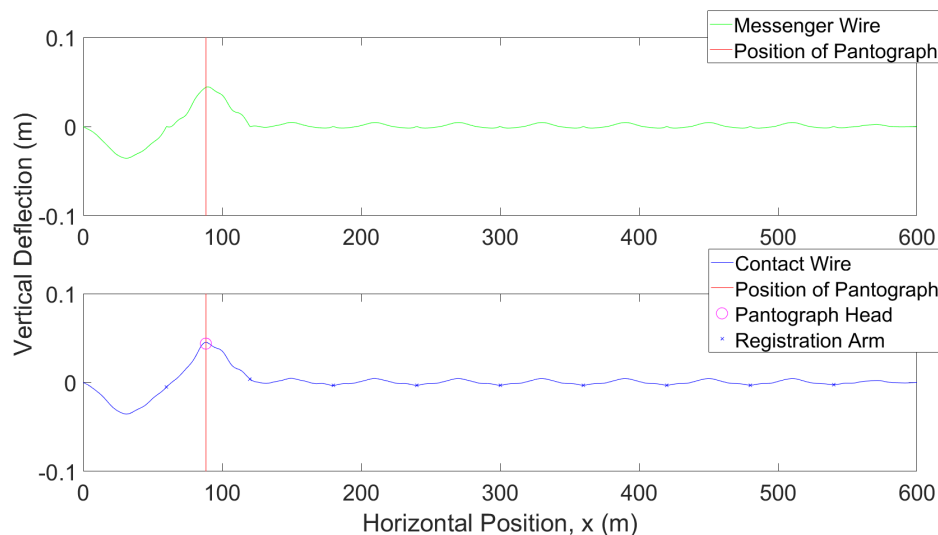


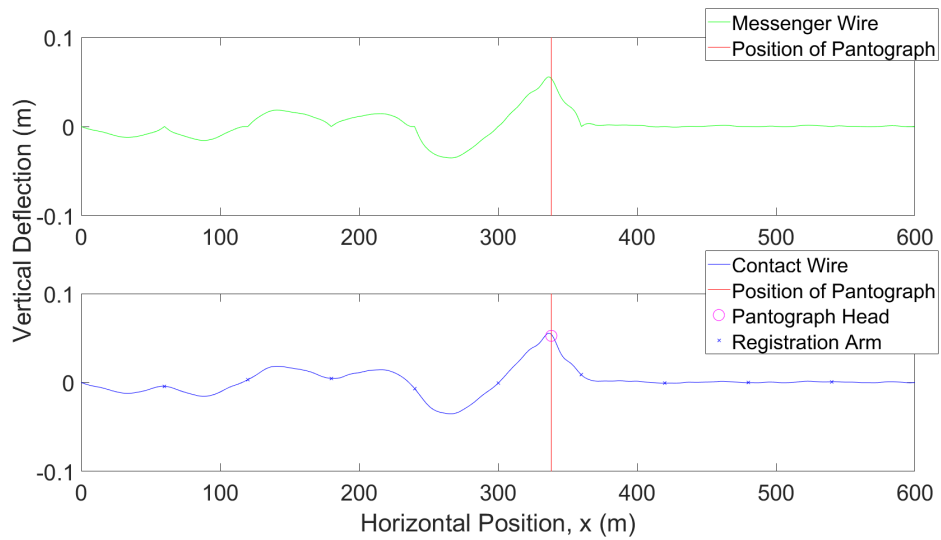
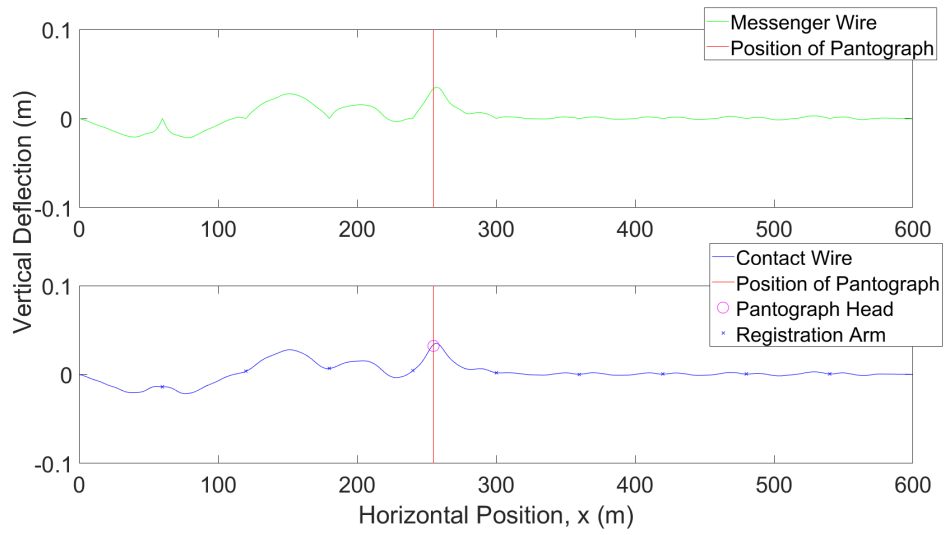
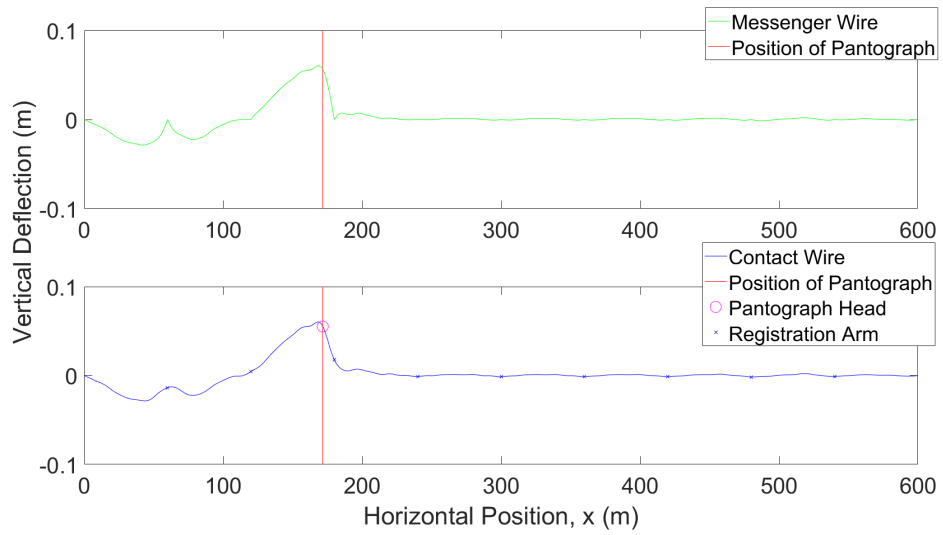


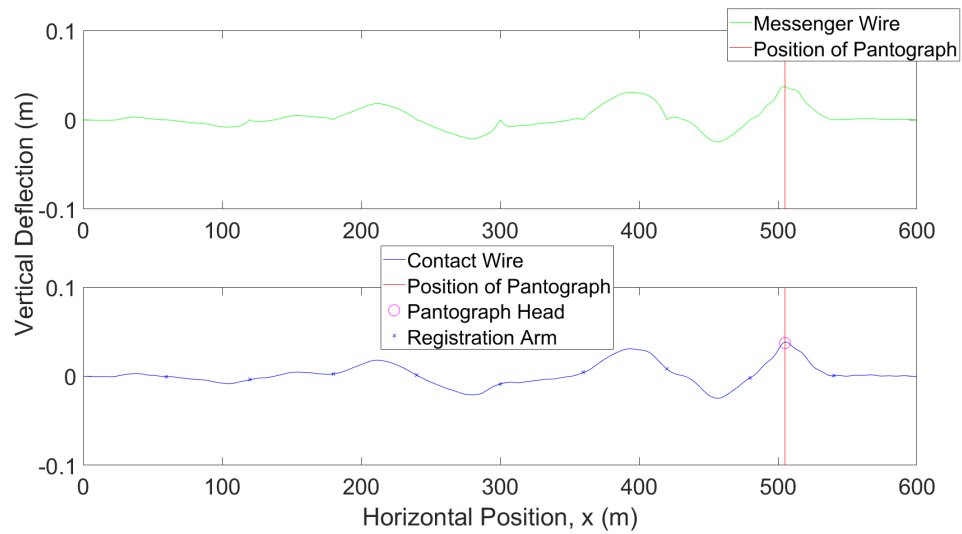
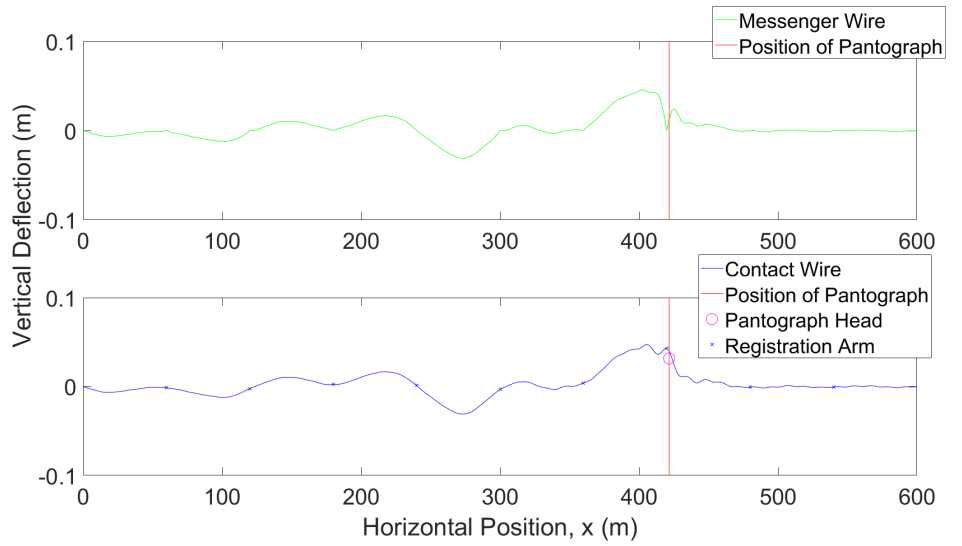
By removing the steady-state deflections, the waves formed in the overhead wires can be seen clearly. The pantograph not only perturbs the wire at the point of contact, but also leaves a wave behind it. Except for a short section immediately in front of the pantograph, the overhead lines in front of the pantograph are largely unperturbed.

It can be seen that there are kinks in the messenger wire every 60m, where the wire is fixed by its supports. There are smaller kinks in the contact wire at each registration arm, where the registration arms provide a softer restraint.

3.3.3 Dynamic Deflections at 300 km/hour







At the higher speed, the magnitude of the vertical deflections is larger. Furthermore, the spatial frequencies of the waves formed in the overhead system are a function of the speed of the train. Even as the pantograph reaches the end of the contact wire, the overhead wires at the start of the wire continue to oscillate, since there is very little damping in the overhead system.

3.3.4 Contact-Force Plots

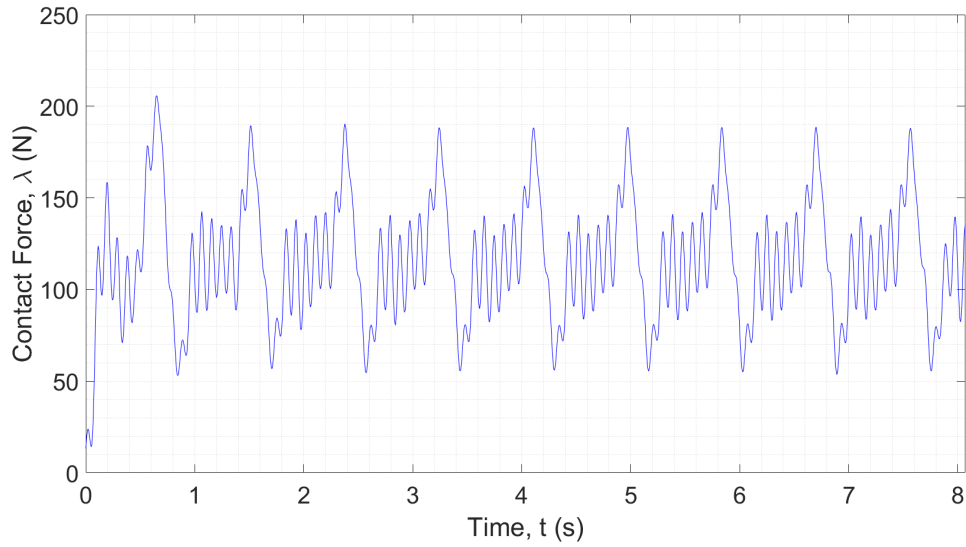


Figure 3.7: Plot of contact force against time for BS:EN 50318:2002 at 250 km/hour

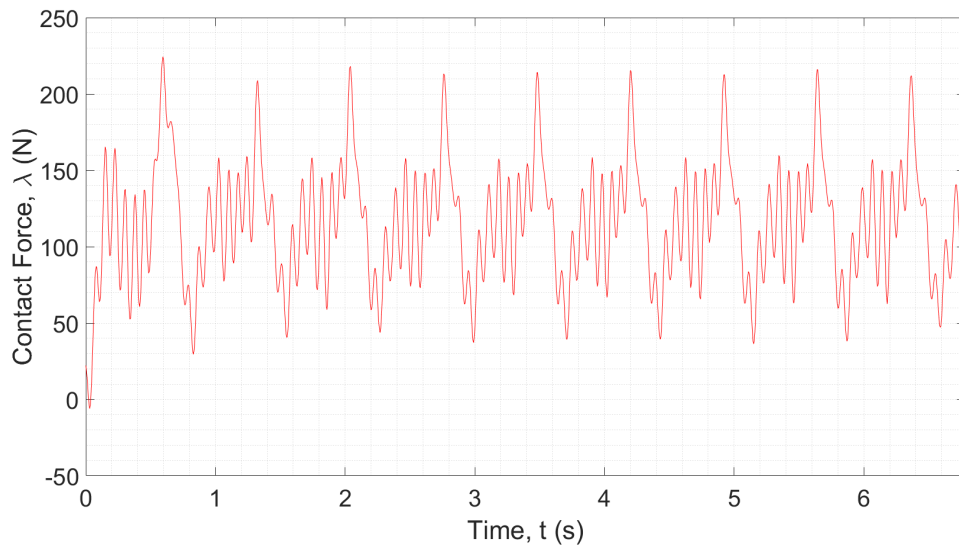


Figure 3.8: Plot of contact force against time for BS:EN 50318:2002 at 300 km/hour

Figure 3.7 and Figure 3.8 show the time profile of the contact force at 250 km/hour and at 300 km/hour, respectively. The plots show that the contact force is stable, with a small increase in maximum force shortly after the pantograph comes into contact with the wire. There is no real risk of loss of contact, nor of excessive contact force, for this OLE configuration. It can also be seen that the contact force is almost periodic; this is illustrated by Figure 3.9.

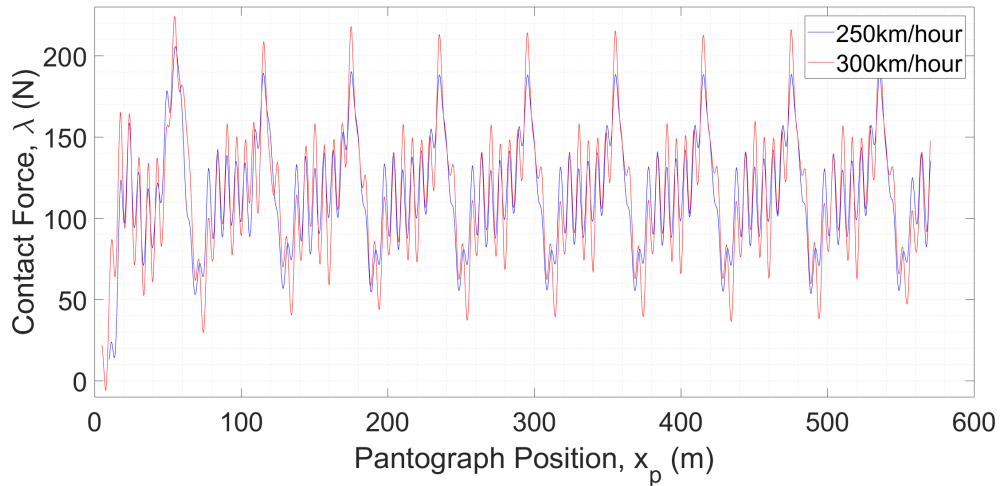


Figure 3.9: Plot of contact forces against pantograph position for BS:EN 50318:2002

By plotting the contact forces against pantograph position, rather than time, it was shown that the periodicity was due to the droppers and registration arms. The effective contact-wire stiffness is greatest close to these components, which leads to the variations in contact force. Each small oscillation is due to the pantograph passing a dropper and the large oscillation at the end of each period is caused by a registration arm.

3.3.5 Comparison to Required Results

The European Standard specifies the range of acceptable values for each result. These ranges were determined using multiple pantograph-catenary modelling programs which have been validated against real test data.

Train speed (km/hour)	250		300	
	Required	Obtained	Required	Obtained
Mean contact force (N)	110-120	116.69	110-120	116.65
Standard deviation of contact force (N)	26-31	30.88	32-40	37.46
Mean contact force – 3s.d. (N)	20-40	24.06	-5-20	4.26
Mean contact force + 3s.d. (N)	190-210	209.33	210-230	229.04
Minimum of contact force (N)	50-75	55.54	30-55	37.17
Maximum of contact force (N)	175-210	188.56	190-225	215.47
Maximum uplift at support (mm)	48-55	48.04	55-65	55.13
Percentage loss of contact (%)	0	0.00	0	0.00
Damping factor	-	0.055	-	0.040

Table 3.2: Table of results for validation against BS:EN 50318:2002

Every result is in the specified range, indicated by the green numbers in the table above. There was no loss of contact and no problems were observed in the animation of catenary-wire deflections.

The damping factors shown in the above table were larger than the European Standard suggests, but still reasonable; while the European Standard specifies that the only damping included in the model should be the damping of the pantograph, it was clarified in a discussion with Furrer+Frey that all other modelling software has had to use damping in the overhead wires in order to give the required results. Overhead wires in the real world are lightly damped, as they lose energy for various reasons, so it is realistic to use a small, nonzero damping factor. All of the later models presented in this thesis also include wire damping.

The damping factors were chosen to minimise damping while making sure that all of the results fell in the required ranges. Modal damping was used and the same value was used for each mode.

3.3.6 Verification Using MATLAB Code

In order to verify the results obtained by the Simulink model, MATLAB code was written to simulate the same system. This code used the same solution process, as well as identical parameters, and served to check for errors in the Simulink model.

Train speed (km/hour)	250		300	
	Simulink	MATLAB	Simulink	MATLAB
Mean contact force (N)	116.69	116.71	116.65	116.62
Standard deviation of contact force (N)	30.88	31.03	37.46	37.72
Mean contact force – 3s.d. (N)	24.06	23.62	4.26	3.46
Mean contact force + 3s.d. (N)	209.33	209.79	229.04	229.78
Minimum of contact force (N)	55.54	54.86	37.17	37.19
Maximum of contact force (N)	188.56	188.88	215.47	215.34
Maximum uplift at support (mm)	48.04	48.07	55.13	54.09
Percentage loss of contact (%)	0.00	0.00	0.00	0.00

Table 3.3: Comparison of results from Simulink and MATLAB for BS:EN 50318:2002

The MATLAB code shows excellent agreement with the Simulink model. The small discrepancy in numerical results is due to the differences in solver settings. Although two

of the MATLAB results fall just outside their required ranges, the input parameters could be adjusted to achieve satisfactory results. The purpose of this verification process is to show that the Simulink model is realistic and error-free.

While the ODE-solver settings, preprocessing code and postprocessing code could be tweaked to make the numerical results identical, the Simulink model has two main advantages over MATLAB:

1. The velocity profile of the train can be chosen during the simulation. For example, the program could take an input from a joystick.
2. Scopes can be used to plot signals while the simulation is running.

The MATLAB code can take any velocity profile as an input, but that profile has to be determined before the simulation is started. The Simulink model can allow a human ‘driver’ to see the contact-force profile, react to it and change the velocity of the train accordingly.

3.3.7 Simulation Speed

All of the simulations were performed on a Windows desktop machine with a quadcore processor. No attempt was made to dedicate memory or CPU cores to the solver.

The Simulink model uses ode45 to solve the differential equation. This algorithm was chosen due to its high speed when solving nonstiff differential equations. The error tolerances chosen to maximise the simulation speed while providing sufficient realism. The realism of the solution was evaluated both by checking the results against the benchmark and by running simulations with lower error tolerance and ensuring consistent results. The error tolerances chosen were 10^{-3} relative tolerance and 10^{-6} absolute tolerance.

Train speed (km/hour)	250	300
Pre-processing (s)	0.08	0.08
Simulation time (s)	5	4
Post-processing (s)	0.08	0.08
Real time (s)	8.07	6.73

Table 3.4: Simulink simulation speeds for BS:EN 50318:2002

In both simulations, the eigenmodes of the DAE were lightly damped. The damping factors used are larger than the European Standard suggests, but still within reason.

The real time is the time taken by the train to move along the contact wire, i.e. the amount of time that the results represent, whereas the simulation time is the time taken by the model to calculate the results. The simulation times are substantially faster than real time and could be improved further.

3.4 Conclusions

The Simulink model was used to simulate the interaction between a single pantograph and a single contact wire. This yielded believable results and showed some important characteristics of the pantograph-catenary interaction, such as the formation of a trailing wave behind the moving pantograph. This trailing wave is a crucial aspect of the analysis of close, coupled pantographs, which will be studied in the next chapter.

The results met all of the requirements of the 2002 European Standard at both 250 km/hour and 300 km/hour. Furthermore, the simulation was significantly faster than real time. However, the level of modal damping required to ensure the results were as required by the European Standard was high. This was probably because the model for the overhead-wire system included no other forms of damping.

This validation serves as a promising initial proof of concept of the Galerkin approach for pantograph-catenary modelling. However, this model did not include dropper unloading, damping at the messenger-wire supports, multiple pantographs or contact-wire transitions. Therefore, further modelling was required to show that these could be implemented while maintaining the realism and speed of the initial model.

Chapter 4

Validation Against BS:EN 50318:2018

4.1 Introduction

This chapter covers the process of validating the Simulink model against BS:EN 50318:2018 [35]. This European Standard was designed to replace the 2002 European Standard. It tests new simulation software more thoroughly and includes various catenary topologies in order to accommodate simulations designed for different OLE configurations.

One example of a different catenary topology that may be chosen for this validation is the stitched messenger wire, where an additional wire is attached to the messenger wire at each messenger support and used to support the contact wire via the droppers. This OLE design is common in France and Germany, but is not currently supported by the new software presented in this thesis.

The AC - Simple catenary system was chosen for this validation, because this design is very common in real-world pantograph systems and, therefore, validation using this OLE design demonstrates that the software is widely applicable to real catenary systems. The AC - Simple system is also convenient insofar as it is very similar to the system considered in Chapter 3.

While similar to the previous standard, the 2018 European Standard increases the complexity of the model in three ways:

1. There are now two pantographs in contact with the same contact wire, separated by

200m.

2. Dropper unloading must be included in the model.
3. The messenger wire is attached to each support by a spring and a damper, as described in Section 2.2.2.

The pantograph model is identical for each pantograph and has three masses, as shown in Figure 2.1b. The equations of motions are given by (2.3)-(2.5).

The set-up of a single messenger span is pictured in Figure 4.1. The number of messenger spans per contact wire is not prescribed in the standard, but the configuration of each messenger span is prescribed by the 2018 European Standard.

The 55m messenger span prescribed by the 2018 European Standard is shorter than the 60m span prescribed by the 2002 European Standard and the prescribed train speeds of 275km/hour and 320km/hour are higher than those prescribed by the 2002 European Standard. These changes reflect the changes in real-world catenary design as train speeds have increased. Both of these changes increase the frequency at which the train encounters droppers, which means that higher-frequency effects in the overhead wires must be modelled.

The flat section at each end of the messenger span is to allow the registration arms to clamp on to the contact wire horizontally. The Simulink model does not require this flat section, but it is prescribed by the European Standard.

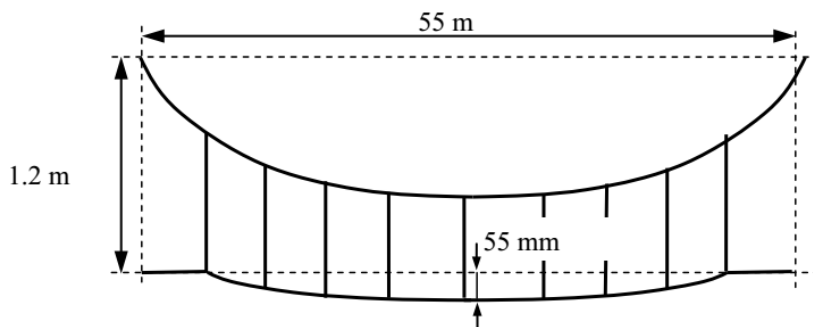


Figure 4.1: Image of single span taken from BS:EN 50318:2018

The standard requires that certain properties of the contact-force profile, the maximum uplift at a support and the range of displacement of the pantograph head all fall within

specified ranges. The analysis section is ten spans long and the train speeds are 275 km/hour and 320 km/hour.

4.2 Model Updates

4.2.1 Multiple Pantographs

$\tilde{S}(\underline{x}_p(t))$ -Matrix

With multiple pantographs come multiple contact constraints. The individual contact constraints given by (4.1) and (4.2) are combined into a vector equation in (4.3)-(4.4). The elimination of $\tilde{q}_1(t)$ is shown in (4.5), where $\tilde{q}_1(t)$ is a 2×1 vector containing the two eliminated states. The expressions for $\dot{\tilde{q}}_1(t)$ and $\ddot{\tilde{q}}_1(t)$ are also analogous to those given in Section 2.3.12.

$$z_3^f(t) + \bar{z}_3^f - \sin\left(\tilde{\beta}x_p^f(t)\right)^T V\tilde{q}(t) - \sin\left(\bar{\beta}x_p^f(t)\right)^T \bar{q} = 0 \quad (4.1)$$

where $z_3^f(t)$ is the height of the head of the front pantograph and $x_p^f(t)$ the horizontal position of the front pantograph.

$$z_3^b(t) + \bar{z}_3^b - \sin\left(\tilde{\beta}x_p^b(t)\right)^T V\tilde{q}(t) - \sin\left(\bar{\beta}x_p^b(t)\right)^T \bar{q} = 0 \quad (4.2)$$

where $z_3^b(t)$ is the height of the head of the rear pantograph and $x_p^b(t)$ the horizontal position of the rear pantograph.

$$\begin{aligned} \begin{pmatrix} z_3^f(t) \\ z_3^b(t) \end{pmatrix} + \begin{pmatrix} \bar{z}_3^f \\ \bar{z}_3^b \end{pmatrix} - \sin\left(\tilde{\beta} \begin{pmatrix} x_p^f(t) & x_p^b(t) \end{pmatrix}\right)^T V\tilde{q}(t) \\ - \sin\left(\bar{\beta} \begin{pmatrix} x_p^f(t) & x_p^b(t) \end{pmatrix}\right)^T \bar{q} = \begin{pmatrix} 0 \\ 0 \end{pmatrix} \end{aligned} \quad (4.3)$$

$$\begin{pmatrix} z_3^f(t) \\ z_3^b(t) \end{pmatrix} + \begin{pmatrix} \bar{z}_3^f \\ \bar{z}_3^b \end{pmatrix} - S(t) \left(V_1 \tilde{q}_1(t) + V_2 \tilde{q}_2(t) \right) - \bar{S}(t) \bar{q} = \begin{pmatrix} 0 \\ 0 \end{pmatrix} \quad (4.4)$$

$$\tilde{q}_1(t) = \tilde{S}^{-1}(\underline{x}_p(t)) \left(\begin{pmatrix} z_3^f(t) \\ z_3^b(t) \end{pmatrix} + \begin{pmatrix} \bar{z}_3^f \\ \bar{z}_3^b \end{pmatrix} - S(\underline{x}_p(t)) V_2 \tilde{q}_2(t) - \bar{S}(\underline{x}_p(t)) \bar{q} \right) \quad (4.5)$$

$$\bar{S}(\underline{x}_p(t)) = \sin \left(\bar{\underline{\beta}} \begin{pmatrix} x_p^f(t) & x_p^b(t) \end{pmatrix} \right)^T = \sin \left(\bar{\underline{\beta}} \underline{x}_p(t)^T \right)^T \quad (4.6)$$

$$S(\underline{x}_p(t)) = \sin \left(\tilde{\underline{\beta}} \begin{pmatrix} x_p^f(t) & x_p^b(t) \end{pmatrix} \right)^T = \sin \left(\tilde{\underline{\beta}} \underline{x}_p(t)^T \right)^T \quad (4.7)$$

$$\tilde{S}(\underline{x}_p(t)) = S(\underline{x}_p(t)) V_1 \quad (4.8)$$

$$\underline{x}_p(t) = \begin{pmatrix} x_p^f(t) \\ x_p^b(t) \end{pmatrix} \quad (4.9)$$

where V_1 contains the two columns of V that correspond to the two eliminated eigenmodes. V_2 contains all of the remaining columns. $\tilde{q}_2(t)$ contains all of the $\tilde{q}(t)$ -terms that are not being eliminated. $\tilde{S}(\underline{x}_p(t))$ is a 2×2 matrix that must be nonsingular so that inversion is possible.

$\tilde{F}_1(\underline{x}_p(t))$ -Matrix

The elimination of $\underline{\lambda}(t) = \begin{pmatrix} \lambda_1(t) \\ \lambda_2(t) \end{pmatrix}$ also requires the inversion of a 2×2 matrix, $\tilde{F}_1(\underline{x}_p(t))$ in (4.10).

$$\ddot{\underline{q}}_1(t) = -\eta \dot{\underline{q}}_1(t) + \Lambda_1 \tilde{q}_1(t) + \tilde{F}_1(t) \underline{\lambda}(t) \quad (4.10)$$

$$\underline{\lambda}(t) = \tilde{F}_1^{-1}(t) \left(\ddot{\underline{q}}_1(t) + \eta \dot{\underline{q}}_1(t) - \Lambda_1 \underline{q}_1(t) \right) \quad (4.11)$$

$$\tilde{F}_1(\underline{x}_p(t)) = \frac{2}{\rho AL} W_1 (I - A_3)^{-1} S(\underline{x}_p(t)) \quad (4.12)$$

where W_1 contains the two rows of W which correspond to the two eliminated eigenmodes.

The two eliminated eigenmodes, $\tilde{\underline{q}}_1(t)$, were chosen carefully to avoid singular $\tilde{S}(\underline{x}_p(t))$ - and $\tilde{F}_1(\underline{x}_p(t))$ -matrices. For the catenary system in this section, $\tilde{\underline{q}}_1(t) = \begin{pmatrix} \tilde{q}_2(t) \\ \tilde{q}_3(t) \end{pmatrix}$ was found to be suitable.

4.2.2 Dropper Unloading

Droppers were modelled as linear springs in tension, but exerted no force in compression. Since the dropper forces contributed to the A_1 -matrix before diagonalisation, the terms corresponding to any unloaded droppers were removed. The static force applied by an unloaded dropper was also removed.

Detection

A dropper is unloaded if and only if the inequality in (4.13) is satisfied.

$$w^m(x_{d,i,j}^m, t) - w(x_{d,i,j}, t) = \underline{u}_{d,i,j}^T \tilde{\underline{q}}(t) < L_{d,i,j}^{\text{unstretched}} \quad (4.13)$$

where $\underline{u}_{d,i,j}^T$ is a constant row vector that is evaluated in pre-processing and is specific to a single dropper. $\tilde{\underline{q}}(t)$ is the reconstructed full vector of eigenmodes. The detection inequalities for all droppers were compiled into a single matrix equation, (4.14), which was used to form a binary vector which indicated unloaded droppers, $\underline{i}(t)$.

$$U_d \tilde{\underline{q}}(t) < \underline{L}_d^{\text{unstretched}} \quad (4.14)$$

Removal of Dynamic Compressions

The dropper-force matrices evaluated in Section 2.2.4 were used to remove the dynamic force for each unloaded dropper.

$$\ddot{\underline{q}}(t) = \tilde{\Lambda}\tilde{\underline{q}}(t) + \tilde{B}\dot{\tilde{\underline{q}}}(t) + \tilde{F}_1(\underline{x}_p(t))\underline{\lambda}(t) - WK_{\text{unload,left}}\text{diag}\{\underline{i}(t)\}K_{\text{unload,right}}V\tilde{\underline{q}}(t) \quad (4.15)$$

where $\underline{i}(t)$ is the binary dropper-unloading indicator vector.

$K_{\text{unload,left}}$ and $K_{\text{unload,right}}$ were evaluated in pre-processing, before diagonalisation. The formula given in Section 4.15 was used to remove any and all dynamic forces for unloaded droppers with a single matrix equation.

Removal of Static Tensions

The static dropper extension, $\bar{L}_{d,i,j} - L_{d,i,j}^{\text{unstretched}}$, was calculated for each dropper in the steady-state code, where it was taken that no droppers were in compression. The static dropper tension was evaluated using (2.25) and an equal and opposite force was applied to the messenger wire and contact wire for each dropper in order to counteract this static tension.

$$\begin{aligned} \ddot{\underline{q}}(t) = & \tilde{\Lambda}\tilde{\underline{q}}(t) + \tilde{B}\dot{\tilde{\underline{q}}}(t) + \tilde{F}_1(\underline{x}_p(t))\underline{\lambda}(t) - \bar{K}_{\text{unload}}\text{diag}\{\underline{i}(t)\} \\ & - WK_{\text{unload,left}}\text{diag}\{\underline{i}(t)\}K_{\text{unload,right}}V\tilde{\underline{q}}(t) \end{aligned} \quad (4.16)$$

where \bar{K}_{unload} is independent of the state vector, because it is only a function of steady-state deflections.

Limitations

There are two limitations that reduce the realism of the dropper-unloading model:

1. The $\ddot{\underline{q}}_1(t)$ -equations cannot be updated without altering the elimination of variables based on the current set of unloaded droppers. This is not feasible, so the unloading

terms in these equations were omitted.

2. Dropper unloading affects the pre-diagonalisation A_1 -matrix. This means that the eigenvector decomposition is an approximation whenever at least one dropper is unloaded.

4.3 Results

For all simulations, the contact wire was 990m long, consisting of eighteen uniform spans. This number was chosen in order to match the frequency characteristics of the benchmark catenary system, which are indicated by the standard deviations of filtered forces, as well as to approximately match the length of a typical real-world catenary system.

The frequency cut-off used for the three-mass pantograph model was 85rad/s or 13.6Hz. This was chosen to give a minimum 90dB attenuation of any higher-frequency excitations. This frequency was used as an input to (2.138) to give the number of contact-wire modes: 210. The number of messenger-wire modes per span was conservatively chosen to be 22, giving a higher maximum spatial frequency for the messenger wire than for the contact wire.

The standard requests the filtered contact forces in three frequency ranges: 0-5Hz, 0-20Hz and 5-20Hz. Ideal filters, which attenuated no frequencies within the passband and accepted no frequencies outside it, were applied to the time profile of the contact force in post-processing for each pantograph in order to recover the filtered force profiles. The force plots in Section 4.3.2 show the unfiltered contact forces.

As before, ode45 was used to solve the ODE. The relative tolerance was 10^{-3} and the absolute tolerance was 10^{-6} . Much more work could be done to optimise the solver settings, but these settings are sufficient for a proof of concept of the Galerkin approach.

4.3.1 Snapshots

Figure 4.2 shows a snapshot of the total wire deflections at 275 km/hour. It can be seen that the section of contact wire immediately in front of the rear pantograph has been

perturbed by the front pantograph, so the interaction between the rear pantograph and the contact wire is influenced by the front pantograph. The front pantograph is not affected significantly by the rear pantograph. This is in agreement with the results presented in [48].

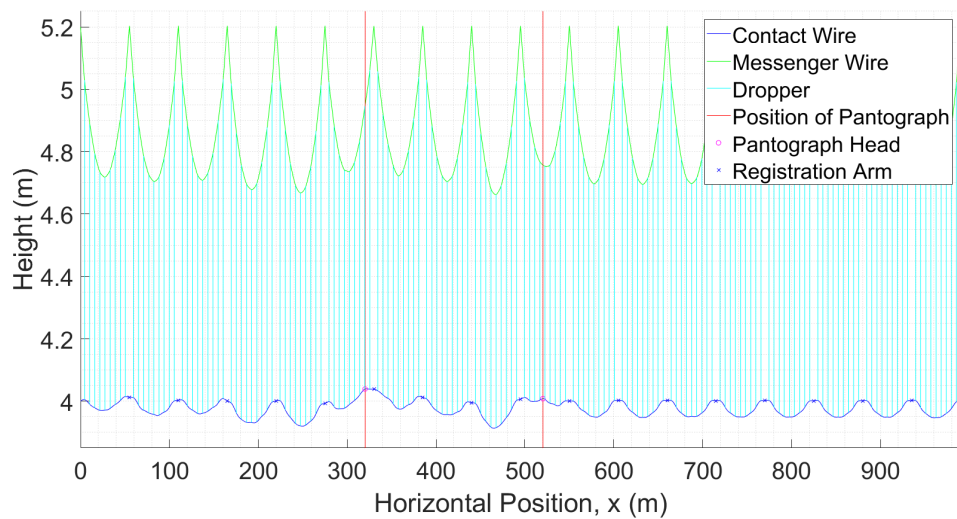
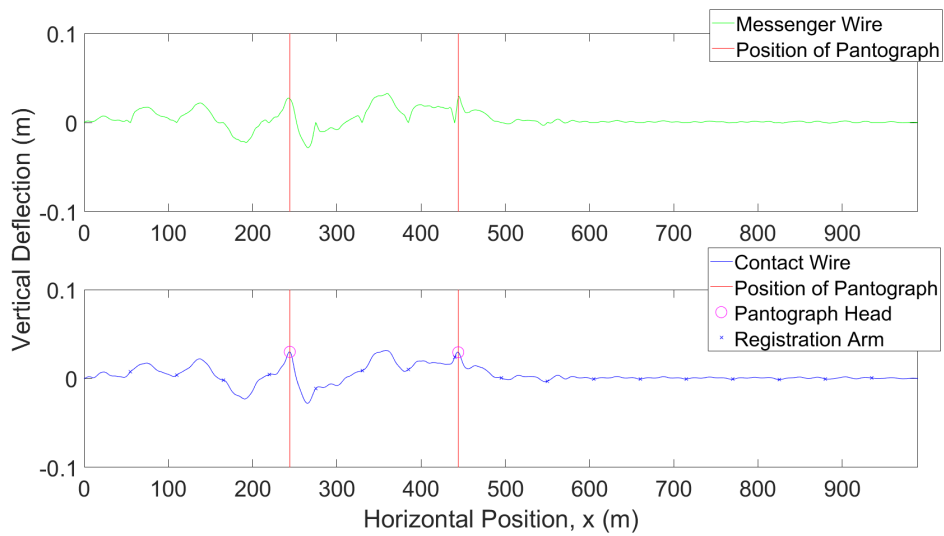
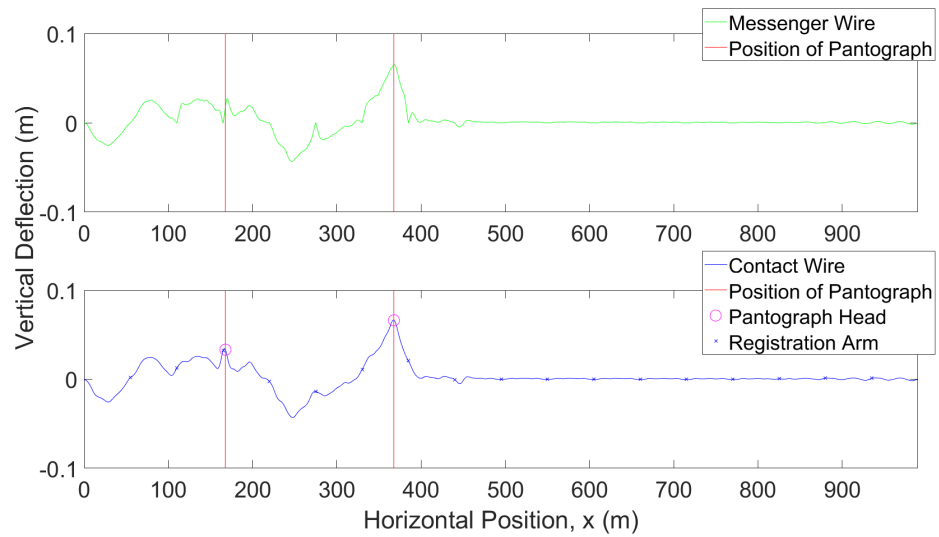
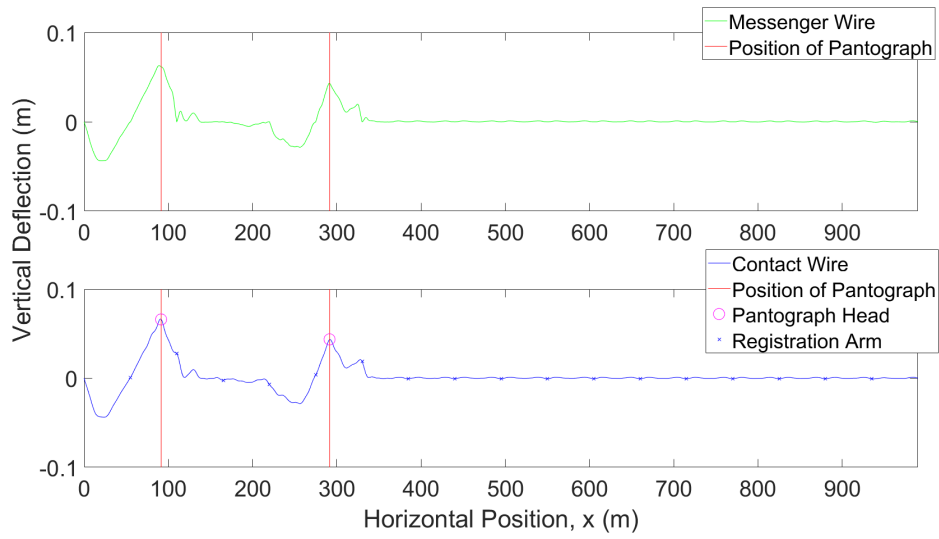
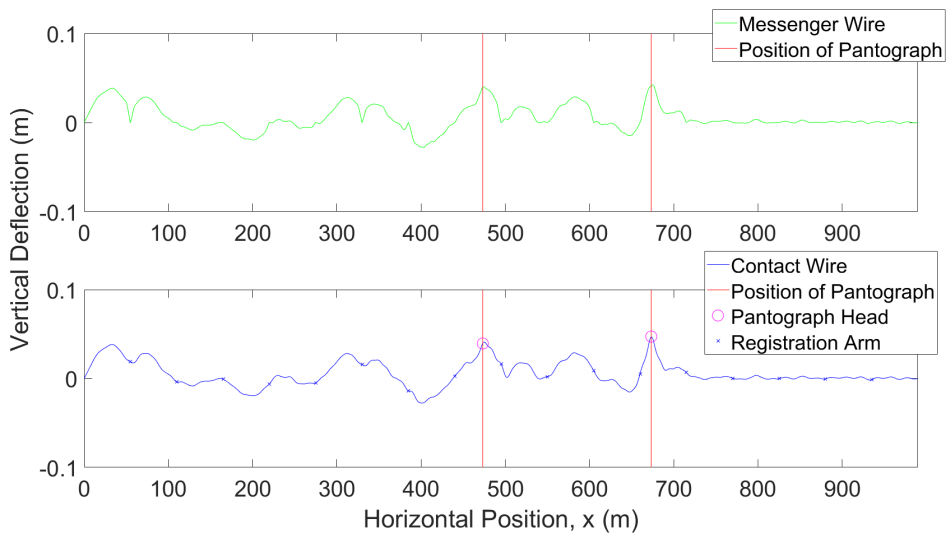
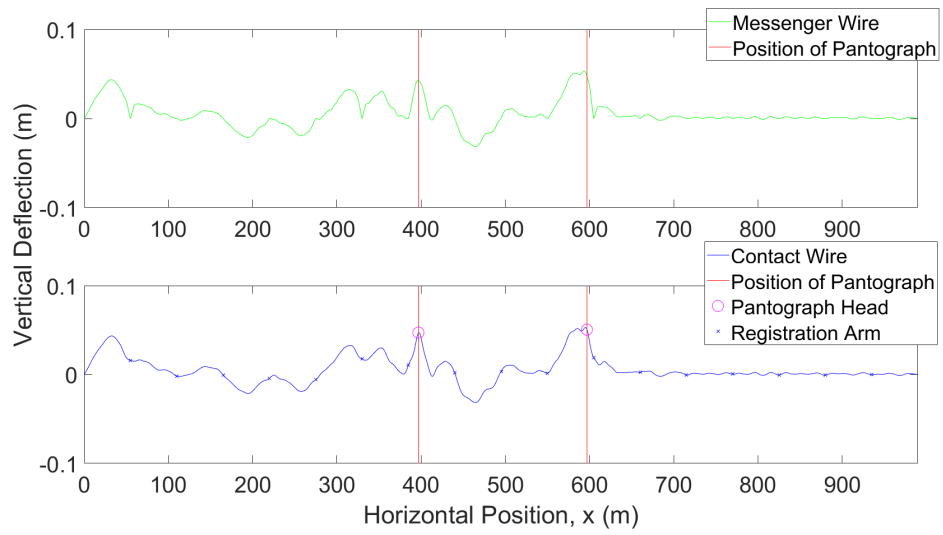
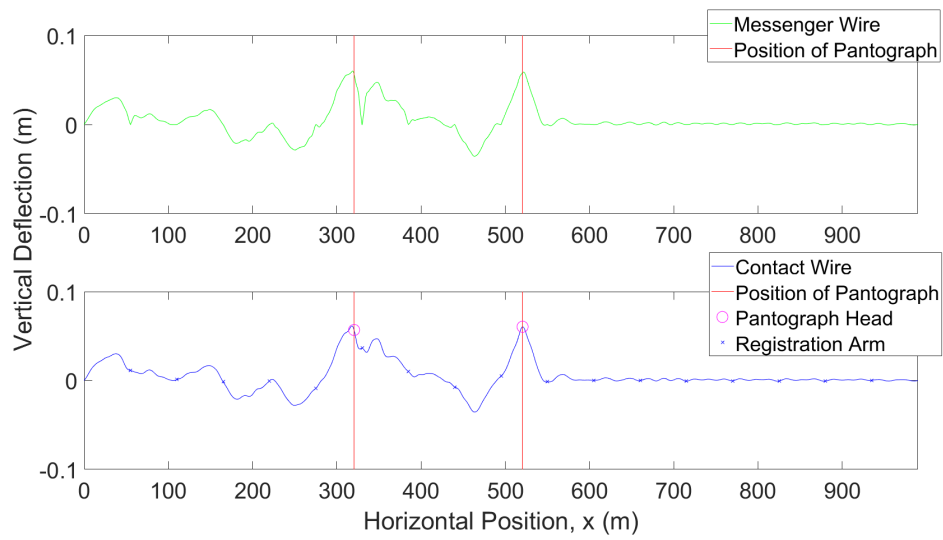


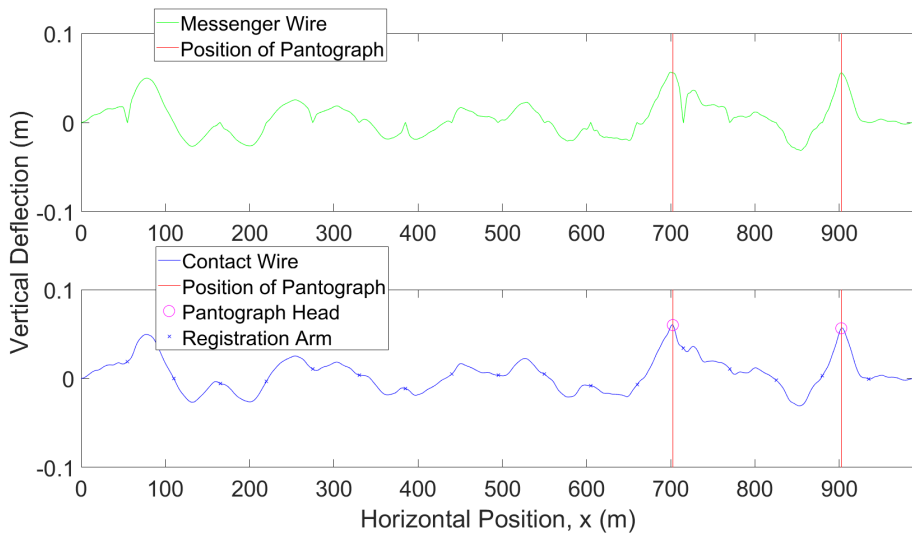
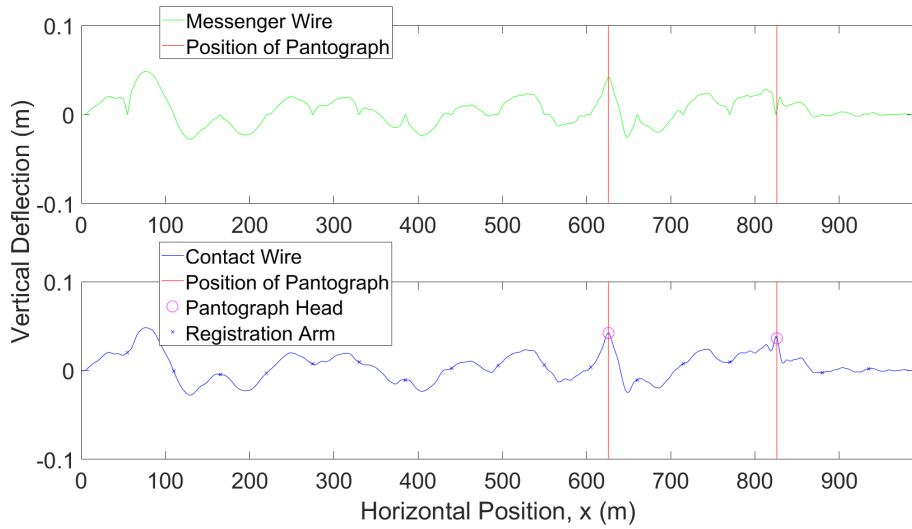
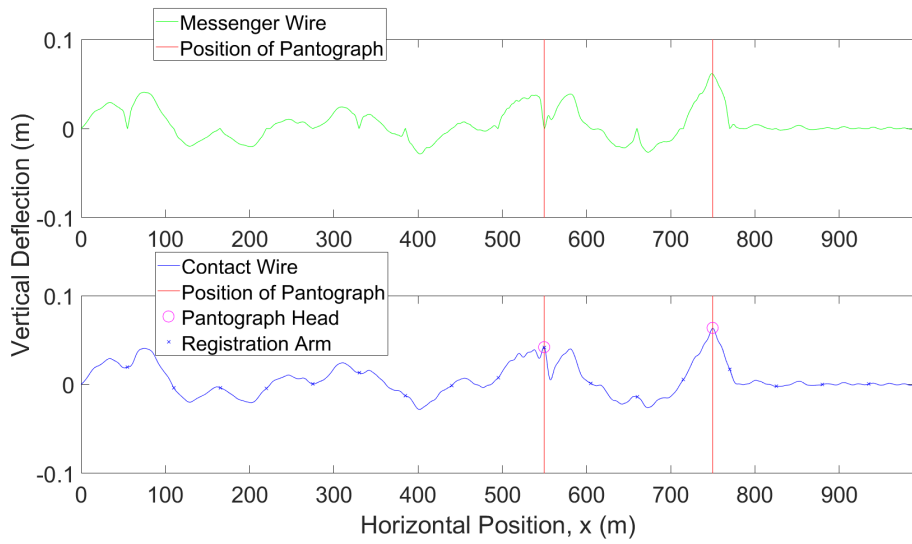
Figure 4.2: Snapshot of total (static and dynamic) vertical wire deflections at 275 km/hour for BS:EN 50318:2018

The contact-wire sag is much greater here than it was for the 2002 European Standard. This is because the dropper arrangement specified by the 2018 standard is more realistic. The snapshots again exaggerate the sag due to the difference in axis scales: the maximum sag is 55mm, whereas the contact-wire length is 990m. The dynamic horizontal deflections were found to be negligible.

Dynamic Deflections at 275 km/hour

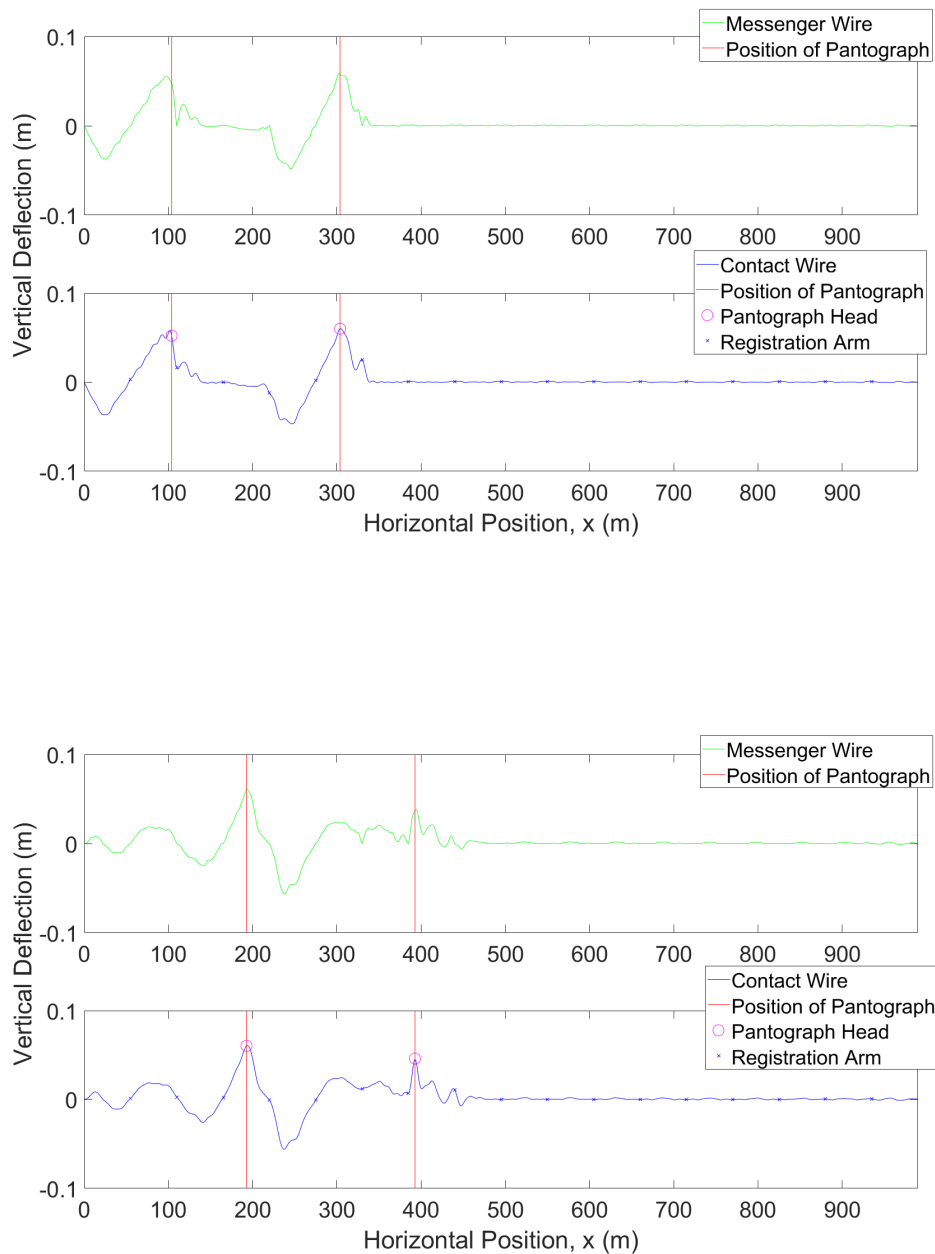


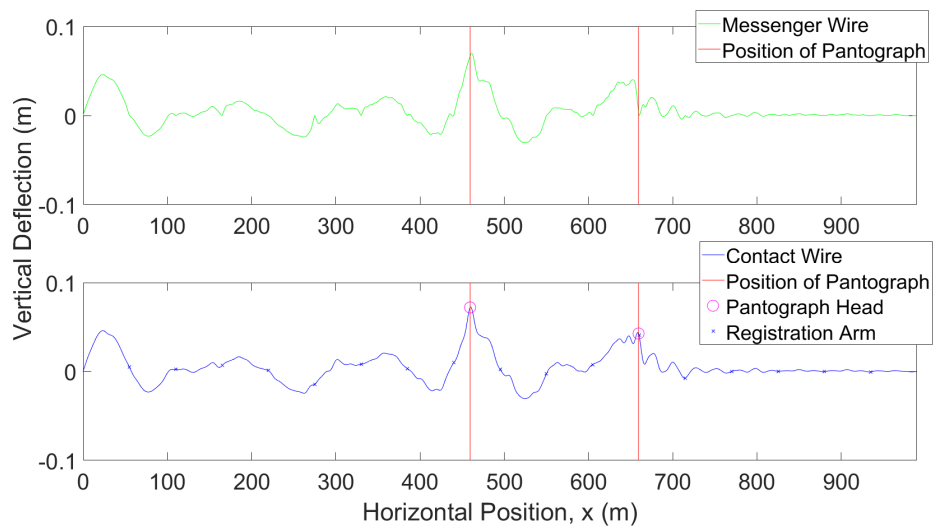
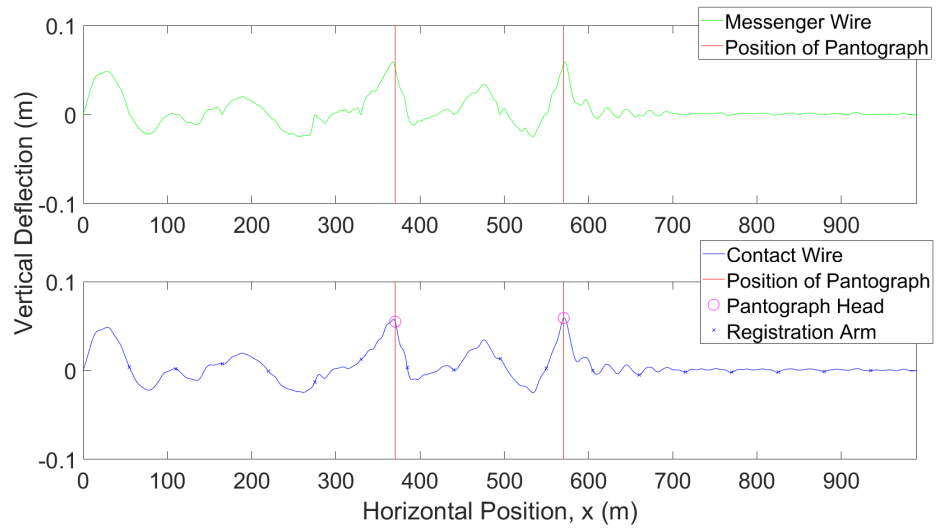
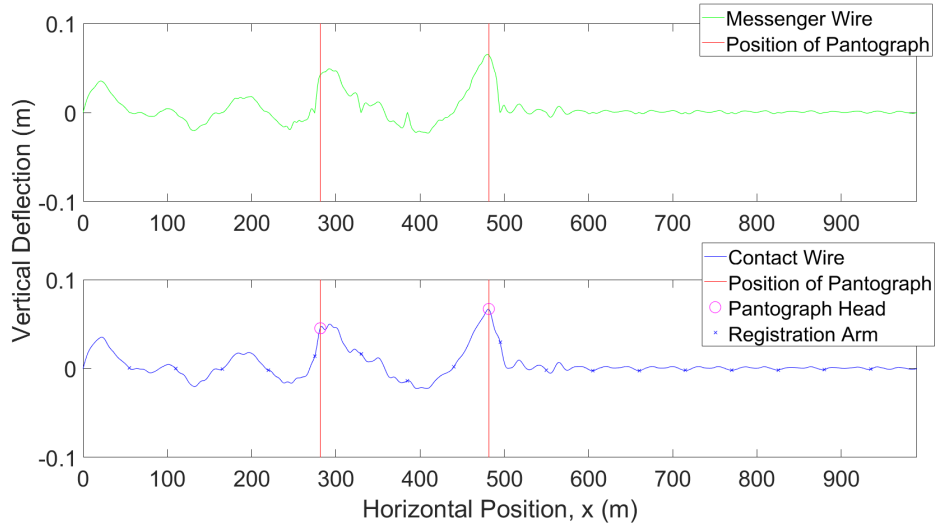


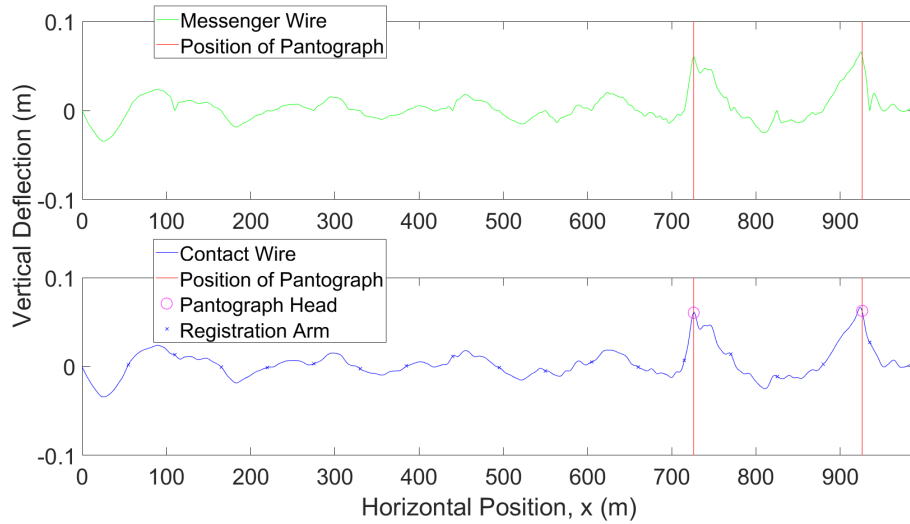
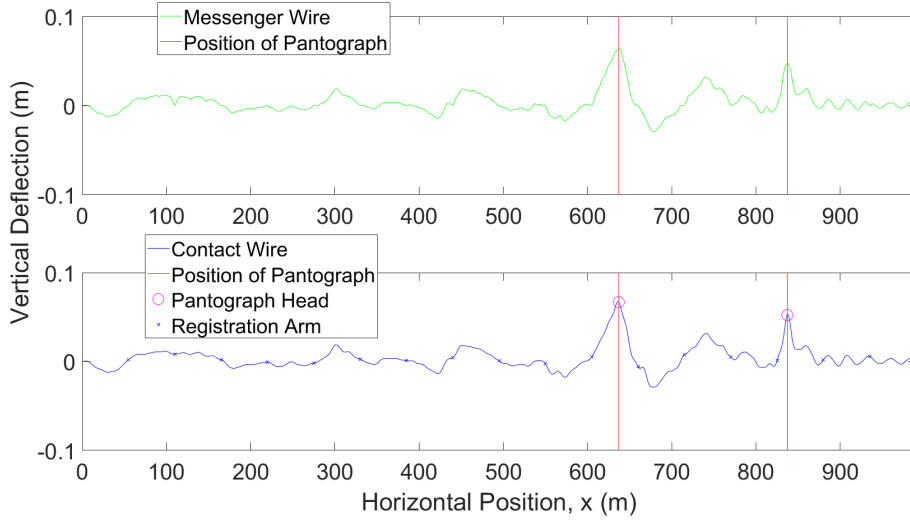
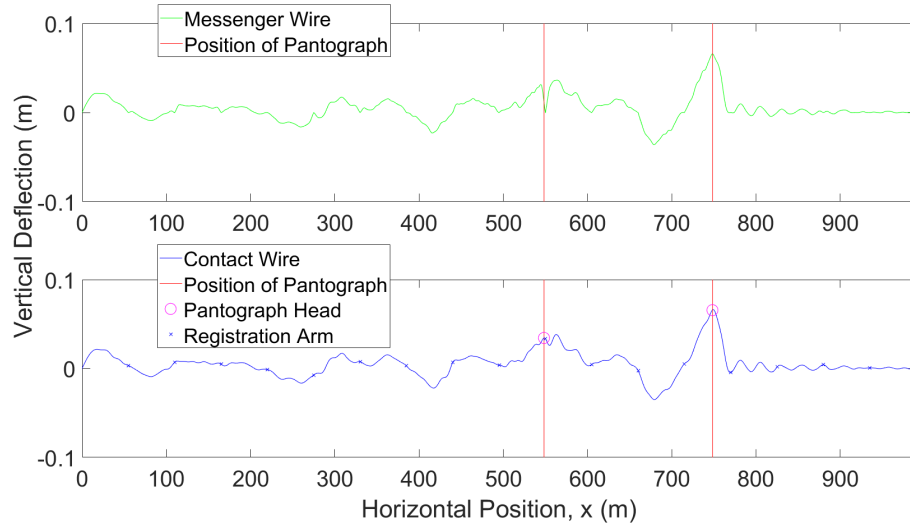


It can be seen that the wave formed in the contact wire by the front pantograph affects the interaction between the rear pantograph and the wire. This effect is a strong function of both train speed and pantograph separation. At the lower speed, the range of oscillation of the rear pantograph is greater than that of the front pantograph, because of the influence of the trailing wave on the rear pantograph.

Dynamic Deflections at 320 km/hour







At the higher speed, the trailing wave has the opposite effect: the range of oscillation is smaller for the back pantograph than the front. Furthermore, the oscillations left in the overhead wires after the train has passed by are smaller in magnitude for the higher speed than the lower speed.

It was found that dropper unloading was rare and had minimal effect on the requested results. At the lower speed, no dropper unloading occurred. At the higher speed, droppers only became unloaded momentarily as the pantograph passed underneath them and no more than one dropper was ever unloaded simultaneously. Dropper unloading was more common for the front pantograph than the rear pantograph and mostly occurred close to the registration arms.

When a dropper becomes unloaded, it stops contributing to the catenary system's stiffness. The system's overall stiffness comes from the 162 droppers, the 17 registration arms, the messenger supports and the two wires, so a single dropper's stiffness is a very small part of the whole system. The unloading of a single dropper does not have a significant effect on the global modes, but it does affect the catenary behaviour close to the dropper.

The Galerkin approach is not the best method for realistically modelling small-scale effects close to the point of contact. This could be achieved, but it would require a large increase in the number of contact-wire modes included before diagonalisation. For instance, in order to realistically reproduce effects on a 100mm scale, modes with half wavelengths at least as short as 100mm should be included, so at least 9,900 modes would have to be included. This is far more than the 210 contact-wire modes included here, so the Galerkin approach's advantage in simulation speed would be lost.

4.3.2 Contact-Force Plots

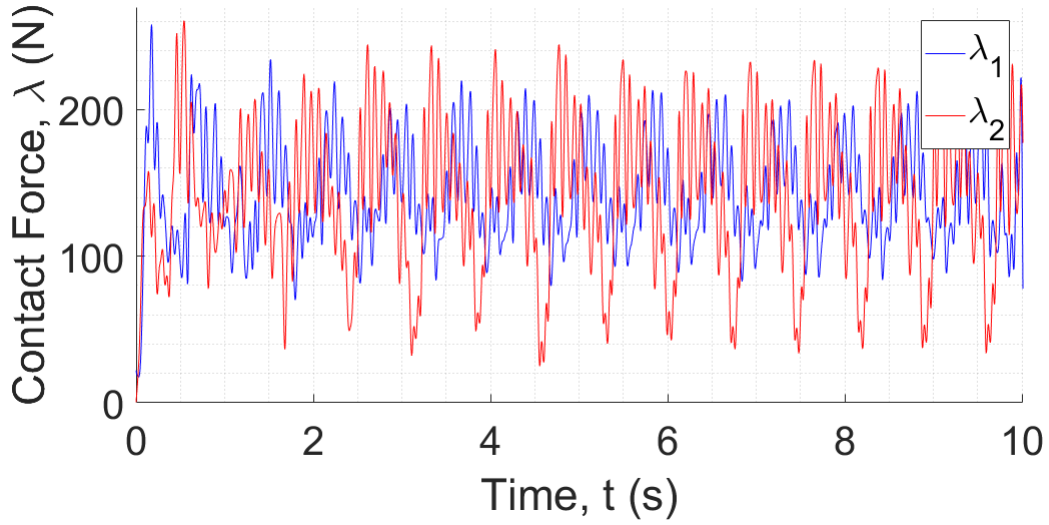


Figure 4.3: Plot of contact forces against time for BS:EN 50318:2018 at 275 km/hour

As before, it can be seen that the contact forces are almost periodic due to the uniform layout of droppers and registration arms. The contact forces for the two pantographs are out of phase, because the pantograph separation, 200m, is not divisible by the span length, 55m. The phase difference is constant because the pantograph separation is constant.

The variance of the contact force for the rear pantograph is much greater than the variance for the front pantograph. This is because the front pantograph perturbs the contact wire before the rear pantograph passes through, so the force profile of the rear pantograph, $\lambda_2(t)$, is dependent on the pantograph separation and train speed.

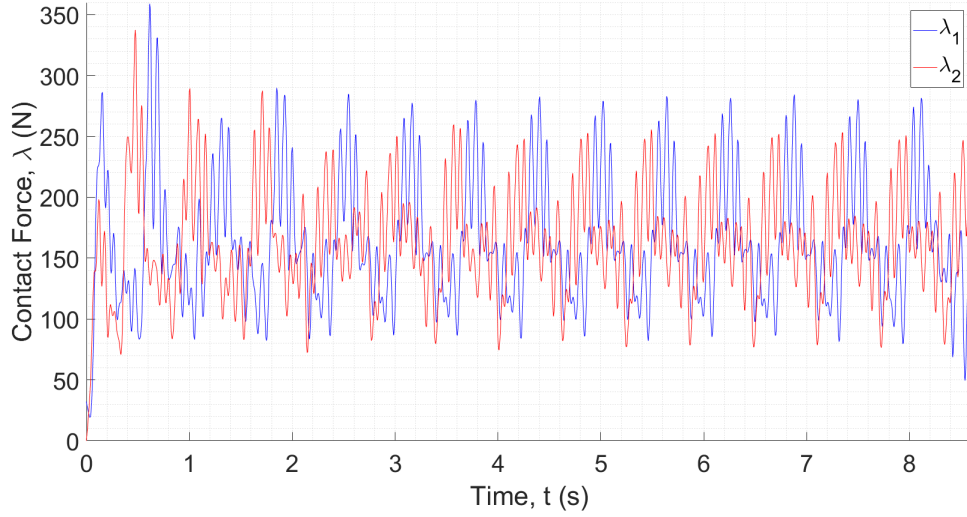


Figure 4.4: Plot of contact forces against time for BS:EN 50318:2018 at 320 km/hour

At 320 km/hour, the variance is smaller for the rear pantograph than the front. This, again, is due to the pantograph separation, train speed and catenary dynamics, which determine the effect that the front pantograph has on the rear pantograph. These findings are all in agreement with the benchmark in [22], which formed the results required by the 2018 European Standard.

For both train speeds, the load pattern initially includes a transient response, which takes about one second to decay. After this transient has decayed, the load pattern becomes almost periodic.

4.3.3 Comparison to Required Results

The analysis section started at the beginning of the sixth messenger span and ended at the end of the fifteenth. If the analysis section were brought closer to the start of the contact wire, then the front pantograph would reach the analysis section before the transient component of its contact force had sufficiently decayed. However, the simulation ends when the front pantograph is 10m from the end of the 990m contact wire. The rear pantograph is 200m behind, which means it is 780m from the start of the wire. This is 45m before the end of the analysis section, so the rear pantograph's contact force is only measured for the first 505m of the 550m analysis section.

275 km/hour	Required		Obtained	
	Pan 1	Pan 2	Pan 1	Pan 2
Mean contact force (N)	137-146	138-147	143.33	143.29
s.d. of contact force: 0-20Hz (N)	31.9-34.8	50.0-54.5	32.59	51.70
s.d. of contact force: 0-5Hz (N)	25.6-28.9	41.2-45.4	26.50	44.50
s.d. of contact force: 5-20Hz (N)	16.2-23.1	25.2-34.7	18.97	26.32
Maximum of contact force (N)	211-244	241-290	235.07	244.84
Minimum of contact force (N)	71-86	14-50	72.52	25.32
Contact-point displacement range (mm)	38-49	53-70	43.18	68.97
Maximum uplift at support (mm)	37-54		53.22	
Percentage loss of contact (%)	0	0	0.00	0.00
Damping factor	-		8.5×10^{-3}	

Table 4.1: Table of 275 km/hour results for validation against BS:EN 50318:2018

320 km/hour	Required		Obtained	
	Pan 1	Pan 2	Pan 1	Pan 2
Mean contact force (N)	150-173	158.5-172.5	164.93	164.55
s.d. of contact force: 0-20Hz (N)	49-63	30-44	49.96	42.19
s.d. of contact force: 0-5Hz (N)	38-44	14-23	40.62	29.45
s.d. of contact force: 5-20Hz (N)	29-46	25-38	29.09	30.22
Maximum of contact force (N)	280-343	247-317	336.16	264.96
Minimum of contact force (N)	50-82	21-86	77.48	62.10
Contact-point displacement range (mm)	39-51	18-35	50.46	31.10
Maximum uplift at support (mm)	52-64		62.01	
Percentage loss of contact (%)	0	0	0.00	0.00
Damping factor	-		0.016	

Table 4.2: Table of 320 km/hour results for validation against BS:EN 50318:2018

At 275 km/hour, every result is in the required range. At 320 km/hour, the standard deviation of the contact force between 0Hz and 5Hz for the rear pantograph is 28% higher than the upper bound. However, it is stated in [22] that the dispersal of indicator values used to generate the required ranges was particularly high for the rear pantograph at 320 km/hour. Therefore, the higher value presented here is believable.

The damping factors used here are much smaller than the damping factors used in the previous chapter. It is likely that less damping is needed in the overhead wires because damping is now included in the messenger-wire supports.

4.3.4 Simulation Speed

Train speed (km/hour)	275	320
Pre-processing (s)	1.47	1.11
Simulation time (s)	173	91
Post-processing (s)	0.27	0.25
Real time (s)	10.01	8.60

Table 4.3: Table of simulation speeds for BS:EN 50318:2018

These simulation times are more than one order of magnitude longer than those for the 2002 European Standard, but this is still much faster than FEM software. The main reasons for the loss of speed are the inclusion of the second pantograph and the increased number of eigenmodes included due to the long contact wire: 481 modes at 275 km/hour and 398 modes at 320 km/hour, as opposed to 161 modes at both speeds for the 2002 European Standard.

The number of eigenmodes was initially chosen to be 481 for both train speeds, using a cut-off eigenvalue magnitude of 2×10^4 , but it was found that the number of modes could be reduced for the higher speed, achieving a faster simulation time without significantly affecting the results. The 481st mode has a natural frequency of 22.4Hz, which is higher than both the pantograph's frequency cut-off (13.6Hz) and the rate at which the pantograph encounters droppers at the higher speed (16.2Hz). Therefore, the number of eigenmodes is high enough to realistically reproduce the pantograph dynamics at both train speeds. The 398th mode has a natural frequency of 16.4Hz, which is just high enough to reproduce these effects. However, some of the results for the lower train speed with 398 modes fell outside the required ranges, so the number of modes was left as 481.

4.4 Conclusions

The model proved to be realistic, with only a single result falling outside its required range. The simulation speed was decreased by the addition of a second pantograph and the larger number of eigenmodes included because of the longer contact wire, but was still fast in comparison to FEM software. It was shown that the Galerkin approach could be

used to model multiple pantographs in contact with one wire and that dropper unloading could also be included. However, the transition from one contact wire to the next was not modelled and this is required in order to model larger OLE configurations with multiple contact wires.

Chapter 5

Contact Events

5.1 Introduction

Previously, there was no loss of contact between the pantograph head and the contact wire. When modelling contact-wire transitions or testing poorly designed catenary systems, this is not true. When there is loss of contact, the model must detect contact events, when the pantograph comes into or out of contact with the wire, and update the states and equations accordingly. This is explained in [48].

In this chapter, the process of modelling events is described. The conditions used to detect events are explained and a simplified version is given, which greatly improves speed at the cost of slightly reduced realism. Impact modelling is used to determine the new states whenever the pantograph comes into contact with a wire, but not when the pantograph comes out of contact. The specifics of implementing events in Simulink are explained in detail. The events modelling is demonstrated using three identical BS:EN 50318:2018 catenary sections and the results are compared to those from the previous chapter. Finally, conclusions are drawn about the performance and the relative merits of the simplified and full events models are discussed.

5.2 Detection of Events

5.2.1 A Pantograph Comes Into Contact

When the pantograph is not in contact with the contact wire, the model must check for an into-contact event. This occurs as the pantograph physically comes into contact with the wire, when the height of the pantograph head is equal to the contact-wire deflection at that position.

$$z_3(t) + \bar{z}_3 - \sin \left(\tilde{\beta} x_p(t) \right)^T V \tilde{q}(t) - \sin \left(\bar{\beta} x_p(t) \right)^T \bar{q} = 0 \quad (5.1)$$

5.2.2 A Pantograph Comes Out of Contact

When the pantograph is in contact with the contact wire, the model must check for a loss-of-contact event. This occurs when the contact force falls to zero.

$$\lambda(t) = 0 \quad (5.2)$$

5.2.3 Simplified Events

Previously, either full-complexity events or no events have been included. The full events model checks for contact events at every time step, whereas the no-events model assumes that all pantographs remain in contact with all wires at all times.

For some simulations, detailed events modelling is not required and the model can be simplified in order to increase simulation speed. This is done by searching for only two events per pantograph per contact-wire transition:

1. The pantograph comes into contact with the new contact wire. This is detected using (5.1).
2. The pantograph comes out of contact with the old contact wire. This is detected using (5.2).

This simplification prevents the pantograph from bouncing between the two wires, which can result in excessive contact events that have little effect on the overall results. It also means that once the pantograph has lost contact with the old wire, the model does not need to check for events until the pantograph reaches the end of the new contact wire and must transition again.

After simulation, the logs of contact force, pantograph-head deflection and wire deflections can be used to determine whether events should have been detected. This can be used to justify or disqualify the use of the simplified events model. However, the simulation software cannot currently switch dynamically between events models: if the simplified model is found to be insufficient, then the simulation must be rerun with the full events model.

5.3 Impact Modelling

The following analysis considers a single pantograph interacting with two overlapping contact wires. For simulations involving multiple pantographs, each pantograph is considered separately and the analysis is identical.

When the pantograph comes into contact with a wire, care must be taken to ensure that the new initial conditions satisfy the velocity constraint. This is because there is incongruence between the velocity of the pantograph head and that of the wire immediately before the contact event. This is not a problem for loss-of-contact events, where there is no such velocity mismatch.

$$\begin{aligned}
\Delta \dot{z}_3(t) &= \sin \left(\tilde{\beta} x_{p,1}(t) \right)^T V \Delta \dot{\underline{q}}_1(t) - \left(\dot{z}_3(t) - \sin \left(\tilde{\beta} x_{p,1}(t) \right)^T V \dot{\underline{q}}_1(t) \right. \\
&\quad \left. - \left(\left(\tilde{\beta} v_p(t) \right) .* \cos \left(\tilde{\beta} x_{p,1}(t) \right) \right)^T V \tilde{\underline{q}}_1(t) - \left(\left(\tilde{\beta} v_p(t) \right) .* \cos \left(\tilde{\beta} x_{p,1}(t) \right) \right)^T \tilde{\underline{q}}_1(t) \right) \\
&= \sin \left(\tilde{\beta} x_{p,1}(t) \right)^T V \Delta \dot{\underline{q}}_1(t) - k_v(t),
\end{aligned} \tag{5.3}$$

where k_v represents the current, violated velocity constraint (the difference in velocity

between the pantograph and contact wire at the point of contact) and $x_{p,1}(t)$ is the position of the pantograph in Contact Wire 1's coordinate system.

Momentum must be conserved, as shown in (5.4). The term in the curly brackets is included if the pantograph was already in contact with Contact Wire 2 and is coming into contact with Contact Wire 1. If the pantograph was in contact with neither wire, then this term is omitted.

$$m_3 \Delta \dot{z}_3(t) + \rho A \int_0^L \Delta \dot{w}_1(x, t) dx + \left\{ \rho A \int_0^L \Delta \dot{w}_2(x, t) dx \right\} = 0 \quad (5.4)$$

where $\dot{w}(x, t) = \sin(\underline{\tilde{\beta}}x) \dot{\underline{q}}(t)$.

As the system of equations is underdetermined, the shape of $\Delta \dot{w}_i(x, t)$ must be prescribed for each wire. This was approximated as a Dirac Delta function centred at $x_{p,i}(t)$ and an orthogonality integral was used to find $\Delta \dot{\underline{q}}_i(t)$. It is important to note that the peak of this Delta-function approximation is finite, because it was constructed from a finite number of sine terms.

$$\Delta \dot{w}_i(x, t) = \sin(\underline{\tilde{\beta}}x)^T V \Delta \dot{\underline{q}}_i(t) = k_{w,i}(t) \delta(x - x_{p,i}(t)) \quad i = 1, 2 \quad (5.5)$$

$$\Delta \dot{w}_2(x_p^b, t) = \{\Delta \dot{z}_3(t)\} \quad (5.6)$$

(5.3)-(5.6) were used to evaluate $\Delta \dot{z}_3(t)$, $\Delta \dot{\underline{q}}_1(t)$, $\Delta \dot{\underline{q}}_2(t)$ and $k_{w,i}(t)$.

$$k_{w,1}(t) = \frac{k_v(t)}{\frac{\rho A k_{A,1}(t)}{m_3 + \left\{ \frac{\rho A L k_{A,2}(t)}{2 \sin(\underline{\tilde{\beta}}x_{p,2}(t))^T V W \sin(\underline{\tilde{\beta}}x_{p,2}(t)) \right\}} + \frac{2}{L} \sin(\underline{\tilde{\beta}}x_{p,1}(t))^T V W \sin(\underline{\tilde{\beta}}x_{p,1}(t))} \quad (5.7)$$

$$\Delta \dot{z}_3(t) = \frac{2k_{w,1}(t)}{L} \sin(\underline{\tilde{\beta}}x_{p,1}(t))^T V W \sin(\underline{\tilde{\beta}}x_{p,1}(t)) - k_v(t) \quad (5.8)$$

$$k_{w,2}(t) = \left\{ \frac{\Delta \dot{z}_3(t)}{\sin(\underline{\tilde{\beta}}x_{p,2}(t))^T V W \sin(\underline{\tilde{\beta}}x_{p,2}(t))} \right\} \quad (5.9)$$

$$\Delta \dot{\underline{q}}_i(t) = \frac{2k_{w,i}(t)}{L} W \sin \left(\underline{\tilde{\beta}} x_{p,i}(t) \right) \quad i = 1, 2 \quad (5.10)$$

$$\begin{aligned} k_{A,i}(t) &= \frac{2}{L} \int_0^L \sin \left(\underline{\tilde{\beta}} x \right)^T dx V W \sin \left(\underline{\tilde{\beta}} x_{p,i}(t) \right) \\ &= \frac{2}{L} \left(\begin{pmatrix} 1./\underline{\beta} \\ \underline{0} \end{pmatrix} \cdot * (\underline{1} - (-1).^N) \right)^T V W \sin \left(\underline{\tilde{\beta}} x_{p,i}(t) \right) \end{aligned} \quad (5.11)$$

$$N = \begin{pmatrix} 1 \\ 2 \\ \vdots \\ N_q \end{pmatrix} \quad (5.12)$$

These terms were used to calculate the correct initial conditions after every into-contact event. When a pantograph came out of contact with a wire, impact modelling was not used and the velocities were left unchanged.

5.4 Simulink Implementation

5.4.1 Contact Conditions

With two pantographs, there are four possible contact conditions for each wire:

1. Neither pantograph in contact.
2. Front pantograph in contact; rear pantograph out of contact.
3. Rear pantograph in contact; front pantograph out of contact.
4. Both pantographs in contact.

If neither pantograph is in contact with the wire, then no contact force is applied and no variables are eliminated. The equations are simplified by removing all $\lambda(t)$ -terms.

If only one pantograph is in contact, then the equations for Chapter 3 are used. In the contact constraints, $x_p(t)$ and $z_3(t)$ are evaluated for the in-contact pantograph. No contact force is exerted on the out-of-contact pantograph.

If both pantographs are in contact, then the equations for Chapter 4 are used.

The contact conditions were evaluated separately for each wire, because overlapping wires are coupled only through the $\ddot{z}_3(t)$ -equation. Whenever a contact event occurred, the new contact conditions were used to choose the correct set of equations for each contact wire.

Triggered Subsystems

A triggered subsystem is a Simulink block which evaluates its output only when an edge is detected from a certain input. This input is known as a trigger signal. After the output has been evaluated, the subsystem holds this output until the next event occurs.

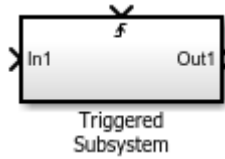


Figure 5.1: A triggered subsystem in Simulink

The event-detection equations (5.1)-(5.2) were used to form trigger signals, which became positive only when an event occurred. Triggered subsystems monitored the trigger signals for rising edges and were used to create a 2×1 binary vector for each wire that denoted the contact conditions.

The trigger signals were additionally used to reset all of the integrators in the model. Whenever an event occurred, each integrator was restarted with the correct initial conditions. These initial conditions were calculated continuously.

Enabled Subsystems

An enabled subsystem is similar to a triggered subsystem insofar as it takes a control signal as an auxiliary input. However, an enabled subsystem produces a continuous output

whenever its control input is positive. When the control input is nonpositive, the subsystem does not execute and its last output is held.

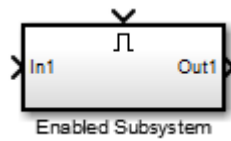


Figure 5.2: An enabled subsystem in Simulink

Four enabled subsystems were used for each contact wire: one for each possible contact condition. The enabled subsystem corresponding to the current contact condition was used to produce the correct set of equations, while the outputs from the other three subsystems were ignored.

5.4.2 Avoidance of Algebraic Loops

An algebraic loop exists in Simulink if and only if there is a closed signal loop containing only direct-feedthrough blocks. A direct-feedthrough block requires only its input at the current time step to determine its output. Simulink requires all signals to be in agreement, so an algebraic loop creates circular dependencies and is typically highly undesirable.

The use of the state accelerations, $\underline{w}(t)$, to calculate the trigger signals and contact forces creates an algebraic loop, as these signals do not pass through an integrator. To break this loop, a small time delay (one millisecond) was used.

Due to the time delay, events were detected after they occurred. Therefore, it was necessary to rewind the states to their values at the time of the event by applying the time delay to each trigger signal and each signal used to set new initial conditions. This way, the whole system was rewound by one time delay.

If an event was detected less than one time delay after a previous event, then the states that caused this event were erroneous states waiting to be rewound and the event was not legitimate. Therefore, events were disallowed for one time delay after an event had been detected. The erroneous states were removed from the results in post-processing.

5.4.3 New-Wire Events

In addition to contact events, new-wire events had to be detected. The model only included two contact wires at any given time, so new wires had to be brought in dynamically. Whenever the front pantograph reached the start of a new wire, this new wire was brought into the model and the back wire was removed. The previously described events procedure was used and the new initial conditions were chosen such that the old front wire became the new back wire.

5.5 Results

The events modelling was applied to the 2018 European Standard, with the same damping factor and uplift forces as in the previous chapter. ode45 was used again, with the same settings as in the previous chapter. The full events model was used to generate all of the plots, but simplified events were also tested and the results are compared in Section 5.5.3.

For these simulations, three of the 990m catenary sections from the previous chapter were used. The first section allowed the transient component of each pantograph's contact force to decay before the pantograph reached the analysis section. The second catenary section included the analysis section, which was used to measure properties of the contact-force profile for each pantograph. The third section allowed the front pantograph to continue past the end of the second contact wire while the rear pantograph reached the end of the analysis section.

The numbers of modes used for each catenary section were the same as in the previous chapter. The model included two pantographs, with the same three-mass model and 200m separation as in the previous chapter.

5.5.1 Snapshots

In the following snapshots, the steady-state deflections have been included and the overall deflection is shown. This allows the overlap between adjacent catenary systems to be shown clearly, which is especially important when studying the the transition of a panto-

graph from one contact wire to the next.

275 km/hour

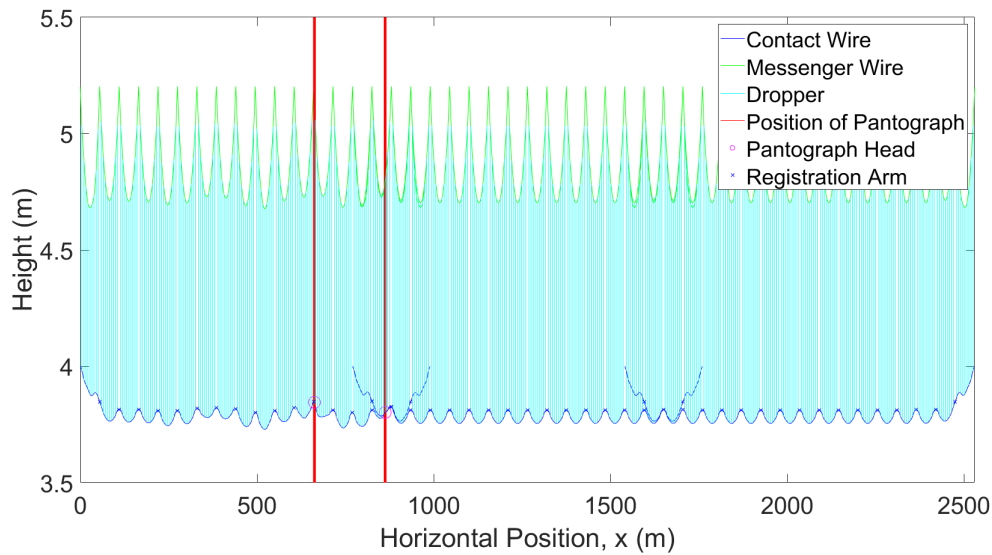


Figure 5.3: Snapshot 1 of vertical wire deflections at 275 km/hour with events

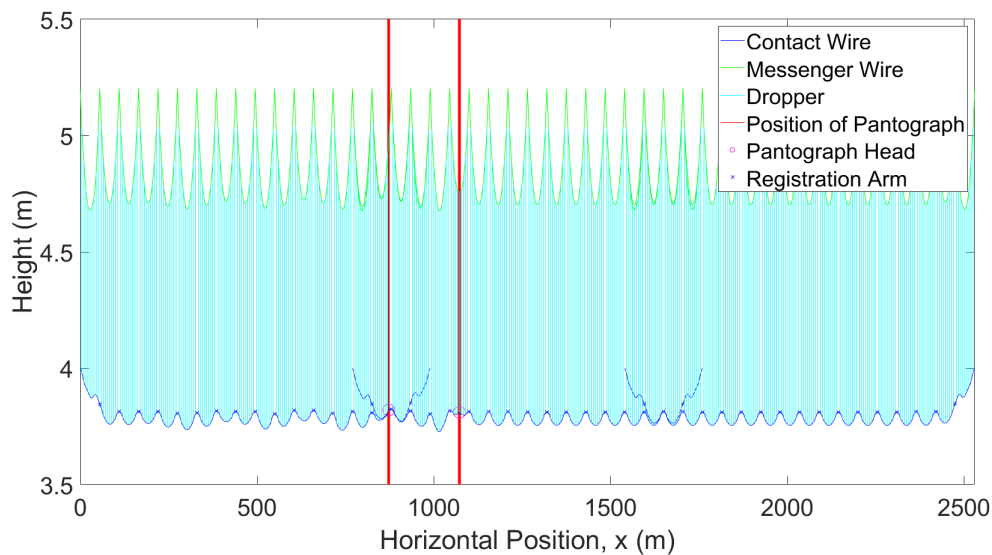


Figure 5.4: Snapshot 2 of vertical wire deflections at 275 km/hour with events

Figure 5.3 and Figure 5.4 show the pantographs transitioning from the first contact wire to the second at 275 km/hour. The magenta circles in the horizontal plots are included only for pantograph-wire combinations that are in contact. Two circles for the same pantograph indicate that it is currently in contact with both of the overlapping contact wires.

The overlap was chosen to be 220m, in order to achieve a smooth transition from one wire to the next. Since the overlap was exactly four messenger spans long, the droppers of adjacent catenary sections in the transition span were aligned exactly and the two sagging wires were almost exactly parallel in steady state. Each contact wire had a 55m fly-in span at the start and a symmetrical 55m fly-out span at the end, where the wire gently descended 200mm from its fixed supports. This arrangement was chosen both to be realistic and to make the transition of a pantograph from one contact wire to the next as smooth as possible. Real-world transition spans are designed very similarly, because it is important to ensure smooth transitions.

320 km/hour

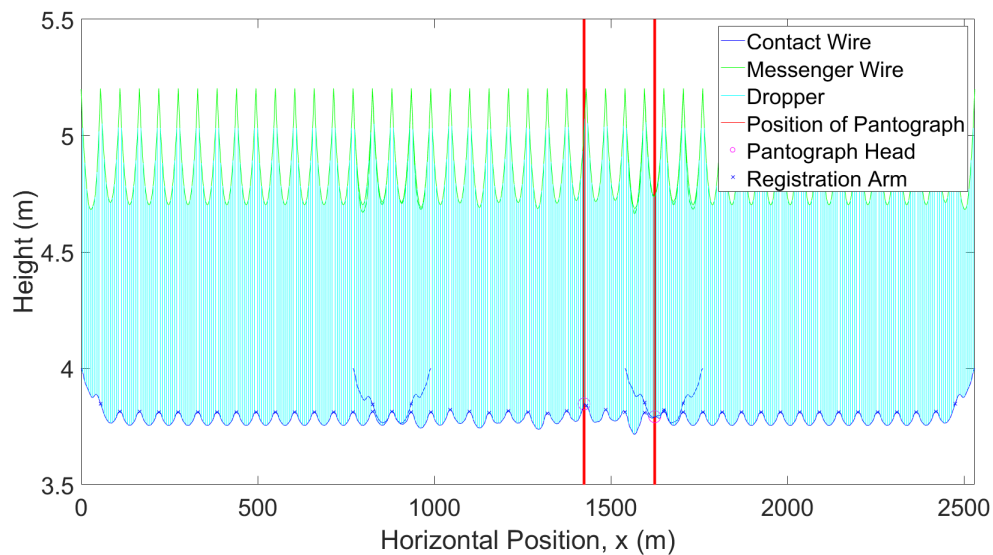


Figure 5.5: Snapshot 1 of vertical and wire deflections at 320 km/hour with events

Figure 5.5 and Figure 5.6 show the pantographs transitioning from the second contact wire to the third at 320 km/hour. This transition was also very smooth, with no missed events and no major contact-wire bounce.

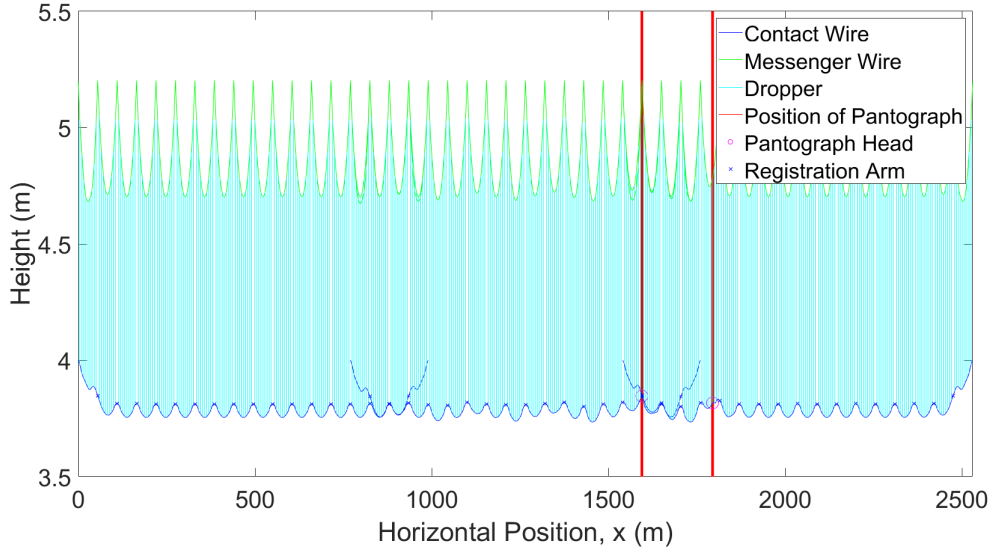


Figure 5.6: Snapshot 2 of vertical wire deflections at 320 km/hour with events

5.5.2 Contact-Force Plots

In the following plots, $\lambda_{i,j}(t)$ is the contact force between the i^{th} contact wire and the j^{th} pantograph. The train was started from rest and accelerated to its final speed in 2.5s, which is the reason for the early distortion in the contact-force oscillations.

First Contact Wire

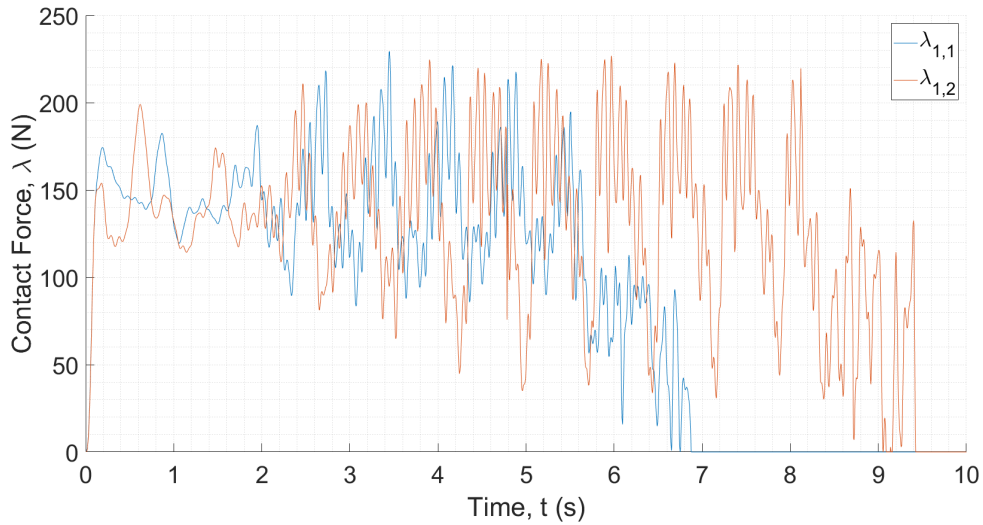


Figure 5.7: Plot of contact forces against time for the first wire at 275 km/hour with events

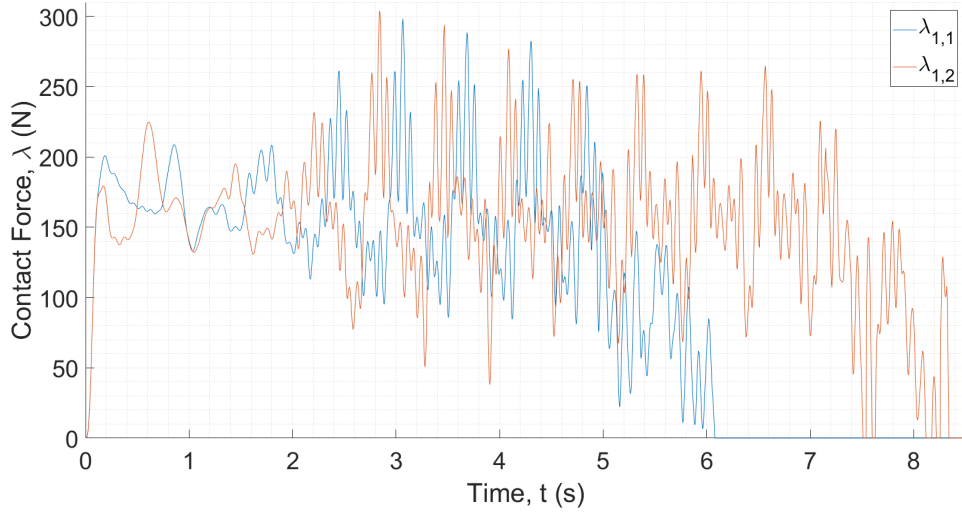


Figure 5.8: Plot of contact forces against time for the first wire at 320 km/hour with events

Figure 5.7 and Figure 5.8 show the time evolution of the contact force between the first contact wire and each pantograph. The front pantograph comes out of contact first, after coming into contact with the second wire. About two seconds later, the rear pantograph also leaves contact with the first contact wire.

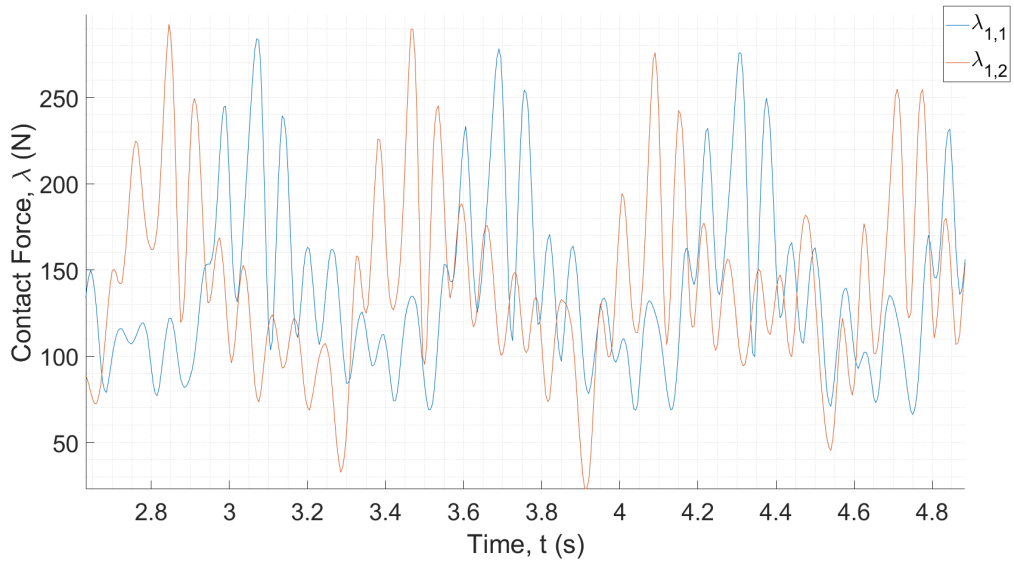


Figure 5.9: Zoomed-in plot of contact forces against time for the first wire at 320 km/hour with events

Both pantographs' forces oscillate at the same frequency, but they are out of phase. These oscillations are caused by the arrangement of droppers, registration arms and messenger supports. The amplitude of contact-force oscillations of the rear pantograph is

substantially larger than that of the front pantograph, due to the trailing wave created in the contact by the front pantograph. Similar results were observed at 275 km/hour.

Second Contact Wire

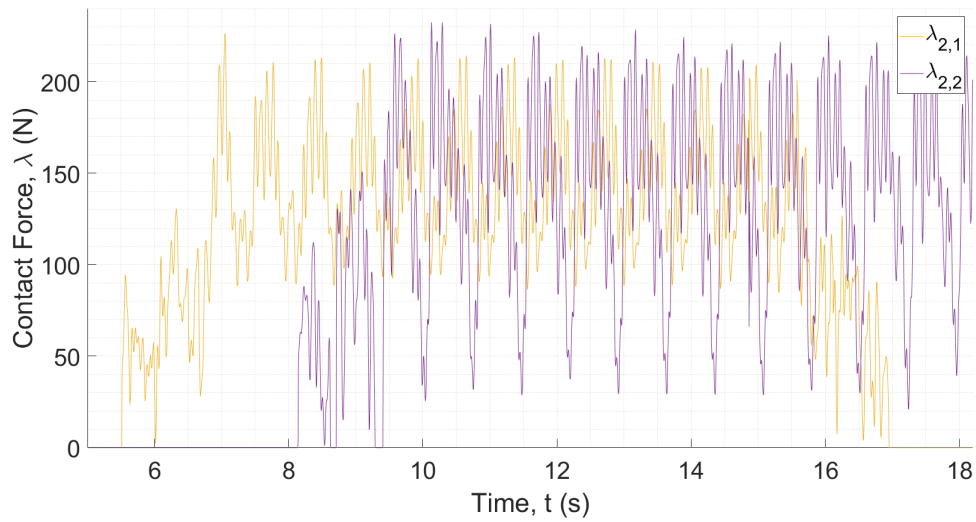


Figure 5.10: Plot of contact forces against time for the second wire at 275 km/hour with events

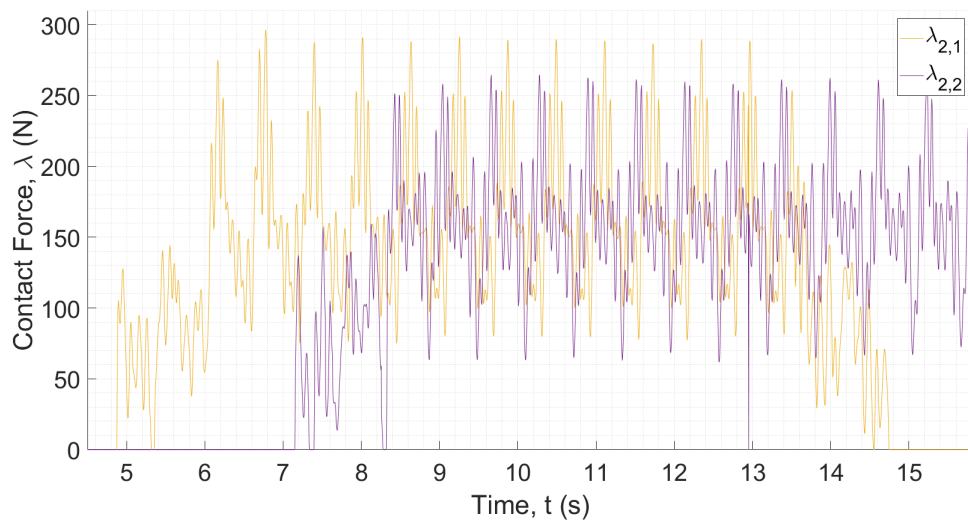


Figure 5.11: Plot of contact forces against time for the second wire at 320 km/hour with events

Figure 5.10 and Figure 5.11 show the time evolution of the contact force between the second contact wire and each pantograph. It can be seen that the peak contact force for

each pantograph is barely affected by the transition, because the transfer of contact was very smooth.

The drop in contact force for the second pantograph plotted at 13s was due to the rearrangement of matrices as the third contact wire was brought into the Simulink model. This was caused by the plotting code and the contact force did not really drop to zero.

Pantographs

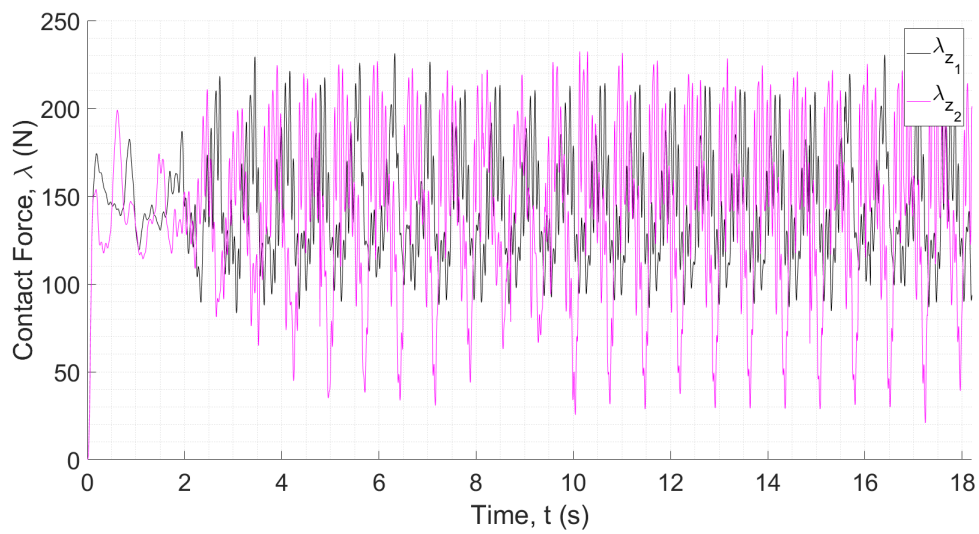


Figure 5.12: Plot of contact forces against time for the pantographs at 275 km/hour with events

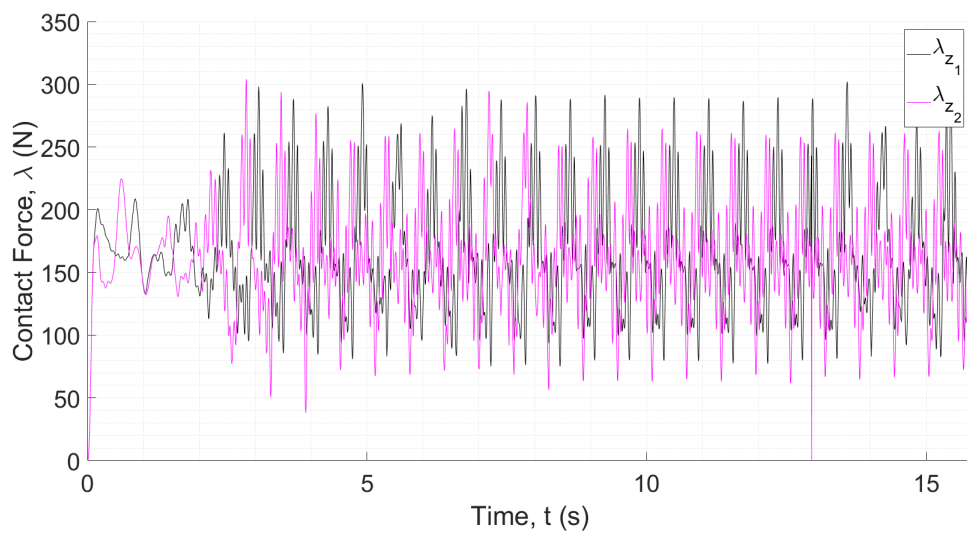


Figure 5.13: Plot of contact forces against time for the pantographs at 320 km/hour with events

Figure 5.12 and Figure 5.13 show the total force exerted on each pantograph by the contact wires. It can be seen that throughout each transition, the contact force is split between the two wires such that the total force is very similar to the force for a single wire.

When the overlap is changed such that the overlap length is not a multiple of the messenger-span length and the droppers of the two catenary systems are not aligned, the transition is far less smooth. The range of total contact force on the pantograph head through the transition span is greater and the transient contact-force profile that is caused by the transition and remains after the transition is complete is greater in amplitude. Furthermore, for some configurations, the pantograph bounces in and out of contact with a contact wire multiple times. These effects are realistic for a poorly designed overlap and show the importance of proper transition-span design.

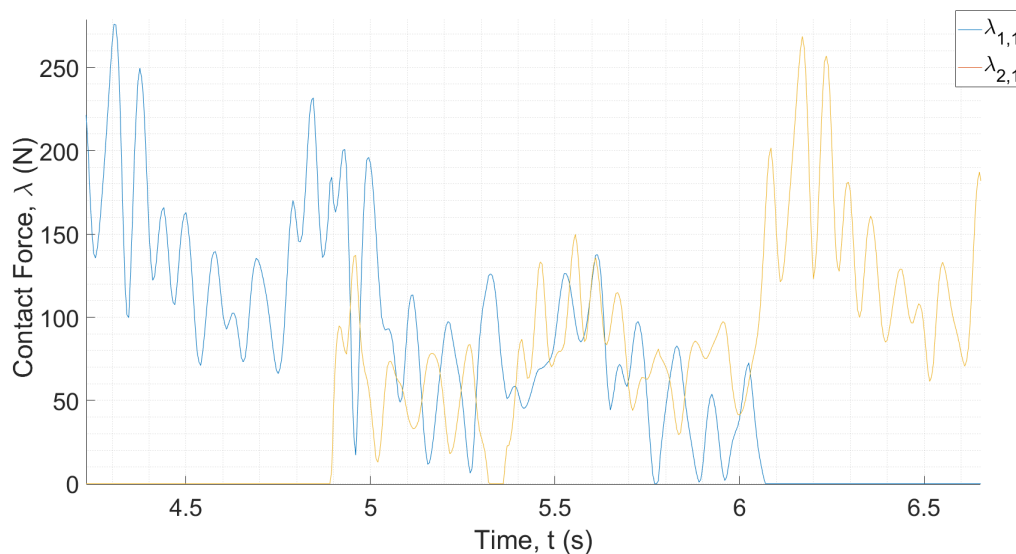


Figure 5.14: Plot of contact forces against time for the front pantograph as it transitions from the first wire to the second at 320 km/hour

Between five and six seconds in Figure 5.14, both pantographs are in contact with the first contact wire. It is clear that the two contact forces vary independently and should be calculated separately, as they have been here. The difference in contact force between the two pantographs is especially large at the time of a contact-wire transition. The calculation of individual contact forces is one of the main achievements of the software presented here, as many existing simulations unrealistically split the force 50:50 between the wires.

All Contact Wires and Pantographs

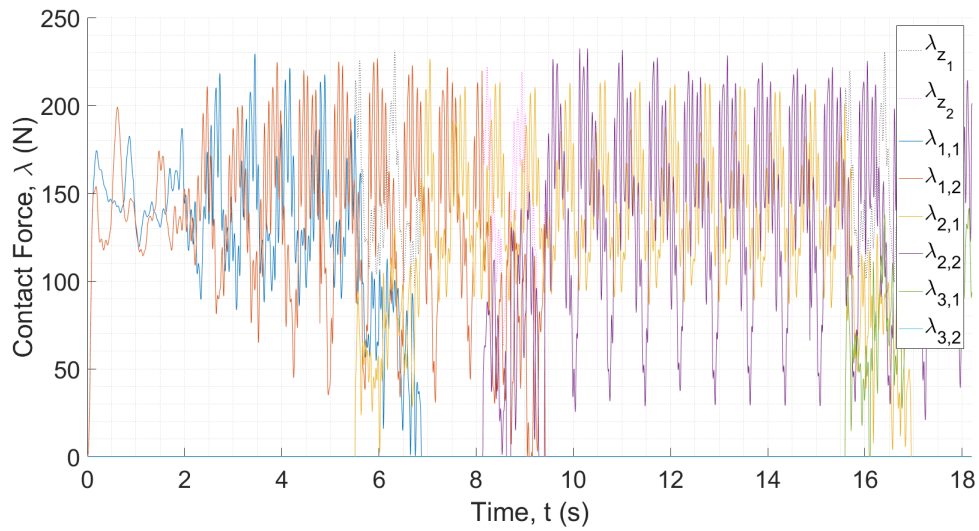


Figure 5.15: Plot of contact forces against time for all wires and pantographs at 275 km/hour with events

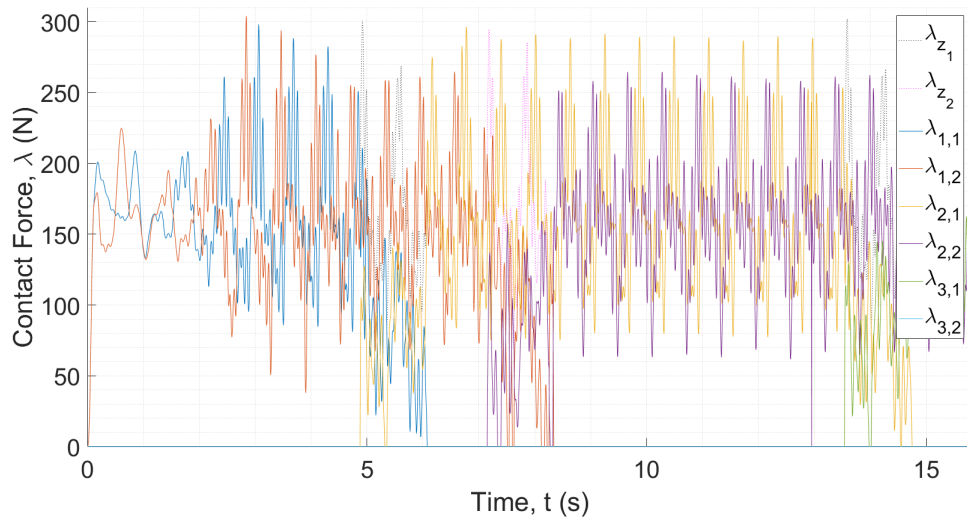


Figure 5.16: Plot of contact forces against time for all wires and pantographs at 320 km/hour with events

Figure 5.15 and Figure 5.16 show the contact forces for all three contact wires and both pantographs. These graphs are somewhat difficult to interpret, but are intended to give an overall picture of the simulation results.

5.5.3 Comparison of Results

275 km/hour	Without events		With full events		With simplified events	
	Pan 1	Pan 2	Pan 1	Pan 2	Pan 1	Pan 2
Mean contact force (N)	143.33	143.28	143.53	140.42	143.51	140.34
s.d. of contact force: 0-20Hz (N)	32.71	51.87	31.27	50.88	31.42	50.86
s.d. of contact force: 0-5Hz (N)	26.51	44.51	26.15	44.12	26.26	44.12
s.d. of contact force: 5-20Hz (N)	19.16	26.62	17.14	25.34	17.25	25.30
Maximum of contact force (N)	235.70	244.96	216.22	229.58	218.71	229.20
Minimum of contact force (N)	72.29	24.92	85.61	17.87	86.15	18.93
Contact-point displacement range (mm)	43.17	68.98	38.34	62.91	38.16	62.12
Maximum uplift at support (mm)	53.27		42.78		43.74	
Percentage loss of contact (%)	0.00	0.00	0.00	0.00	0.00	0.00

Table 5.1: Table of 275 km/hour results for model with events

■ As required ■ Error $\leq 5\%$ ■ $5\% < \text{Error} \leq 10\%$ ■ Error $> 10\%$

The events model shows good agreement with the single-wire model. However, with events, the transients have much more time to die off before the front pantograph reaches the analysis section, hence the lower range of contact force. The damping could be reduced in order to amend the results that are not in the correct ranges, but the purpose of these simulations is to compare the results with full events, simplified events and no events.

The results for simplified events are almost identical to those for full events, but the simulation speed was substantially improved by this simplification. This suggests that simplified events should be used when the results for the transition sections are not of interest.

320 km/hour	Without events		With full events		With simplified events	
	Pan 1	Pan 2	Pan 1	Pan 2	Pan 1	Pan 2
Mean contact force (N)	164.09	164.57	164.21	161.66	164.22	161.60
s.d. of contact force: 0-20Hz (N)	50.17	42.54	49.12	42.75	49.12	42.75
s.d. of contact force: 0-5Hz (N)	40.62	29.47	40.73	32.08	40.78	32.14
s.d. of contact force: 5-20Hz (N)	29.46	30.68	27.46	28.27	27.38	28.91
Maximum of contact force (N)	334.53	265.80	294.51	265.00	294.93	266.71
Minimum of contact force (N)	75.99	61.24	75.86	58.92	74.85	58.41
Contact-point displacement range (mm)	50.35	31.11	45.68	29.40	44.82	28.98
Maximum uplift at support (mm)	62.09		52.38		52.14	
Percentage loss of contact (%)	0.00	0.00	0.00	0.00	0.00	0.00

Table 5.2: Table of 320 km/hour results for model with events

■ As required ■ Error $\leq 5\%$ ■ $5\% < \text{Error} \leq 10\%$ ■ Error $> 10\%$

At 320 km/hour, the same trends are shown: the lack of transients leads to reduced displacements and smaller maximum contact forces and the simplified-events results are in agreement with those for full events.

For both train speeds, most of the results fall within the ranges required by the 2018 European Standard. The parameters of this model could be tuned to improve the results further, but this is not the purpose of these simulations. These simulations are intended to be a proof of concept of the events model and to show that this model can produce realistic results that are similar to those produced by the model without events.

5.6 Simulation Speed

Train speed (km/hour)	275		
	Without events	With full events	With simplified events
Pre-processing (s)	1.47	1.44	1.44
Simulation time (s)	173	2158	1603
Post-processing (s)	0.27	4.81	3.40
Real time (s)	10.01	18.20	18.2
Relative speed	5.6×10^{-2}	8.4×10^{-3}	1.1×10^{-2}

Table 5.3: Comparison of simulation speeds with and without events at 275 km/hour

Train speed (km/hour)	320		
	Without events	With full events	With simplified events
Pre-processing (s)	1.11	1.65	1.65
Simulation time (s)	91	1450	1085
Post-processing (s)	0.25	3.25	2.34
Real time (s)	8.60	15.82	15.82
Relative speed	9.5×10^{-2}	1.1×10^{-2}	1.5×10^{-2}

Table 5.4: Comparison of simulation speeds with and without events at 320 km/hour

The relative speed shown is $\frac{\text{real time}}{\text{simulation time}}$. Adding events to the model reduces the simulation speed primarily because the solver has to check for events at all times. This means that more time steps are required in order to produce realistic results. Furthermore, the events procedure itself is time-consuming and must be carried out frequently throughout each transition section.

Despite the simplified-events model producing almost identical results to the full-events model, the improvement in simulation speed is over 30%. This can be further improved, because the simplified model was adapted from the full model and includes some unnecessary computation.

5.7 Conclusions

The instantaneous change in vertical contact-wire velocity due to impact with the pantograph head was represented by a Dirac Delta function in space, centred on the point of impact. The velocity constraint was used to ensure that the resulting change in vertical pantograph-head velocity was consistent with the change in the contact wire's velocity, while conservation of momentum was used to determine the relative changes in velocity of the pantograph and the wire.

The impact was assumed to be instantaneous, which required an infinite contact force, and the pantograph head was not allowed to deform. Furthermore, kinetic energy was not conserved. Therefore, the realism of the impact modelling could be substantially improved. However, the main goal of the impact-modelling subsystem is to ensure that the pantograph transitions smoothly from one contact wire to the next and allow the simulation to continue.

The realism of the updated model was confirmed by comparison to the results from the previous chapter. The simulation speed was found to be reduced by around 85% by full events modelling, largely due to the reduction in length of time step.

A simplified events model was proposed and the improvement in simulation speed was demonstrated. For the 2018 European Standard, the simplified events model and full events model gave almost identical results, which were in line with the benchmark. This simplified model should be used whenever the analysis section does not include any transition spans. A number of ways to further improve the simulation speed will be discussed in Section 7.2.

For a pantograph in contact with two contact wires simultaneously, the split of contact force between the two wires was studied. Many existing pieces of pantograph-catenary

simulation software assume for simplicity that half of the contact force is applied to each wire. This new software improves on this by explicitly calculating the contact force exerted on each wire. It was found that shortly after the pantograph had come into contact with a second wire, this split was far from 50:50.

Chapter 6

Validation Against Old Dalby

Test-Track Data

6.1 Introduction

In this chapter, the Simulink model is modified to simulate a real track, with many different catenary sections, as shown in Figure 6.1 and Figure 6.2. The Old Dalby test track was specifically designed to have as many different OLE set-ups and discrete components as possible, in order to test pantograph-catenary systems and simulations. The data for this track was provided by Furrer+Frey, who own the overhead equipment and had run physical tests on the track for six weeks.

The testing took place from February 17th to March 28th, 2014. A Javelin train was loaned from Hitachi and driven by employees of Southeastern. Two pantographs were provided by Brecknell Willis. Various problems were encountered, including the miscalibration of the second pantograph and unintentionally crossed contact wires, but these were eventually overcome and believable data was obtained.

6.1.1 Old Dalby Data

When the Old Dalby testing took place, data about the position of the train, the position of pantograph head and the contact force was collected. This data has been made available

and results from the Simulink model are compared to the contact-force data in this chapter. None of the data collection or processing was done as part of this thesis; the processed data was provided by Furrer+Frey.

The contact force was estimated using a video of the pantograph head taken by a camera mounted on the roof of the train. The video was used to measure the acceleration of the pantograph head, which, alongside a model of the pantograph dynamics, was used to estimate the contact force. A 20Hz low-pass filter was then applied to the estimated contact force to remove high-frequency noise. The contact-force data was made available both in summary statistics and as a time series.

6.1.2 Test-Track Layout

Most of the track consists of OLE arrangements similar to those considered previously, but of varying lengths and configurations. However, there are also some fundamentally different sections. The short section beginning at 1000m is the neutral section, which is used to electrically separate two electrified wires with different sources. The section from 1900m to 2050m is a single-span overlap: the contact wire approaches the track laterally and in parallel with the track for one span. The section starting at 2200m with the large horizontal range is the first underbridge section of the test track.

The length of contact wire, number and position of messenger spans, number and position of droppers and material properties may all vary from wire to wire. Additionally, the contact wires and messenger wires may not be horizontal, but instead slope either upwards or downwards relative to the track.

The updates to the model are explained and the final Simulink model is presented. This model accepts an overhead line from a database, as well as any two- or three-mass pantograph representation, and can model one or two pantographs, with full or simplified events.

The model is validated against real data from the Old Dalby Test Track. The results are discussed and the current limitations of the model are detailed. Conclusions are drawn about the findings and suggestions are made for further improvement.

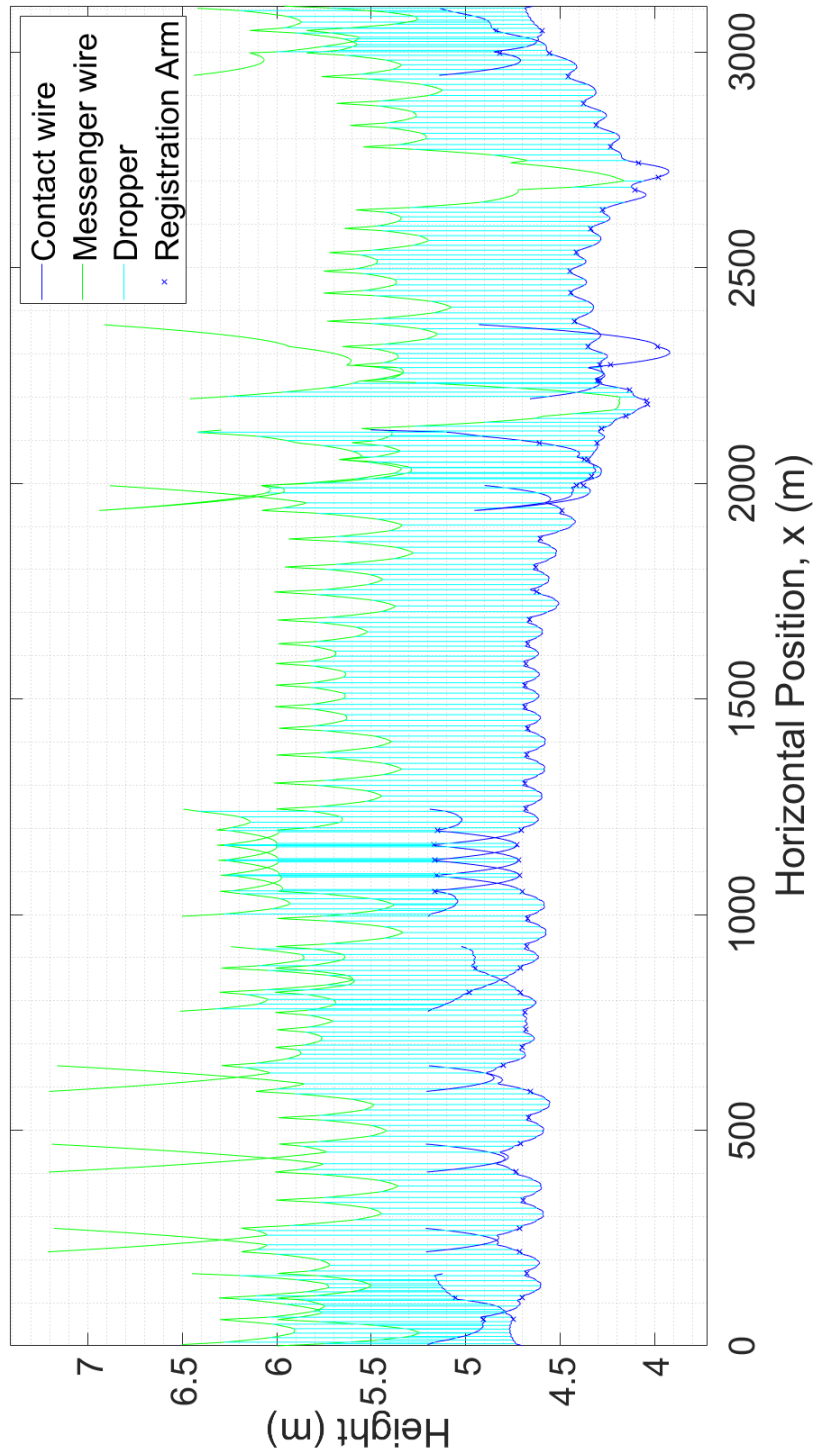


Figure 6.1: Plot of steady-state, vertical wire deflections for the Old Dalby test track

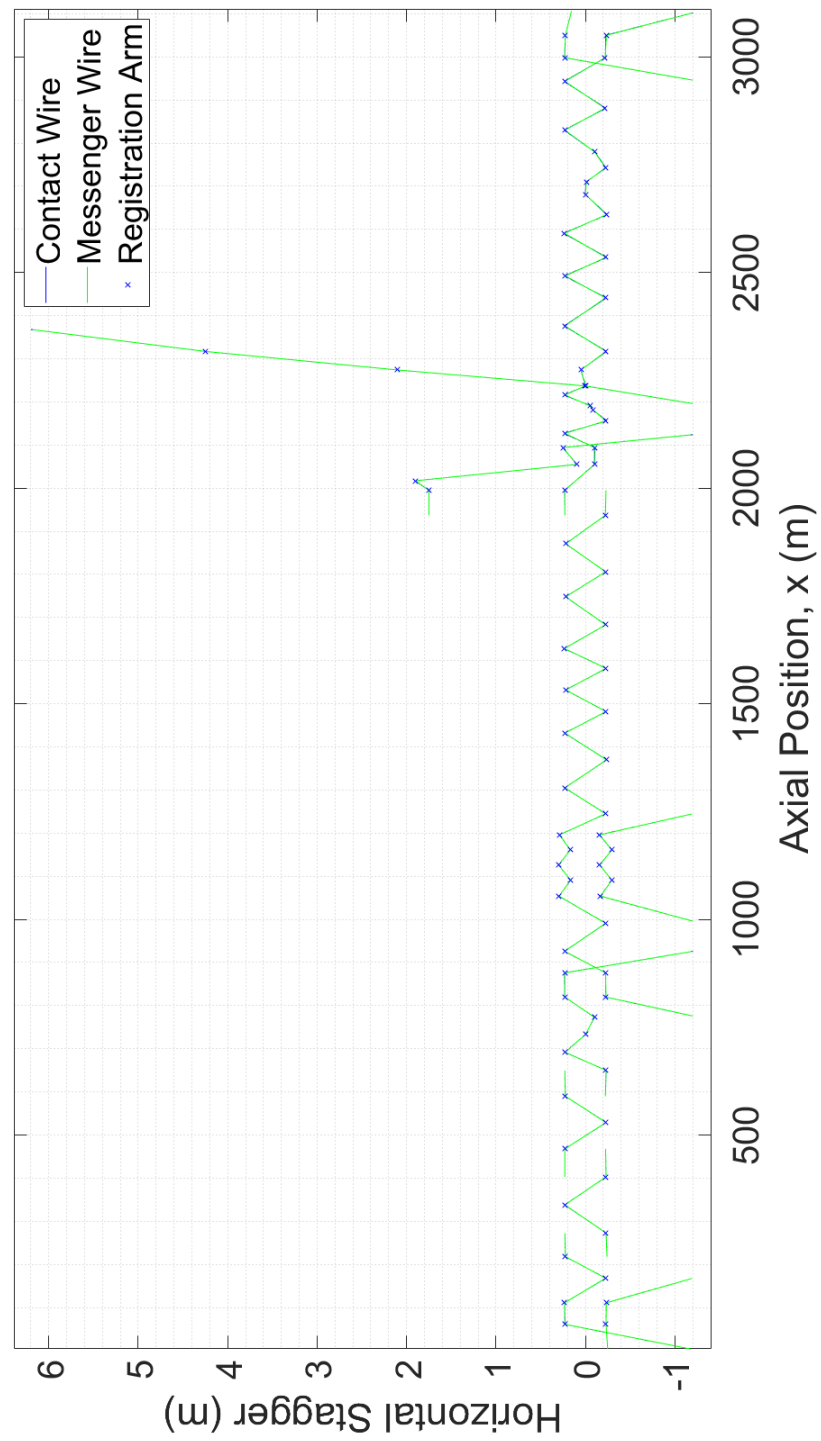


Figure 6.2: Plot of steady-state, horizontal wire deflections for the Old Dalby test track

6.2 Model Updates

6.2.1 Differing Catenary Systems

In the previous events modelling, all the catenary systems were identical. Therefore, the matrices used in the Simulink model did not change when a new wire was loaded in and the back wire removed. However, the overhead systems in the Old Dalby test track are all distinct and have distinct sets of matrices.

In the pre-processing, the matrices for each overhead system were evaluated and compiled into a Simulink bus object. Whenever the front pantograph reached a new contact wire, a triggered subsystem was used to read this bus object and update the system of equations accordingly. Because this was only performed once per new wire reached, it did not substantially reduce the overall simulation speed.

6.2.2 Wire Gradients

Each contact wire and messenger wire has an initial height, h_0 , and a gradient, m . The contact constraints were updated accordingly.

Position Constraint

$$0 = z_3(t) + \bar{z}_3 - \sin \left(\underline{\tilde{\beta}} x_p(t) \right)^T \left(\tilde{V}_1 \tilde{q}_1(t) + \tilde{V}_2 \tilde{q}_2(t) \right) - \sin \left(\underline{\bar{\beta}} x_p(t) \right)^T \underline{\bar{q}} - h_0 - m x_p(t) \quad (6.1)$$

Velocity Constraint

$$\begin{aligned} 0 = & \dot{z}_3(t) - \sin \left(\underline{\tilde{\beta}} x_p(t) \right)^T \left(\tilde{V}_1 \dot{\tilde{q}}_1(t) + \tilde{V}_2 \dot{\tilde{q}}_2(t) \right) \\ & - \left(\left(\underline{\tilde{\beta}} x_p(t) \right)^T \cos \left(\underline{\tilde{\beta}} x_p(t) \right) \right)^T \left(\tilde{V}_1 \tilde{q}_1(t) + \tilde{V}_2 \tilde{q}_2(t) \right) \\ & - \left(\left(\underline{\bar{\beta}} x_p(t) \right)^T \cos \left(\underline{\bar{\beta}} x_p(t) \right) \right)^T \underline{\bar{q}} - m v_p(t) \end{aligned} \quad (6.2)$$

Acceleration Constraint

$$\begin{aligned}
0 = & \ddot{z}_3(t) - \sin(\underline{\tilde{\beta}}x_p(t))^T \left(\tilde{V}_1 \ddot{\tilde{q}}_1(t) + \tilde{V}_2 \ddot{\tilde{q}}_2(t) \right) \\
& - \left(\left(\underline{\tilde{\beta}}v_p(t) \right) .* \cos(\underline{\tilde{\beta}}x_p(t)) \right)^T \left(\tilde{V}_1 \dot{\tilde{q}}_1(t) + \tilde{V}_2 \dot{\tilde{q}}_2(t) \right) \\
& + \left(\left(\left(\underline{\tilde{\beta}}v_p(t) \right)^2 .* \sin(\underline{\tilde{\beta}}x_p(t)) \right) - \left(\left(\underline{\tilde{\beta}}a_p(t) \right) .* \cos(\underline{\tilde{\beta}}x_p(t)) \right) \right)^T \left(\tilde{V}_1 \tilde{q}_1(t) + \tilde{V}_2 \tilde{q}_2(t) \right) \\
& + \left(\left(\left(\underline{\tilde{\beta}}v_p(t) \right)^2 .* \sin(\underline{\tilde{\beta}}x_p(t)) \right) - \left(\left(\underline{\tilde{\beta}}a_p(t) \right) .* \cos(\underline{\tilde{\beta}}x_p(t)) \right) \right)^T \underline{\tilde{q}} - ma_p(t)
\end{aligned} \tag{6.3}$$

The elimination of variables outlined in Section 2.3.12 was used again. The coefficients of h_0 , $mx_p(t)$, $mv_p(t)$ and $ma_p(t)$ in the expressions for the eliminated terms were directly proportional to the coefficients of \bar{z}_3 , $z_3(t)$, $\dot{z}_3(t)$ and $\ddot{z}_3(t)$, respectively.

6.2.3 Aerodynamic Pantograph Forces

The ‘Z’-shape of the pantograph gives rise to a downward force on the moving pantograph head due to air resistance. This is counteracted by the use of an aerofoil on the pantograph head, which produces an upthrust to negate the downward force. The mass-spring-damper model includes only the aerofoil force as a function of train speed. This force is $P_v v_p^2(t)$.

$$m_3 \ddot{z}_3(t) = c_3 \dot{z}_2(t) - c_3 \dot{z}_3(t) + k_3 z_2(t) - k_3 z_3(t) - \lambda(t) + P_v v_p^2(t) \tag{6.4}$$

For the pantographs used in the line tests simulated here, $P_v = 0.0077 \text{Ns}^2\text{m}^{-2}$ for the front pantograph and $P_v = 0.0060 \text{Ns}^2\text{m}^{-2}$ for the rear pantograph. At a typical train speed of 185km/hour (115mph), this gives uplift forces of 20N and 16N. However, if the aerofoil is correctly designed, then the net vertical aerodynamic force on the pantograph head should be close to zero. The aerofoil force will increase quadratically with train speed, but so will the downward force. Therefore, the resultant force on the pantograph head will be much smaller in magnitude than 20N. The model used here includes the aerofoil force and neglects the downward force, though it may be more reasonable to neglect both of these aerodynamic forces.

When the train direction is reversed, the orientation of each pantograph is also reversed. Therefore, the ‘Z’-shape causes an upthrust instead of a downward force. However, the aerofoil is designed to minimise this directional effect.

6.2.4 Calculation of Original Dropper Lengths

The dropper lengths given in the database are steady-state, tensioned lengths. This is because the droppers are adjusted to the desired lengths upon installation and unstretched lengths are not measured.

In order to evaluate the steady-state sag and to implement dropper unloading, the unstretched dropper lengths must be known. To achieve this, the unstretched lengths were used as additional states in the steady-state MATLAB code and evaluated alongside the wire deflections.

6.2.5 Choice of Eliminated Eigenmodes

Previously, the eliminated eigenmode for single-pantograph contact conditions and pair of eigenmodes for double-pantograph contact conditions were chosen in pre-processing by examining the inverted terms, $\tilde{S}(\underline{x}_p(t))$ and $\tilde{F}_1(\underline{x}_p(t))$. For the 2018 European Standard's catenary system, the choice of eliminated eigenmodes was independent of $\underline{x}_p(t)$. However, for some of the catenary systems in the Old Dalby test track, no eliminated eigenmode or pair of eigenmodes was suitable for all $\underline{x}_p(t)$.

A set of eigenmodes is suitable for elimination if and only if the two terms that are inverted in the elimination-of-variables process are nonsingular for all $\underline{x}_p(t)$ along the contact wire. The Simulink model requires suitable eliminations for all contact conditions for all $\underline{x}_p(t)$. Because the inverted terms are functions only of $\underline{x}_p(t)$, the velocity profile of the train does not affect the choice of eliminated eigenmodes.

The original contact-wire modes, before eigenvector decomposition, are sine waves of increasing spatial frequency, with the first mode's wavelength being twice the length of the wire. After diagonalisation, the eigenmodes resemble the original sine waves, but are distorted by the messenger-wire dynamics, as well as the forces exerted by the droppers and registration arms.

One Pantograph in Contact with Wire

$$S(\underline{x}_p(t)) = \sin \left(\tilde{\beta} \underline{x}_p(t) \right)^T \tilde{V}_1 \quad (6.5)$$

$$F(x_p(t)) = \tilde{W}_1 (I - A_3)^{-1} \sin(\tilde{\beta} x_p(t)) \quad (6.6)$$

First Catenary System

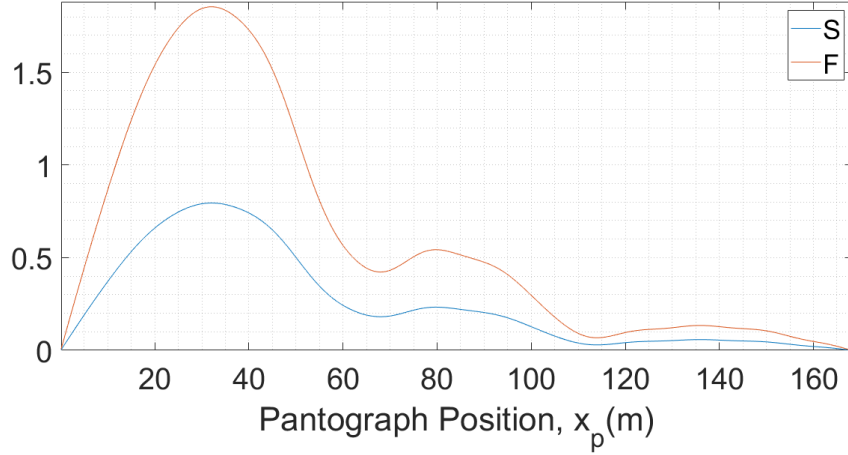


Figure 6.3: Plot of values of S and F against horizontal position for first catenary system in contact with one pantograph, with the first eigenmode eliminated

Figure 6.3 shows the values of the two inverted scalars, $S(x_p(t))$ and $F(x_p(t))$, as functions of $x_p(t)$ for the first catenary system. Since the only zeros are at the contact wire's ends, this elimination is suitable for the whole wire length.

Second Catenary System

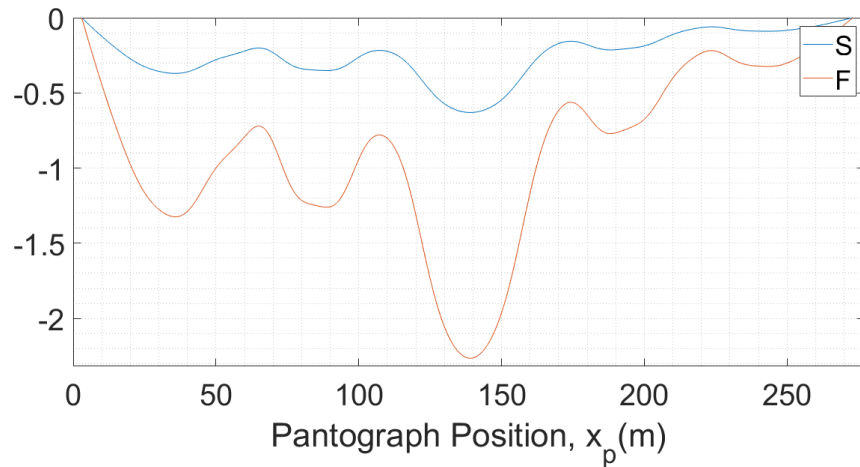


Figure 6.4: Plot of values of S and F against horizontal position for second catenary system in contact with one pantograph, with the first eigenmode eliminated

As before, the only zeroes are at the ends of the contact wire, so the first eigenmode can be eliminated for all $x_p(t)$. This is also true for the third and fourth catenary systems.

Fifth Catenary System

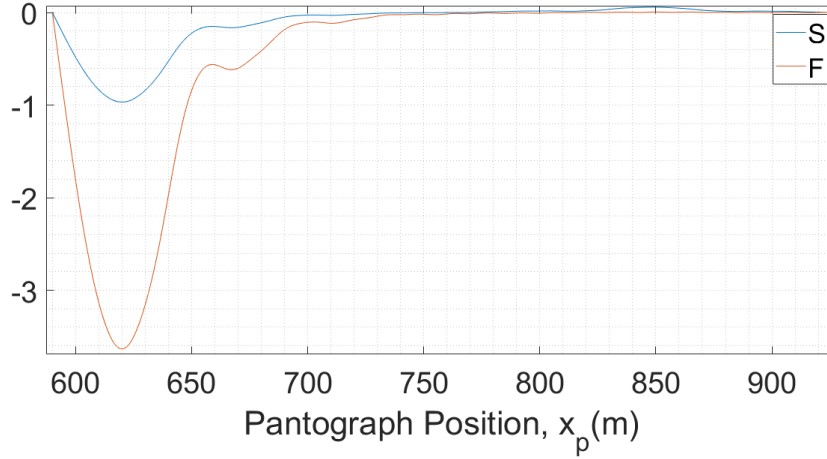


Figure 6.5: Plot of values of S and F against horizontal position for fifth catenary system in contact with one pantograph, with the first eigenmode eliminated

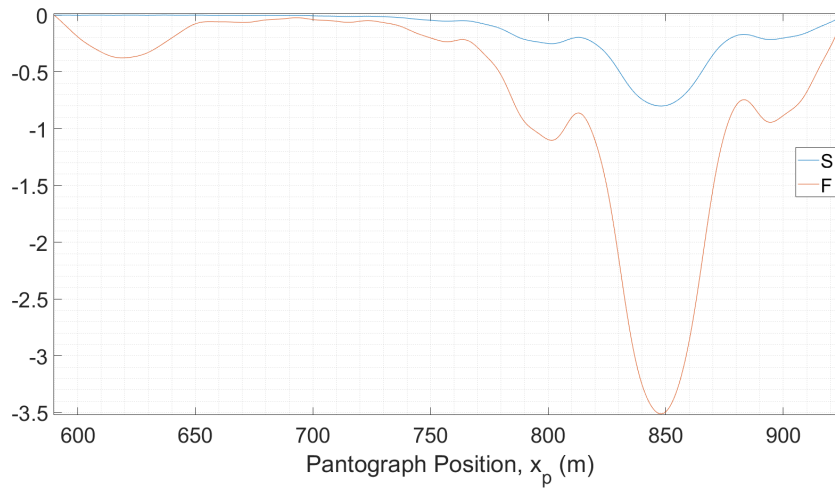


Figure 6.6: Plot of values of S and F against horizontal position for fifth catenary system in contact with one pantograph, with the second eigenmode eliminated

Figure 6.5 shows the first zero crossing is at 760m with the first eigenmode eliminated. Figure 6.6 shows the last zero crossing is at 654m with the second eigenmode eliminated. To avoid dividing by zero, the first eigenmode was eliminated initially and $\tilde{q}_1(t)$ was switched to the second eigenmode between 654m and 760m.

Sixth Catenary System

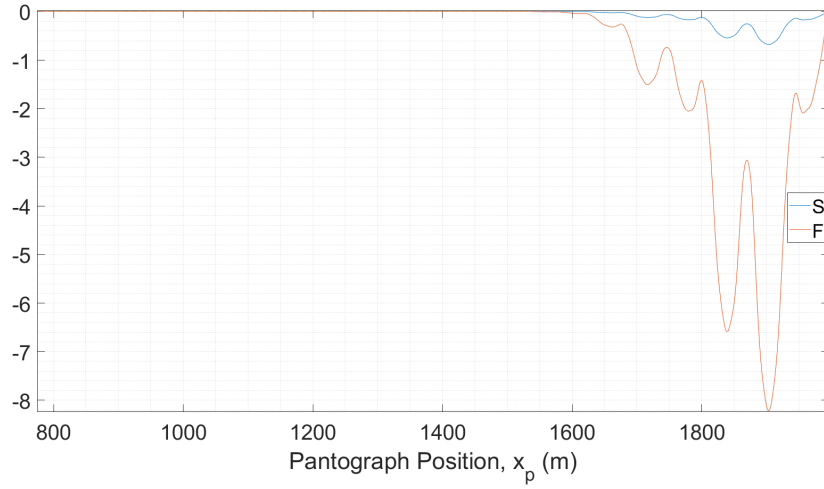


Figure 6.7: Plot of values of S and F against horizontal position for sixth catenary system in contact with one pantograph, with the first eigenmode eliminated

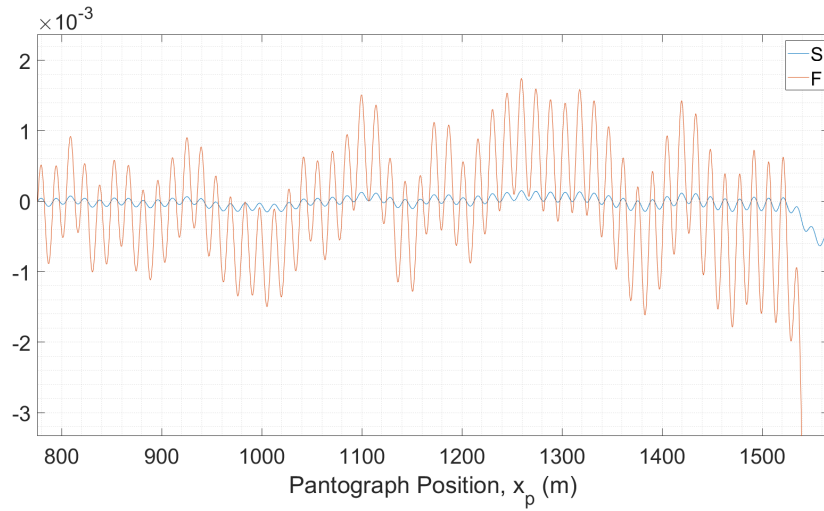


Figure 6.8: Zoomed-in plot of values of S and F against horizontal position for sixth catenary system in contact with one pantograph, with the first eigenmode eliminated

Figure 6.7 and Figure 6.8 both show $S(x_p(t))$ and $F(x_p(t))$ for the sixth catenary system, with the first eigenmode eliminated. While there are no zero crossings for the last 500m of the contact wire, there are hundreds of zero crossings in the first 700m.

It was observed that no single eigenmode was suitable for elimination for all $x_p(t)$. However, different eigenmodes were suitable in different regions and it was possible to find a sequence of eliminations that gave nonsingular $S(x_p(t))$ and $F(x_p(t))$ for all $x_p(t)$.

Two Pantographs in Contact with Wire

$$\underline{x}_p(t) = \begin{pmatrix} x_p^f \\ x_p^b \end{pmatrix} = \begin{pmatrix} x_p^f \\ x_p^f - x_{\text{sep}} \end{pmatrix} \quad (6.7)$$

$$S(\underline{x}_p(t)) = \sin \left(\tilde{\beta} \underline{x}_p^T \right)^T \tilde{V}_1 \quad (6.8)$$

$$F_1(\underline{x}_p(t)) = \tilde{W}_1 (I - A_3)^{-1} \sin \left(\tilde{\beta} \underline{x}_p^T \right) \quad (6.9)$$

Because the inverted terms are 2×2 matrices when two pantographs are in contact with the wire, the determinants of these terms were used to check for singularity and to plot the results.

First Catenary System

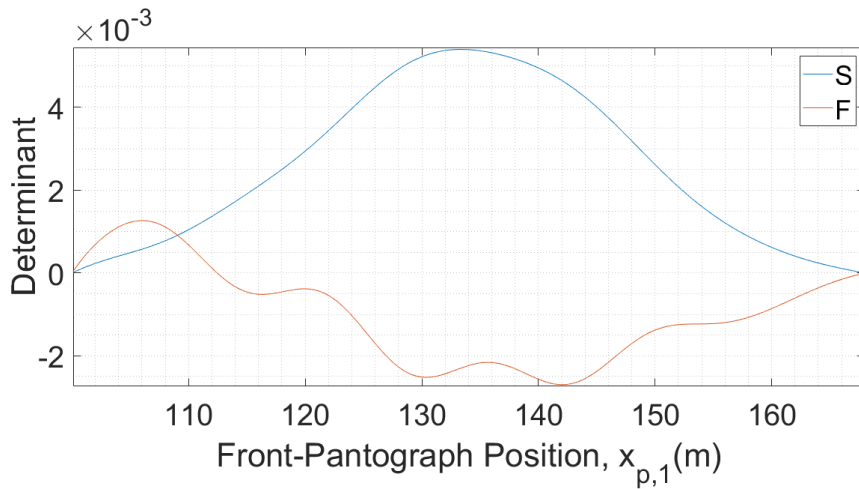


Figure 6.9: Plot of determinants of S and F against horizontal position for first catenary system in contact with two pantographs, with the first and second eigenmodes eliminated

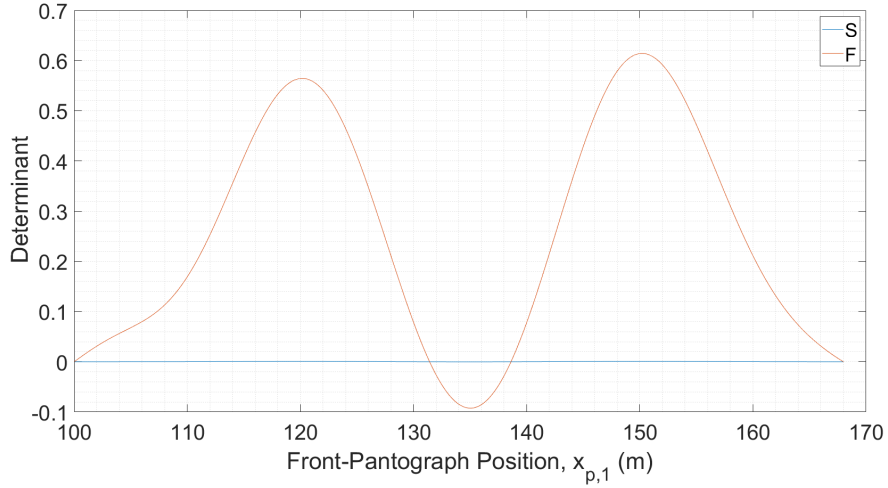


Figure 6.10: Plot of determinants of S and F against horizontal position for first catenary system in contact with two pantographs, with the sixth and seventh eigenmodes eliminated

Figure 6.9 shows the determinants of $S(\underline{x}_p(t))$ and $F(\underline{x}_p(t))$ as functions of $\underline{x}_p(t)$ for the first catenary system in contact with two pantographs. Since there is a zero crossing at 112m, eliminating the first and second eigenmodes is not suitable for the whole wire. Figure 6.10 shows that using $\tilde{q}_1 = \tilde{q}(6 : 7)$ for the first 125m and then switching to $\tilde{q}_1 = \tilde{q}(1 : 2)$ resolves the problem.

Second Catenary System

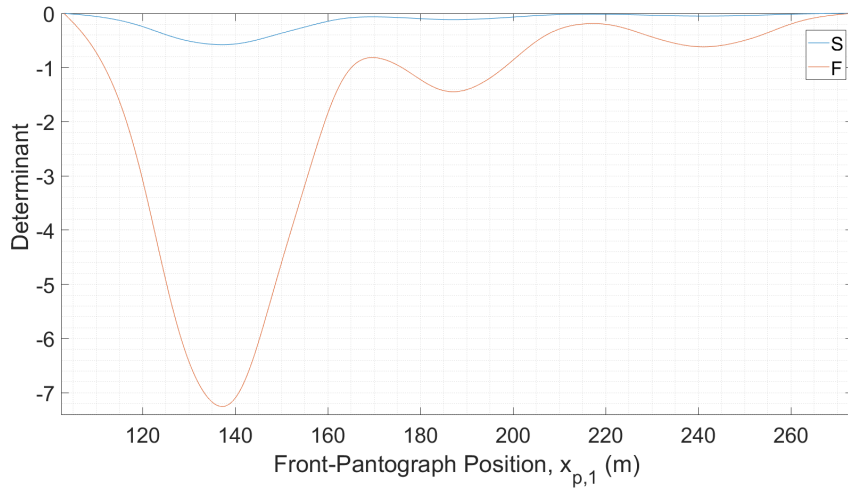


Figure 6.11: Plot of determinants of S and F against horizontal position for second catenary system in contact with two pantographs, with the first and second eigenmodes eliminated

Eliminating the first and second eigenmodes is always suitable for the second catenary system. The same was found to be true for the third and fourth catenaries. For the fifth catenary, always eliminating the second and third eigenmodes was found to be suitable.

Sixth Catenary System

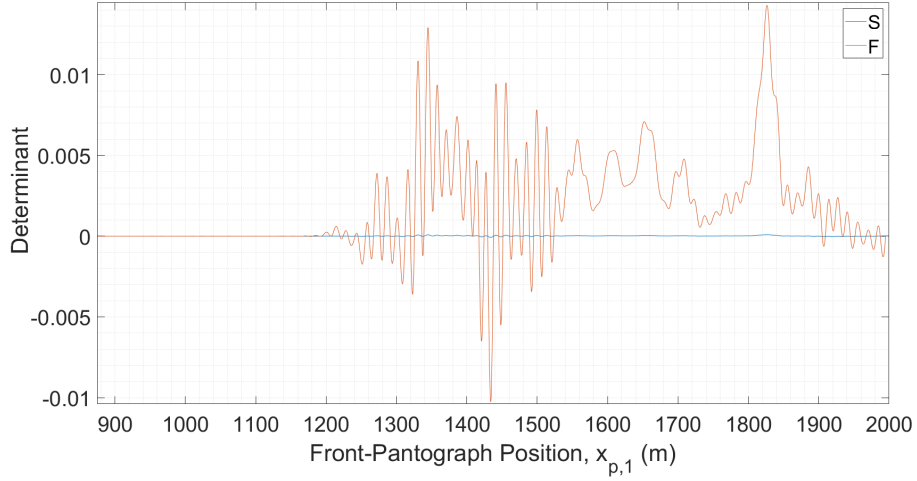


Figure 6.12: Plot of determinants of S and F against horizontal position for sixth catenary system in contact with two pantographs, with the first and second eigenmodes eliminated

The results for the sixth catenary system in contact with two pantographs were similar to those for a single pantograph. Therefore, the sequence of eigenmodes to be eliminated had to be chosen carefully.

Elimination Algorithm

The following algorithm was used in pre-processing to determine the choice of eliminated eigenmodes as a function of $\underline{x}_p(t)$ for double-pantograph contact conditions.

1. Set $\bar{x}_p^f = 0$ and $i = 0$.
2. $i \leftarrow i + 1$.
3. Eliminate the i^{th} and $(i + 1)^{th}$ eigenmodes.
4. Find the smallest $x_p^f(t) > \bar{x}_p^f$ for which the determinant of $S(\underline{x}_p(t))$ or $F(\underline{x}_p(t))$ is zero, $x_{p,0}$.

5. If $x_{p,0} < \bar{x}_p^f + x_p^{\text{minstep}}$ go to 2).

6. If the end of the wire has not been reached, set $\bar{x}_p^f = x_{p,0} - x_p^{\text{stepback}}$, set $i = 0$ and go to 2).

x_p^{minstep} and x_p^{stepback} are constants chosen with the goal of minimising the number of $x_p(t)$ -events while ensuring that an appropriate sequence of eigenmode eliminations exists.

This algorithm was used to schedule $x_p(t)$ -events in the pre-processing, giving a vector of $x_p(t)$ -values and a matrix of eigenmodes to be eliminated after reaching each position in that vector. The algorithm used for single-pantograph contact conditions was entirely analogous. These events were implemented in the same manner as new-wire events and the matrices were updated accordingly.



Figure 6.13: Image of arcing due to loss of contact on the Old Dalby track (credit: Furrer+Frey)

6.3 Results

The steady-state modelling was performed for the first eleven catenary systems of the Old Dalby test track with no issues. This section covered over 3km of the track, as shown in the steady-state plots.

The dynamic modelling was performed only for the first five catenary systems, because problems with events modelling arose due to the very long sixth contact wire and the abnormal layout of the seventh catenary system, which is neutral section. In practice, these parts of the overhead line are poorly designed and can cause loss of contact and arcing, as illustrated in Figure 6.13. The dynamic results for the first five wires are presented and the model's limitations are discussed.

The Simulink model used ode45 to solve the ODE for the dynamic pantograph-catenary interaction. All of the settings were identical to those used in the previous chapters.

Frequency properties of the catenary model and the pantograph model are shown in Table 6.1. The pantograph cut-off frequency was chosen to be 15.6Hz, giving 95dB of attenuation. The number of vertical contact-wire modes included for each catenary section was calculated using (2.138) and the number of horizontal contact-wire modes was set to half this number, as horizontal dynamic deflections were expected to be very small. The number of messenger-wire modes was also calculated using (2.138). After diagonalisation, the number of eigenmodes included was calculated using a cut-off eigenvalue magnitude of 2×10^4 , which was chosen by inspecting some of the catenary sections' eigenvalue matrices for large steps in magnitude.

Catenary Section	1	2	3	4	5
Number of contact-wire modes	45	72	67	66	90
Number of messenger-wire modes per span	14	14	16	15	10
Number of eigenmodes after diagonalisation	102	172	166	163	214
Natural frequency of highest mode (Hz)	15.3	16.1	16.1	15.9	16.1
Pantograph-force frequency (Hz)	5.5	3.8	2.9	2.9	4.0
Damping factor	0.02	0.02	0.02	0.02	0.02

Table 6.1: Table of frequency properties of catenary model and pantograph model

For all but one of the catenary sections, the natural frequency of the highest eigenmode

is higher than the cut-off frequency of the pantograph. However, since the pantograph is excited by the droppers at the pantograph-force frequency, which is much lower than the pantograph cut-off frequency, there should be no need to reproduce pantograph dynamics close to the pantograph cut-off frequency.

6.3.1 Steady-State Wire Deflections

Vertical Deflections

Figure 6.1 shows the vertical steady-state deflections for the first eleven catenary systems of the Old Dalby track. These catenary systems are highly irregular, with differing lengths, heights, gradients, messenger-span layouts and dropper distributions. The short catenary system between 996m and 1245m is the neutral section. This section is not electrified and allows different sections of the overhead line to be powered by different power grids.

Some of the messenger spans of later catenary systems contain few or no droppers, which causes large contact-wire sag. These catenary designs may have been chosen to allow the train to pass under bridges, in which case realistic simulation of the pantograph-catenary interaction could require the addition of discrete components to the model.

Horizontal Deflections

The registration-arm positions dictate the stagger of the contact wire. The messenger wire's steady-state stagger matches the contact wire's, but there is no dynamic messenger-wire stagger, because no external, dynamic, horizontal forces are applied. The dynamic, horizontal contact-wire deflection is assumed to be so small that the droppers remain approximately vertical and the dropper tensions have no horizontal components.

The configuration of catenary systems for the Old Dalby test track is highly atypical and is not representative of a regular electric-train journey. This configuration has been chosen to stress test the pantograph-catenary system and identify any problems in the physical overhead system, as well as unrealistic aspects of pantograph-catenary models.

6.3.2 Snapshots

Due to problems with events modelling, only the first five sections of the test track were used in the final simulations. These spans run from 0m to 900m in Figure 6.1 and Figure 6.2.

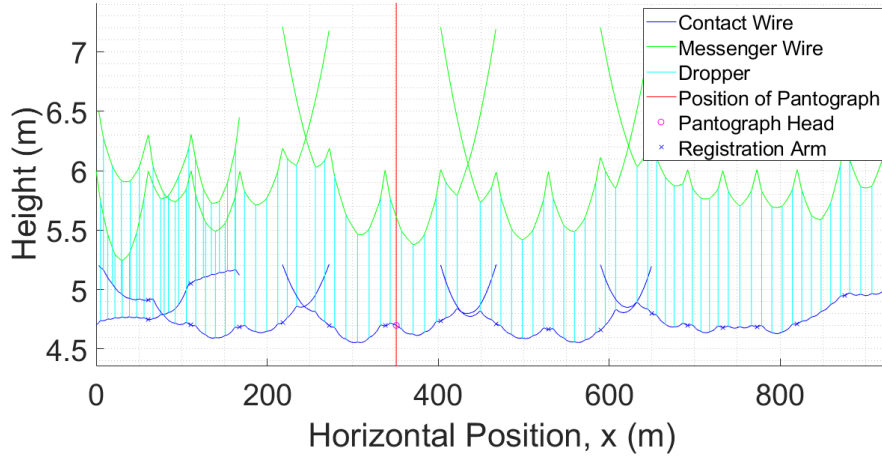


Figure 6.14: Snapshot of vertical and horizontal wire deflections of Old Dalby test track with one pantograph at 115 mph

Figure 6.14 and Figure 6.15 are snapshots of the dynamic wire deflections at 115 mph with a single pantograph and with two pantographs, respectively. While the dynamic, horizontal contact-wire deflection is quite large close to the point of contact, the registration arms barely move.

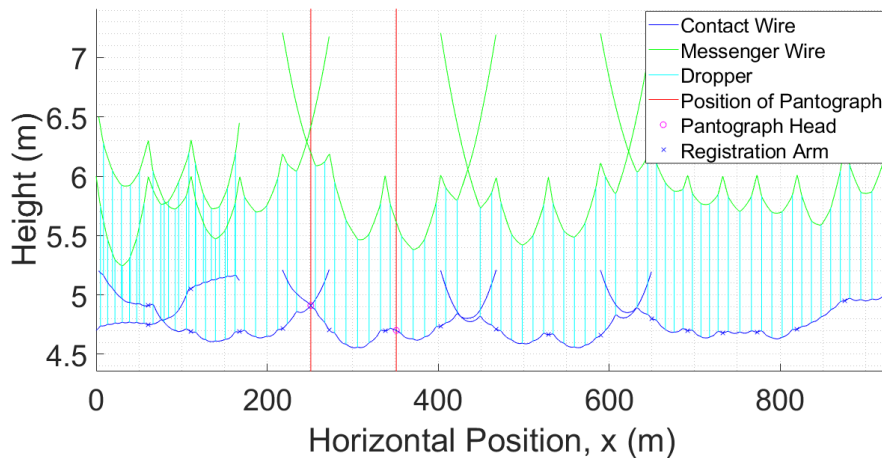


Figure 6.15: Snapshot of vertical and horizontal wire deflections of Old Dalby test track with two pantographs at 115 mph

The deflections close to the front pantograph's point of contact were found to be very

similar with and without the rear pantograph, but the deflections for around the rear pantograph were much larger due to the front pantograph perturbing the catenary wires. This is consistent with the results presented in the previous chapter.

Because only two catenary systems were modelled at any given time, the dynamic deflections for all other catenaries were assumed to be zero. This assumption was shown to be reasonable by checking the wire deflections immediately before a wire was removed from the model.

6.3.3 Force Plots

One Pantograph

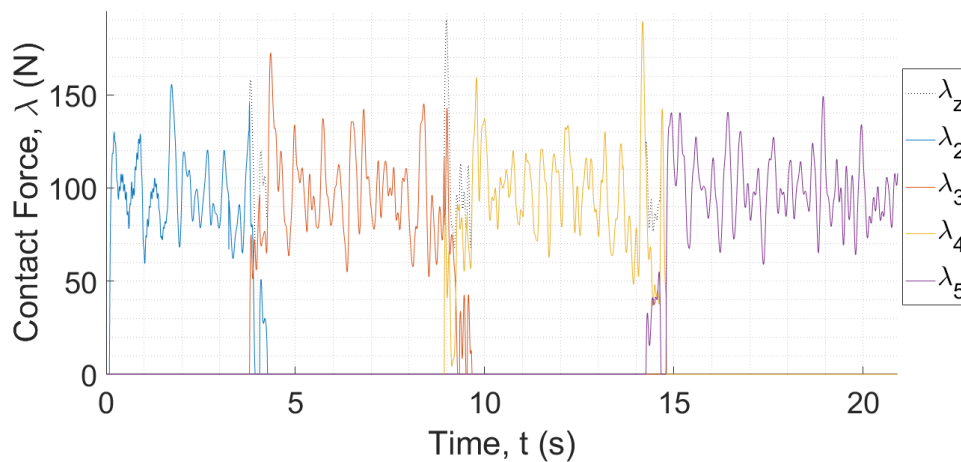


Figure 6.16: Plot of contact forces against time for the Old Dalby test track at 80 mph with a single pantograph

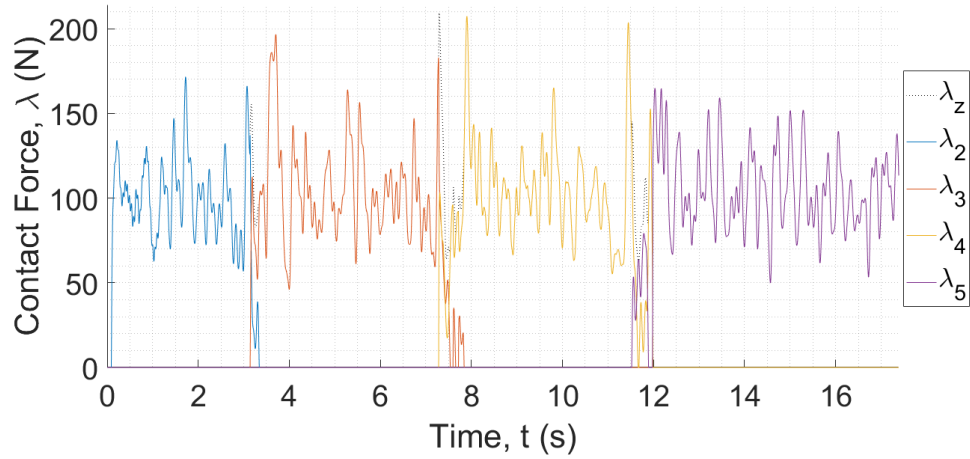


Figure 6.17: Plot of contact forces against time for the Old Dalby test track at 100 mph with a single pantograph

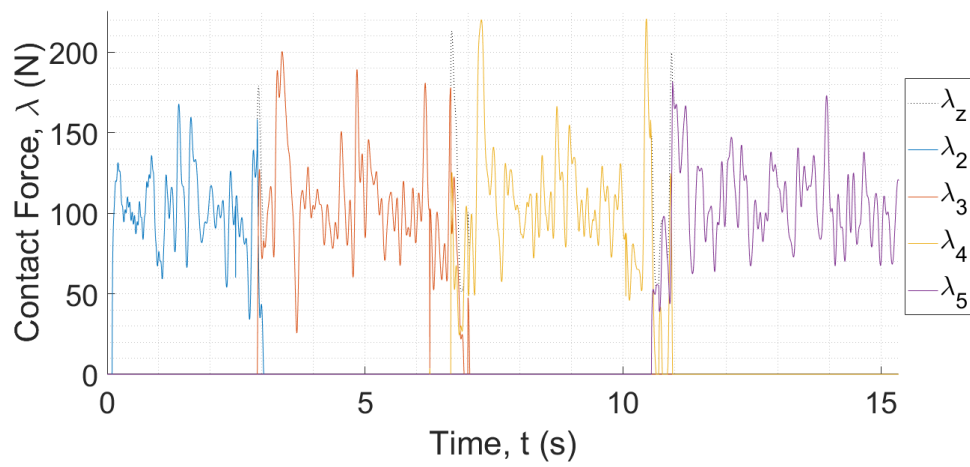


Figure 6.18: Plot of contact forces against time for the Old Dalby test track at 110 mph with a single pantograph

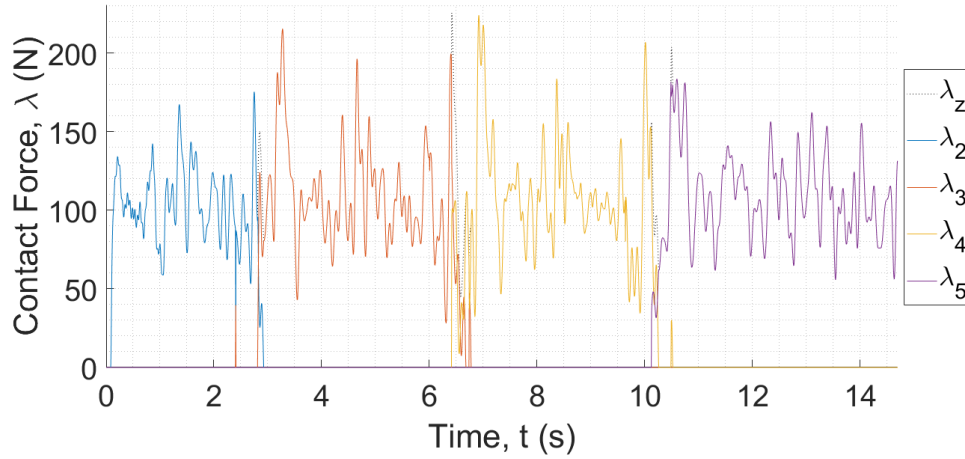


Figure 6.19: Plot of contact forces against time for the Old Dalby test track at 115 mph with a single pantograph

$\lambda_z(t)$ is the total downward contact force exerted on the pantograph head by all wires, whereas $\lambda_i(t)$ is the contact force between the i^{th} contact wire and the pantograph. It can be seen that the transitions between the second to fifth contact wires are fairly smooth, with the total contact force only spiking slightly as the pantograph transitions from one wire to the next.

As the train speed increases, the variance of the contact force increases and the force spikes before and after transition events increase in magnitude, but the periodicity remains. This is in accordance with the results shown in previous chapters.

Two Pantographs

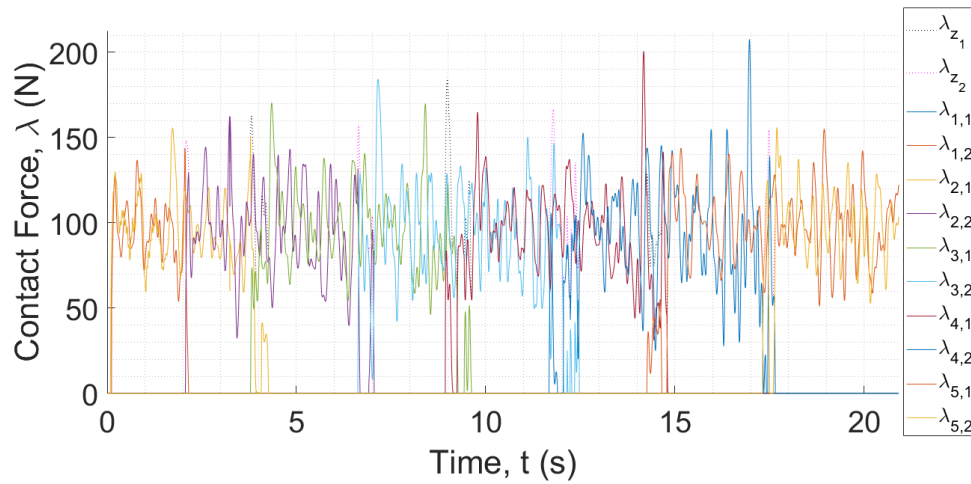


Figure 6.20: Plot of contact forces against time for the Old Dalby test track at 80 mph with two pantographs

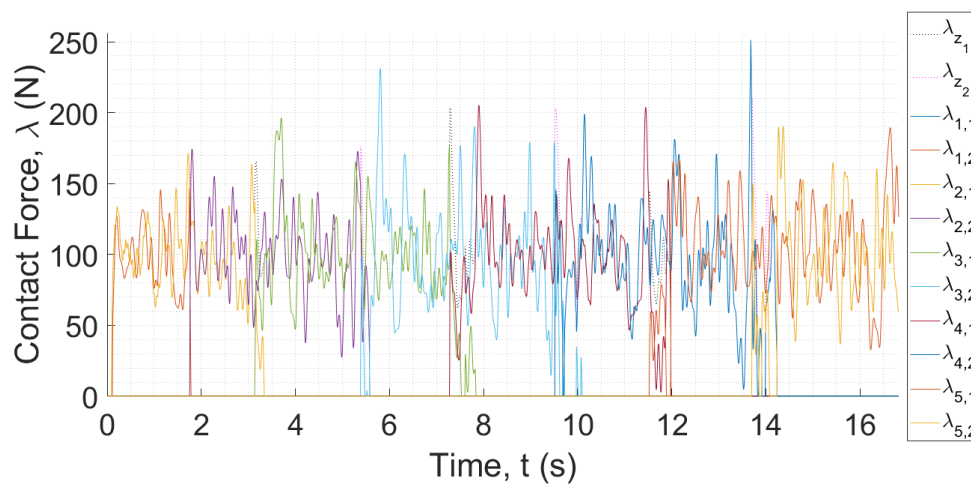


Figure 6.21: Plot of contact forces against time for the Old Dalby test track at 100 mph with two pantographs

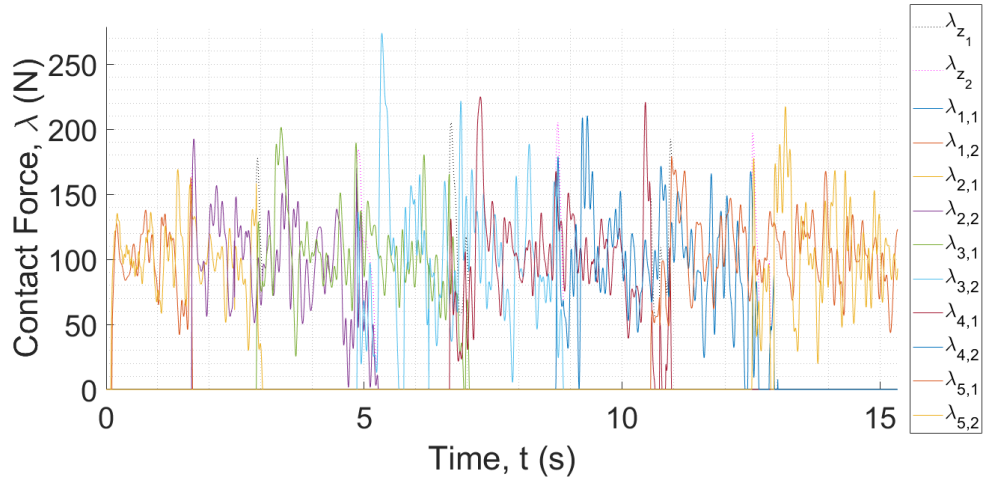


Figure 6.22: Plot of contact forces against time for the Old Dalby test track at 110 mph with two pantographs

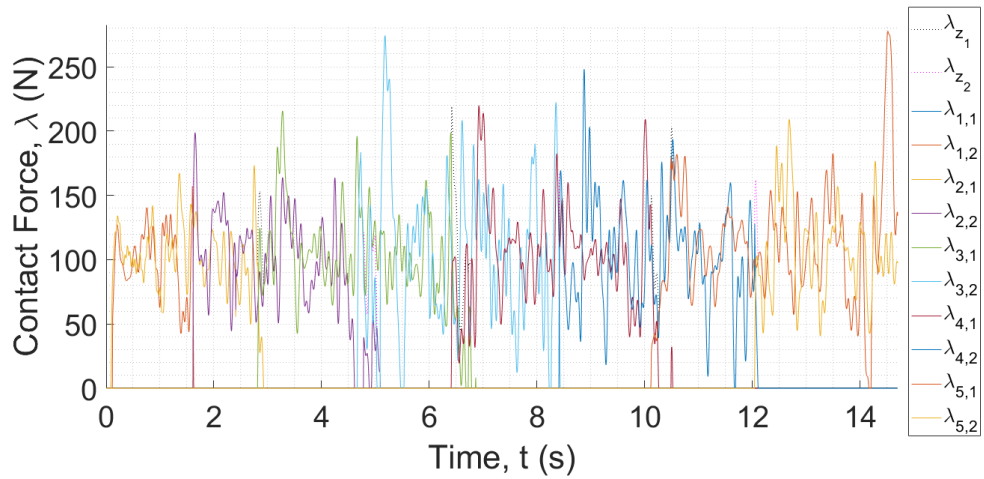


Figure 6.23: Plot of contact forces against time for the Old Dalby test track at 115 mph with two pantographs

The separation between the two pantographs was 100m for all of the two-pantograph results presented in this chapter. With this separation, the front pantograph is not significantly affected by the rear pantograph's interactions with the contact wires, but the rear pantograph is heavily influenced by the front pantograph perturbing the contact wires.

The variance of the contact force for the rear pantograph is far greater than the variance for the front pantograph. This causes the rear pantograph to come out of contact at 110 mph and 115 mph, whereas the front pantograph only falls out of contact at 115 mph.

6.3.4 Comparison to Real Line-Test Data

The measured contact-force data from the Old Dalby tests was provided by Furrer+Freymann and is shown in the tables below. The gathering and processing of data was performed by Serco, who used their Dewesoft 7 data logger. There are two main sources of measurement errors that should be considered:

1. The measurements of contact force may be unrealistic. These measurements use built-in sensors on the pantograph head.
2. The train speed may not be constant. The driver tried to maintain the prescribed speed for each test, as many pieces of simulation software require a constant train speed, but it is not possible to keep the speed of a real train exactly constant. For future line tests and simulations, this error could be mitigated by measuring the velocity profile of the train and using this as an input to the Simulink simulation.

Only the tables of contact-force statistics have been compared to results from the Simulink model so far. Time series of the contact force and of the pantograph-head position are also available. The tables of contact-force statistics were chosen for the first step in validating the Simulink model, because they allow for a simple quantitative comparison of results and can catch many different forms of model error; the time series will be used for validation once the current limitations of the Simulink model have been addressed.

Single Pantograph

Train speed (mph)	80		100		110		115	
	Line Test	Simulink	Line Test	Simulink	Line Test	Simulink	Line Test	Simulink
Mean contact force (N)	95.7	98.97	99.3	104.33	97.4	107.22	101.3	108.89
Standard deviation of contact force (N)	17.7	21.58	21.5	27.06	23.8	30.55	26.5	31.63
Minimum contact force (N)	12.3	43.71	22.8	45.95	18.3	3.71	18.4	28.12
Maximum contact force (N)	182.5	190.07	194.8	209.15	192.6	220.75	211.1	225.71
Mean force - 3 s.d. (N)	42.6	34.21	34.7	23.14	26.0	15.56	22.0	14.00
Noise-to-signal ratio	0.19	0.22	0.22	0.26	0.24	0.28	0.26	0.29

Table 6.2: Table of Old Dalby results with a single pantograph

■ Error ≤ 5% ■ 5% < Error ≤ 10% ■ Error > 10%

The noise-to-signal ratio is defined as the standard deviation of the contact force divided by the mean contact force. The results are quite similar, but there are two major sources of errors:

1. The line-test results are for the full Old Dalby track, whereas only the first five catenary systems were simulated. The later catenary systems use different layouts and will give different contact-force distributions.
2. The damping model strongly influences the contact forces. In order to closely match the real data, the damping factor could be optimised or the form of damping could be changed entirely.

Two Pantographs: Front Pantograph

Train speed (mph)	80		100		110		115	
	Line Test	Simulink	Line Test	Simulink	Line Test	Simulink	Line Test	Simulink
Mean contact force (N)	106.4	99.04	112.8	104.74	109.5	107.10	113.5	110.48
Standard deviation of contact force (N)	20.0	22.85	25.6	29.27	28.0	30.76	29.7	37.46
Minimum contact force (N)	37.6	43.96	26.9	32.67	26.0	0.71	17.2	0.00
Maximum contact force (N)	193.7	200.63	223.0	205.42	223.4	224.88	243.4	277.69
Mean force - 3 s.d. (N)	46.6	30.48	36.0	16.93	25.5	14.82	24.5	-1.89
Noise-to-signal ratio	0.19	0.23	0.23	0.28	0.26	0.29	0.26	0.34

Table 6.3: Table of Old Dalby results for the front pantograph

■ Error ≤ 5% ■ 5% < Error ≤ 10% ■ Error > 10%

Two Pantographs: Rear Pantograph

Train speed (mph)	80		100		110		115	
	Line Test	Simulink	Line Test	Simulink	Line Test	Simulink	Line Test	Simulink
Mean contact force (N)	98.7	97.35	99.4	101.30	110.3	104.73	115.2	104.77
Standard deviation of contact force (N)	22.4	25.67	28.1	35.08	31.8	41.89	33.0	42.87
Minimum contact force (N)	-7.8	25.08	-7.3	4.79	-5.1	0.0	-4.5	0.00
Maximum contact force (N)	246.6	207.65	227.2	251.37	237.4	273.76	253.4	274.23
Mean force - 3 s.d. (N)	31.5	20.33	15.3	-3.05	15.0	-21.95	16.2	-23.84
Noise-to-signal ratio	0.23	0.26	0.28	0.35	0.29	0.40	0.29	0.41

Table 6.4: Table of Old Dalby results for the rear pantograph

■ Error ≤ 5% ■ 5% < Error ≤ 10% ■ Error > 10%

The estimated minimum contact force in the line-test data is negative, which is not realistic. Since this estimate relies on a video of the pantograph head to measure its acceleration and on a model for the pantograph dynamics to convert this acceleration into a force, inaccuracies in the video or the model can lead to unrealistic results. These errors add noise to the contact-force estimation, but they do not introduce a drift in signal offset.

The most important result is the minimum contact force, because this indicates the quality of current collection and the likelihood of loss of contact. The loss of contact shown at higher speeds in Table 6.3 and Table 6.4 suggests that more damping is needed. The damping factor used, $\zeta = 2 \times 10^{-3}$, seems to be unrealistically small.

The numerical results from the two-pantograph simulation show reasonable agreement with the real data. However, it is not clear how much of the disparity is due to only the first five catenaries being modelled and how much is due to unrealistic aspects of the model, so these results are not very useful. This final Simulink model should be treated as a proof of concept of the Galerkin approach, rather than fully functional software, although it is not far from being useful in modelling real tracks.

6.3.5 Simulation Speed

	One Pantograph				Two Pantographs			
Train speed (mph)	80	100	110	115	80	100	110	115
Pre-processing (s)	1.57	1.51	1.59	1.53	1.74	1.69	1.72	1.73
Simulation time (s)	101	90	79	73	174	165	141	135
Post-processing (s)	1.32	1.01	0.87	0.74	1.76	1.57	1.23	1.28
Real time (s)	20.91	17.39	15.35	14.70	20.91	17.39	15.35	14.70
Relative speed	0.20	0.19	0.19	0.20	0.12	0.10	0.11	0.11

Table 6.5: Table of simulation speeds for the Old Dalby model

The relative simulation speeds shown in Table 6.5 are faster than those for the 2018 European Standard, even when compared to the model without events, and this is chiefly due to the short contact-wire lengths for the Old Dalby track. The first five contact wires are relatively short, with the longest being 336m long. Shorter wires require fewer eigenmodes and therefore give faster simulation speeds, whereas the 1219m-long sixth contact wire would take much longer to model.

The current Simulink model requires the same number of modes to be used at all times, so the matrices corresponding to shorter wires are appended with zeros and the simulation speed decreases for all wires when the sixth wire is included, even when this wire is not currently being modelled. However, it should be possible to use variable-sized matrices to recover the excellent simulation speeds for shorter wires even when longer wires must be modelled as well.

6.3.6 Limitations

Lack of Event Robustness

The current model encounters problems with high-frequency chatter when certain impact events occur: the pantograph bounces in and out of contact with the wire and the time step tends to zero, meaning that the model cannot move past the event. This problem most commonly arises when the front pantograph transitions from the neutral section back to the long sixth contact wire.

The events model explained in Chapter 5 worked well for the 2018 standard's catenary system and for the first five catenary systems on the Old Dalby track, but is not able to simulate abrupt transitions between abnormal catenary structures. The infinite chatter that can arise from impact modelling is well documented and some potential solutions are suggested in Section 7.2.

High-Spatial-Frequency Messenger Vibrations

Two of the messenger spans in the fifth catenary system produce unrealistic results: as the pantograph passes along one of these spans, high-spatial-frequency fluctuations are observed in the messenger wire. This might be caused by too many pre-diagonalisation modes being used for the messenger span, or the problem could be more subtle. This issue is only observed for certain messenger spans: most of the spans show realistic deflections.

Size of Bus Object

In the preprocessing code, the necessary matrices are calculated for each contact wire and set of eliminated eigenmodes and saved into a structure. This structure is passed into the Simulink model as a bus object and a triggered subsystem is used to update the matrices whenever a new-wire event occurs or the set of eliminated eigenmodes changes.

The maximum size of input that Simulink can take is two gigabytes. The bus object exceeds this limit if the sixth catenary system is included, so the number of pre-diagonalisation terms must be reduced. This problem could be avoided by adjusting the Simulink model to use variable-sized matrices and computing the matrices each time a new wire were reached or the set of eigenmodes changed.

6.4 Conclusions

The model was updated to simulate a real test track. The details of the overhead catenary systems were read from a spreadsheet and used to create a MATLAB structure, which was passed in to the Simulink model. The sequence of eliminated eigenmodes for each contact condition was determined in preprocessing in order to avoid dividing by zero or inverting a singular matrix.

The final model is largely a success: it is able to simulate an arbitrary overhead line comprised of many irregular catenary systems and produce realistic results. However, limitations of the simplistic events modelling cause problems with robustness and further work is needed in order to model certain parts of the overhead line.

Chapter 7

Conclusions and Further Work

7.1 Conclusions

Pantograph-catenary simulation software has been produced, using the Galerkin method to solve the Euler-Bernoulli beam equations for the contact wire and messenger wire. This software was validated against BS:EN 50318:2002 and BS:EN 50318:2018. In both cases, excellent results were produced in terms of both realism and speed. There was one discrepancy between the results obtained and the benchmark results for the 2018 European Standard: the model gave a higher standard deviation of contact force between 0Hz and 5Hz for the rear pantograph at 320km/hour than the European Standard expected. However, it was noted in [22] that the dispersal of indicator values used to generate the required ranges was especially high for the rear pantograph at this speed. Therefore, the model's value seems believable.

The 2002-standard modelling was performed faster than real speed on a desktop PC, whereas the 2018-standard modelling was performed at around one tenth of real speed. These results support the thesis's hypothesis that the Galerkin approach can produce realistic results with excellent simulation speed. This large improvement in simulation speed over existing FEM software is the greatest achievement of the Simulink model.

The model was updated in order to simulate a real test track. The final model allowed for one or two pantographs and any number of contact wires, with transition events being realistically modelled. Dropper unloading was also included in the model. This model

was extensively tested and consistently produced believable results.

This work serves as a proof of concept of a Galerkin approach to pantograph-catenary modelling. It has been shown that this novel approach can yield useful results for a real-world pantograph system. The model can be expanded and improved substantially to support a variety of real OLE systems, but it has been demonstrated that the Galerkin approach is a powerful solution method for this problem.

Furthermore, contact forces between pantographs and contact wires were calculated realistically throughout contact events. Much of the existing simulation software assumes that when a pantograph is in contact with two wires, the contact force is split 50:50 between the wires. This work shows that this assumption is unrealistic, especially around the time of a contact event, and that the contact force exerted on each wire can be calculated separately.

Another advantage of the Simulink model is that it does not require a constant train speed throughout the simulation. Moreover, the model can accept any acceleration profile as an input and even allows the acceleration profile to be determined while the simulation is running. This will allow a human ‘driver’ to react to the wire deflections and contact force and control the speed of the simulated train as the simulation is performed.

There was one serious limitation of the model: the model was unable to implement certain events and the simulation had to be stopped due to infinite chatter. However, this limitation can likely be removed through careful events modelling, allowing any pantograph-catenary system to be modelled robustly.

7.2 Further Work

Improvement of Event Robustness

The lack of robust event modelling is by far the greatest flaw of the current model. Therefore, solving this problem of high-frequency chatter is the most important way to improve the model. Numerous methods have been presented for modelling the impact of a thin beam against a stop [26,38,54,57–59] and it is very likely that one of them is suitable for

pantograph-catenary modelling.

Validation Against Old Dalby Test Data

There is real track-test data available for fifty-six test runs conducted on the Old Dalby track. Once the events are being implemented robustly, these test runs can be simulated and the results compared to the real Old Dalby data to validate the model.

Simulation Speed

Although effort has been made to maximise the speed of the Simulink model, there is much room for improvement. If the simulation time can be reduced to less than the real time, then the model can be used to predict future catenary behaviour and avoid any problems by reducing the train speed. If this is not achievable, then fast simulations will still be useful for testing many ‘what if?’ scenarios.

One way to increase the final model’s simulation speed is through the use of variable-sized matrices: each wire requires a different number of eigenmodes to be evaluated, but the current model uses the same matrix dimensions for all wires, with shorter wires’ matrices being appended with zeros. This is highly inefficient and can be resolved by allowing the matrices to take variable sizes.

Another improvement would be the use of more enabled subsystems to remove any unnecessary calculations. The impact-modelling subsystem is currently particularly inefficient, with many unused terms being calculated.

Singularity Avoidance

Singular $S(\underline{x}_p(t))$ - and $F(\underline{x}_p(t))$ -matrices were avoided by changing the eliminated eigenmodes based on the pantograph position in Section 6.2.5. The algorithm used was very basic and can be improved, with the aim of minimising the number of $x_p(t)$ -events and therefore improving the simulation speed.

Generalisation of Model

The model should be generalised to any number of pantographs and overlapping contact wires. This is particularly important when modelling contact wires of similar length to the pantograph separation, because the front and rear pantographs may be simultaneously in contact with nonadjacent wires. This entails a straightforward update to the Simulink model, because the equations in Section 4.2.1 are still valid: the 2×2 matrices just become 3×3 . However, there will be eight possible contact conditions, as opposed to four, so keeping $S(\underline{x}_p(t))$ and $F(\underline{x}_p(t))$ nonsingular will be more difficult.

Simplified Events

Simplified events were implemented only as a proof of concept in Chapter 5: the full-events model for the 2018 European Standard was adjusted so that unnecessary events were ignored. This means that the simplified-events model is poorly optimised and its speed can be substantially increased. With a properly optimised model, no events will have to be detected outside of overlap spans and the excellent speed of eventless simulations will be recovered. In the overlap spans, only one trigger signal will be evaluated at any given time, instead of four.

Discrete Components

There are some catenary systems that contain discrete components which are not part of the regular catenary topology. One such component is the section insulator, which allows the pantograph to be transferred from one electrical power source to another without losing contact. Discrete components have not been modelled in this thesis and will need to be added to the model.

Bridges and Level Crossings

Some catenary systems are topologically different from the norm, such as those found under bridges and above level crossings. Under a bridge, there is no room for a messenger wire and a modified contact wire is used instead. Above a level crossing, the contact wire

must be raised in order to provide sufficient clearance. These atypical catenary systems are not currently supported and the model must be updated to include them.

Aerodynamic Effects

Wind loading has not been considered in this thesis, but it is an important aspect of pantograph-catenary modelling. It is explained in [47] that cross wind has three relevant effects on the pantograph-catenary interaction:

1. The direct wind force on the overhead wires.
2. The direct wind force on the pantographs.
3. The force on the train, which affects the movement on the train and therefore moves the base of the pantograph.

These effects should be incorporated into the model and studied in combination with the dynamic pantograph-catenary interaction.

Bibliography

- [1] Current collection technical guide. https://tr.mersen.com/uploads/tx_mersen/17-current-collection-technical-guide-mersen_08.pdf. Accessed: 2019-03-18.

- [2] Electric traction power. <http://www.railway-technical.com/infrastructure/electric-traction-power.html>. Accessed: 2020-03-14.

- [3] Hanger clamp. <https://www.kruch.com/en/productsandservices/catenarycomponents/hangerclamps/hkl-01clampwiththimbleconnection/>. Accessed: 2020-03-14.

- [4] High Speed Two: From concept to reality. <https://www.gov.uk/government/publications/hs2-from-concept-to-reality>. Accessed: 2021-02-13.

- [5] HS2 Q&A: Where is the route, how much will it cost and when will it open? <https://www.cityam.com/qa-what-is-the-hs2-route-how-much-will-it-cost-and-when-will-it-open/>. Accessed: 2020-03-14.

- [6] Pantograph and catenary system. https://www.researchgate.net/figure/Pantograph-and-catenary-system_fig1_282217813. Accessed: 2020-03-14.

- [7] Pantograph (transport). [https://en.wikipedia.org/wiki/Pantograph_\(transport\)](https://en.wikipedia.org/wiki/Pantograph_(transport)). Accessed: 2020-03-14.
- [8] TENSOREX - spring tensioning system for overhead lines on electric railways. <https://www.pfisterer.com/en/our-products/products/tensorex/>. Accessed: 2019-03-13.
- [9] What is pantograph? How they are used in electric rail engines? <https://medium.com/@shubhranshum1/what-is-pantograph-how-they-are-used-in-electric-rail-engines-43f0b253b8ed>. Accessed: 2020-03-14.
- [10] Jorge Ambrósio, João Pombo, Pedro Antunes, and Manuel Pereira. PantoCat statement of method. *Vehicle System Dynamics*, 53(3):314–328, 2015.
- [11] Jorge Ambrósio, Joao Pombo, Manuel Pereira, Pedro Antunes, and António Mósca. A computational procedure for the dynamic analysis of the catenary-pantograph interaction in high-speed trains. *Journal of Theoretical and Applied Mechanics*, 50(3):681–699, 2012.
- [12] Jorge Ambrósio, Frederico Rauter, João Pombo, and Manuel Pereira. Dynamics of high-speed train pantograph-catenary co-simulation of finite element and multibody codes. In *AIP Conference Proceedings*, volume 1233, pages 213–218. AIP, 2010.
- [13] M Arnold and B Simeon. Pantograph and catenary dynamics: a benchmark problem and its numerical solution. *Applied Numerical Mathematics*, 34(4):345–362, 2000.
- [14] Uri M Ascher and Linda R Petzold. Projected implicit Runge–Kutta methods for differential-algebraic equations. *SIAM Journal on Numerical Analysis*, 28(4):1097–1120, 1991.
- [15] Uri M Ascher and Raymond J Spiteri. Collocation software for boundary value differential-algebraic equations. *SIAM Journal on Scientific Computing*, 15(4):938–952, 1994.

- [16] İlhan Aydin, Mehmet Karakose, and Erhan Akin. A new contactless fault diagnosis approach for pantograph-catenary system using pattern recognition and image processing methods. *Advances in Electrical and Computer Engineering*, 14(3):79–88, 2014.
- [17] Olivier Andre Bauchau and James I Craig. *Structural analysis: with applications to aerospace structures*, volume 163. Springer Science & Business Media, 2009.
- [18] Alan Baxter. Network Rail a guide to overhead electrification. no. February. *Network Rail, London*, 2015.
- [19] Jesús Benet, Angelines Alberto, Enrique Arias, and Tomás Rojo. A mathematical model of the pantograph-catenary dynamic interaction with several contact wires. *International Journal of Applied Mathematics*, 37(2), 2007.
- [20] A Bobillot, V Delcourt, P Demanche, and JP Massat. Pantograph-catenary: three paths to knowledge. In *Proceedings of the World Congress on Railway Research*, 2006.
- [21] Kathryn Eleda Brenan, Stephen L Campbell, and Linda Ruth Petzold. *Numerical solution of initial-value problems in differential-algebraic equations*, volume 14. Siam, 1996.
- [22] Stefano Bruni, Jorge Ambrosio, Alberto Carnicero, Yong Hyeon Cho, Lars Finner, Mitsuru Ikeda, Sam Young Kwon, Jean-Pierre Massat, Sebastian Stichel, Manuel Tur, et al. The results of the pantograph–catenary interaction benchmark. *Vehicle System Dynamics*, 53(3):412–435, 2015.
- [23] Stefano Bruni, Alan Facchinetti, M Kolbe, JP Massat, et al. Hardware-in-the-loop testing of pantograph for homologation. In *9th World Congress on Railway Research WCRR*, 2011.
- [24] Giuseppe Bucca and Andrea Collina. A procedure for the wear prediction of collector strip and contact wire in pantograph–catenary system. *Wear*, 266(1-2):46–59, 2009.

- [25] Tore Dahlberg. Moving force on an axially loaded beam—with applications to a railway overhead contact wire. *Vehicle System Dynamics*, 44(8):631–644, 2006.
- [26] A Fathi and N Popplewell. Improved approximations for a beam impacting a stop. *Journal of Sound and Vibration*, 170(3):365–375, 1994.
- [27] Claus Führer and BJ Leimkuhler. Numerical solution of differential-algebraic equations for constrained mechanical motion. *Numerische Mathematik*, 59(1):55–69, 1991.
- [28] Charles William Gear, Ben Leimkuhler, and Gopal K Gupta. Automatic integration of Euler-Lagrange equations with constraints. *Journal of Computational and Applied Mathematics*, 12:77–90, 1985.
- [29] RT Gray, S Levy, JA Bain, and EJ Leclerc. Effect of design changes in railway catenary-pantograph systems on power collection at high speed. *Journal of Engineering for Industry*, 90(4):680–689, 1968.
- [30] Ross Hanley, Riccardo Licciardello, Ségolène Martin, and Keith Rose. TrioTRAIN: bringing research and standardisation closer together. In *Transport Research Arena (TRA) 5th Conference: Transport Solutions from Research to Deployment*, 2014.
- [31] DJ Hartland. Developments towards an active pantograph. 1998.
- [32] R Hauber. Numerical treatment of retarded differential–algebraic equations by collocation methods. *Advances in Computational Mathematics*, 7(4):573–592, 1997.
- [33] William J Hausman, Peter Hertner, and Mira Wilkins. *Global electrification: multinational enterprise and international finance in the history of light and power, 1878–2007*. Cambridge University Press, 2008.
- [34] British Standards Institution. BS:EN 50318:2002. *CENELEC*, 2002.
- [35] British Standards Institution. BS:EN 50318:2018. *CENELEC*, 2018.

- [36] Y. Katada and S. Tabayashi. OCS inspection system for high-speed railways. *Meiden Review*, pages 32–38, 2015.
- [37] S Levy, JA Bain, and EJ Leclerc. Railway overhead contact systems, catenary-pantograph dynamics for power collection at high speeds. *Journal of Engineering for Industry*, 90(4):692–699, 1968.
- [38] SQ Lin and CN Bapat. Extension of clearance and impact force estimation approaches to a beam-stop system. *Journal of Sound and Vibration*, 163(3):423–428, 1993.
- [39] C. Maggs. *Steam Trains: The Magnificent History of Britain’s Locomotives from Stephenson’s Rocket to BR’s Evening Star*. Amberley Publishing Limited, 2014.
- [40] P. Mantegazza and P. Masarati. Analysis of systems of differential-algebraic equations (DAE). *Graduate Course on “Multibody System Dynamics”*, 2012.
- [41] JP Massat, JP Laine, and A Bobillot. Pantograph–catenary dynamics simulation. *Vehicle System Dynamics*, 44(sup1):551–559, 2006.
- [42] Sven Erik Mattsson and Gustaf Söderlind. Index reduction in differential-algebraic equations using dummy derivatives. *SIAM Journal on Scientific Computing*, 14(3):677–692, 1993.
- [43] Arne Nordmark, Harry Dankowicz, and Alan Champneys. Friction-induced reverse chatter in rigid-body mechanisms with impacts. *IMA Journal of Applied Mathematics*, 76(1):85–119, 2010.
- [44] Arne B Nordmark and Petri T Piiroinen. Simulation and stability analysis of impacting systems with complete chattering. *Nonlinear dynamics*, 58(1-2):85–106, 2009.
- [45] G Poetsch, JE Evans, R Meisinger, W Kortüm, W Baldauf, A Veitl, and J Wallaschek. Pantograph/catenary dynamics and control. *Vehicle system dynamics*, 28(2-3):159–195, 1997.

- [46] D Pogorelov. Differential–algebraic equations in multibody system modeling. *Numerical Algorithms*, 19(1-4):183–194, 1998.
- [47] J Pombo, J Ambrósio, M Pereira, F Rauter, Andrea Collina, and Alan Facchinetti. Influence of the aerodynamic forces on the pantograph–catenary system for high-speed trains. *Vehicle System Dynamics*, 47(11):1327–1347, 2009.
- [48] J Pombo, P Antunes, and J Ambrósio. A study on multiple pantograph operations for high-speed catenary contact. In *Proc. Proceedings of the Eleventh International Conference on Computational Structures Technology*, 2012.
- [49] Frederico Grases Rauter, João Pombo, Jorge Ambrósio, Jérôme Chalansonnet, Adrien Bobillot, and Manuel Seabra Pereira. Contact model for the pantograph–catenary interaction. *Journal of System Design and Dynamics*, 1(3):447–457, 2007.
- [50] Werner C Rheinboldt. Differential-algebraic systems as differential equations on manifolds. *Mathematics of Computation*, 43(168):473–482, 1984.
- [51] Jong-Hwi Seo, Seok-Won Kim, Il-Ho Jung, Tae-Won Park, Jin-Yong Mok, Young-Guk Kim, and Jang-Bom Chai. Dynamic analysis of a pantograph–catenary system using absolute nodal coordinates. *Vehicle System Dynamics*, 44(8):615–630, 2006.
- [52] Jong-Hwi Seo, Hiroyuki Sugiyama, and Ahmed A Shabana. Three-dimensional large deformation analysis of the multibody pantograph/catenary systems. *Nonlinear Dynamics*, 42(2):199–215, 2005.
- [53] William James Stronge. *Impact mechanics*. Cambridge University Press, 2018.
- [54] Róbert Szalai. Impact mechanics of elastic structures with point contact. *Journal of Vibration and Acoustics*, 136(4):041002, 2014.
- [55] X Tang, DM Kabat, RJ Natkin, WF Stockhausen, and J Heffel. A new contactless fault diagnosis approach for pantograph–catenary system using pattern recognition and image processing methods. *Journal of Engines*, 111(3):631–642, 2002.
- [56] Conrad Volk. *Magnus Volk of Brighton*. Phillimore & Co Ltd, 1971.

- [57] C Wang and J Kim. New analysis method for a thin beam impacting against a stop based on the full continuous model. *Journal of Sound and Vibration*, 191(5):809–823, 1996.
- [58] C Wang and J Kim. The dynamic analysis of a thin beam impacting against a stop of general three-dimensional geometry. *Journal of Sound and Vibration*, 203(2):237–249, 1997.
- [59] XC Yin, Y Qin, and H Zou. Transient responses of repeated impact of a beam against a stop. *International Journal of Solids and Structures*, 44(22-23):7323–7339, 2007.